PICOSECOND ULTRASONICS FOR NANOSCALE SUBSURFACE STRUCTURAL CHARACTERIZATION

MAKSYM ILLIENKO

Ph.D. thesis, Vrije Universiteit Amsterdam, 2026
Picosecond Ultrasonics for Nanoscale Subsurface Structural Characterization.
Maksym Illienko

Printed by Ridderprint
ISBN: 978-94-92323-96-5
DOI: `https://doi.org/10.5463/thesis.1647`
An electronic version of this dissertation is available at: `https://research.vu.nl`

VRIJE UNIVERSITEIT

PICOSECOND ULTRASONICS FOR NANOSCALE SUBSURFACE STRUCTURAL CHARACTERIZATION

ACADEMISCH PROEFSCHRIFT

ter verkrijging van de graad Doctor of Philosophy
aan de Vrije Universiteit Amsterdam,
op gezag van de rector magnificus
prof.dr. J.J.G. Geurts,
volgens besluit van de decaan
van de Faculteit der Bètawetenschappen
in het openbaar te verdedigen
op maandag 8 juni 2026 om 11.45 uur
in de universiteit

door

Maksym Illienko

geboren te Tsjernihiv, Oekraïne

promotoren:	prof.dr. S.M. Witte
	prof.dr. K.S.E. Eikema
copromotor:	prof.dr. P.C.M. Planken
promotiecommissie:	prof.dr. C.P. Broedersz
	prof.dr. I. Setija
	dr. E. Olsson
	prof.dr. P. Ruello
	dr. G.G.J. Renaud

The work described in this thesis was carried out at the Advanced Research Center for Nanolithography (ARCNL), a public-private partnership between the University of Amsterdam (UvA), the Vrije Universiteit Amsterdam (VU), Rijksuniversiteit Groningen (RUG), the Netherlands Organisation for Scientific Research (NWO), and the semiconductor equipment manufacturer ASML.

I had come to an entirely erroneous conclusion, my dear Watson, how dangerous it always is to reason from insufficient data.

Arthur Conan Doyle,
The Adventure of the Speckled Band

CONTENTS

INTRODUCTION

The development of ultrafast pulsed lasers expanded the scope of experimental physics by enabling the investigation of processes occurring on ultrashort timescales. Within the femtosecond regime of light-matter interaction, many processes that happen on a picosecond timescale, such as molecular dynamics, thermal and diffusion dynamics, relaxation processes in solids, chemical reactions, etc., can be considered effectively "frozen", thereby enabling their direct observation [1–6]. Another prominent ability of ultrafast lasers is the induction of rapid localized heating that can lead to the generation of high frequency coherent acoustic phonons. Studying the acoustic generation process and the use of light-induced acoustic pulses to probe material properties led to a new field of research called picosecond ultrasonics (PU), also known as ultrafast photoacoustics.

The idea of PU is shown in Fig. 1. An ultrashort laser pulse (pump) hits an opaque material, leading to the generation of a high-frequency acoustic pulse. The acoustic pulse propagates longitudinally into the sample. At some point, the acoustic pulse reflects either from internal material interfaces or from the back surface of the sample. Returning to the front surface, the acoustic pulse forms an acoustic echo. This echo can then be detected by the second ultrashort laser pulse (probe). By controlling the time delay between pump and probe pulses, one can investigate the generation and propagation dynamics of light-induced acoustics.

Pioneering experiments in PU were conducted on metal films in the late 1980s [7–9]. Since then, the technique has been developed and found applications in various physics studies. In particular, it was used for thin film characterization [10–16], adhesion testing [17–19], detection and imaging of buried structures [20–26], and contrast microscopy of biological cells [27–31]. Apart from that, the development

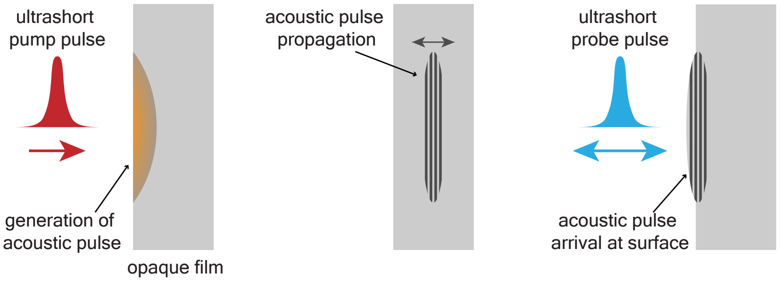

Figure 1: Schematic of the experiment in picosecond ultrasonics.

of PU contributed to studies of solid properties such as electron transport, electron-phonon coupling, phonon-phonon scattering, etc. [32–35].

Even though the concept of the photoacoustic technique (Fig. 1) appears intuitive, the underlying processes are far from trivial. Let us begin with the generation of acoustic waves. The energy from a laser pulse can be transferred into coherent vibrations of a solid in several ways. The most common one is the thermoelastic mechanism [36]. In this case, laser energy is first converted into heat, which then drives the rapid thermal expansion of the solid. Naturally, the shape of the resulting acoustic pulse depends on the volume of the heated region, the heating rate, and the material's elastic properties. The extent of the heated region itself is determined by the thermal properties of the solid and the penetration depth of the laser light [7, 36]. As a result, controlling the temporal profile and frequency spectrum of the generated acoustic waves becomes challenging, since the process is strongly influenced by the sample's intrinsic material parameters. One way to address this challenge is to employ photoacoustic transducers. These are typically deposited onto the sample as additional thin layers of materials with optimal properties for acoustic wave generation [26, 37–39]. The pump light, absorbed by these layers, excites resonant vibrations that are subsequently coupled into an acoustic wave propagating in the sample. Furthermore, nanostructuring the surface has emerged as a promising method for tailoring both the frequency content and spatial distribution of the generated acoustic waves [40–44]. The obvious drawback of such approaches is the need to modify the sample, which undermines the non-invasive benefit of PU. However, this limitation can be avoided by combining PU with complementary techniques, e.g., atomic force microscopy (AFM). In this hybrid approach, the acoustic wave is generated in the AFM tip and then coupled into the sample [44]. The AFM tip can be modified for more efficient generation of acoustics, which does not affect experimental samples. Besides non-invasivity, this approach also allows for a dramatic increase in lateral resolution.

Detection is another non-trivial aspect of PU. It usually relies on monitoring changes in the optical properties of the sample induced by the propagating strain wave. These changes are observed as transient variations in the reflectivity or transmissivity of the probe light and usually have magnitudes on the order of 10^{-4} or lower. Detecting such minor variations requires highly sensitive measurement systems and, in some cases, long integration times. The quadratic frequency dependence of acoustic attenuation further worsens the problem. High-frequency acoustic waves are strongly damped, making it particularly difficult to probe deeply buried interfaces. Several strategies have been explored to enhance detection sensitivity.

It is highly recommended to take a break every 30 minutes during long periods of sitting. Practicing Lindy Hop swing outs is a great option to fill these breaks! Just follow this lovely couple in the corner of the pages.

These strategies include exploiting surface plasmon resonance effects [45–47] and interferometry effects [48–51].

In most experiments, the quantity of interest is the strain field of acoustic echoes. However, the experimentally measured transient reflectivity or transmissivity represents a convoluted optical response. The detected optical signal depends not only on the strain profile within the sample, but also on the photoelastic constants and the optical properties of the material [36]. While optical constants can be measured with relative ease, determining the complete set of photoelastic constants in opaque materials remains a challenging task. This is typically achieved by fitting numerical models to experimental photoacoustic data, which again underscores the importance of controlling the generated strain waves.

Despite the discussed challenges of the PU technique, it remains of high interest due to the extremely high frequencies of the generated acoustics. Those frequencies typically belong to the GHz-THz range. High acoustic frequencies result in short wavelengths, which potentially allows for high-resolution imaging of structures buried below optically opaque materials. For example, at frequency 100 GHz and speed of sound $10\,\mathrm{km/s}$, the wavelength is 100 nm, which goes beyond the visible optical range (in most solids, the speed of sound is significantly lower leading to even shorter wavelength). Naturally, this brings extra motivation to develop PU as a high-resolution imaging tool.

A technique closely related to PU is gigahertz scanning acoustic microscopy (GHz-SAM) [52]. In this method, sound is generated by a piezoelectric emitter mounted on a sapphire block. Zinc oxide (ZnO) crystals are commonly used as piezoelectric elements since they allow operation at GHz frequencies [52, 53]. The generated acoustic waves travel through the sapphire block and are coupled into the sample via a coupling liquid. The sapphire/liquid interface has a concave shape that allows focusing of the acoustic wave. The reflected acoustic wave then couples back into the sapphire block and is detected by the same transducer. This approach can achieve submicron resolution and is applicable in biomedical and semiconductor metrology [54, 55]. However, the acoustic frequencies are limited to several GHz, which remains significantly lower than the frequency range accessible with light-induced acoustics. Additionally, the use of a coupling liquid is necessary to transmit the generated acoustics into the sample, which may restrict the applicability of GHz-SAM in scenarios where non-invasiveness is required.

One such case is metrology during the nanolithography process in semiconductor manufacturing. Nanolithography is a crucial technology for the production of integrated circuits (ICs). Integrated circuits appeared as a result of the miniaturization trend in the semiconductor industry. Since transistor size (a key component of any electronic device) was consistently decreasing, at some point, fabricating each transistor individually with subsequent assembly into a device became infeasible.

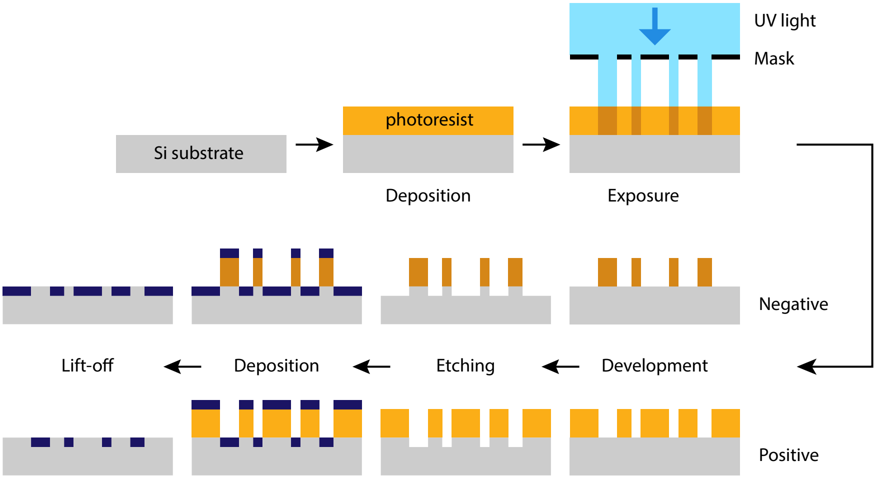

Figure 2: Schematic representation of the optical nanolithography process.

Instead, electronic devices (chips) are "printed" as a single, complete entity where all the individual elements are indistinguishable (integrated). Nowadays, this "printing" approach enables the fabrication of chips with transistor densities exceeding $100\,\mathrm{MT/mm^2}$ (MT stands for mega-transistor) [56].

The workflow of the lithographic process is shown in Fig. 2. A substrate (usually a silicon wafer) is coated with a layer of special light-sensitive material called photoresist. Then the substrate is illuminated with ultraviolet light through the mask, which contains the desired pattern. This pattern is translated onto the photoresist. The exposed areas of the photoresist change their physical properties (specifically solubility), and at the next development step, either exposed (positive resist) or unexposed (negative resist) areas of photoresist are removed. After that, areas of the substrate not covered by photoresist undergo necessary processing such as etching, deposition, or doping. At the final step (lift-off), the photoresist is removed, yielding a patterned substrate. This process can be repeated multiple times, depending on the design of the electronic device. Conventionally, at every new iteration, the wafer must be well-positioned to ensure all printed layers are aligned vertically. The requirement for alignment accuracy is determined by the desired overlay performance, which, in modern devices, should be better than 2 nm [57]. Achieving such high overlay performance requires wafer positioning with subnanometer accuracy.

The alignment procedure is shown in Fig. 3. Special grating-type markers are printed on the wafer in the first round of lithography. These markers are then

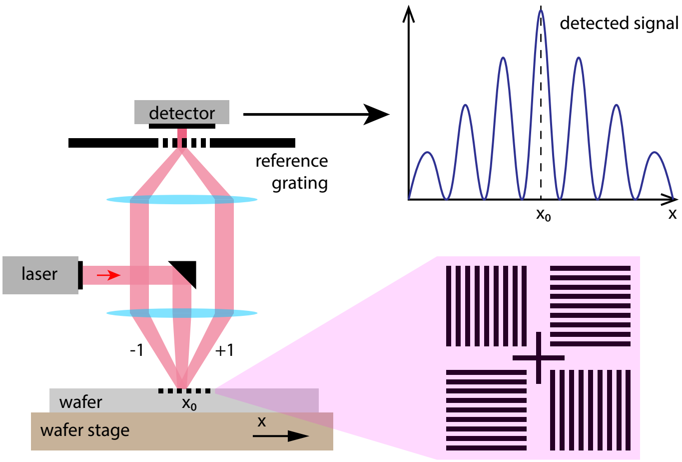

Figure 3: The concept of wafer alignment metrology. A laser beam illuminates a grating-type marker. The +1st and −1st order of diffracted light are focused onto the reference grating to create a filtered image of the marker. The intensity of light transmitted by the reference grating exhibits an oscillatory dependence on the wafer position, allowing for sub-nm-level positioning (adapted from [58]).

illuminated with a laser beam. The +1st and −1st diffraction orders are focused at the detector plane and create an interference fringe pattern. This fringe pattern is imaged onto a reference grating, and transmitted light is picked up by a detector. The overlay of the fringe image and the reference grating, i.e., the detector signal, depends on the absolute wafer position, resulting in a periodic alignment curve shown in Fig. 3. The wafer position can be retrieved from the phase of this detected signal. Consequently, the alignment accuracy is determined by how precisely the phase can be measured, which is defined by the signal-to-noise ratio of the detected signal. This allows subnanometer-level alignment accuracy even with the use of micron-pitch target gratings and visible light [58].

Alignment becomes crucial to 3D-designed devices such as 3D NAND memory chips. In the example shown in Fig. 4, the 3D NAND chip contains a multilayer stack which forms an array of memory cells with corresponding word lines (control gates). Word lines are connected via vertical channels to the bit line and source line. To fabricate such a device, the alternating layers are first deposited on top of a silicon wafer. Then, the high aspect-ratio vertical channels are etched through the multilayered stack. To apply etching at the correct positions, one needs to detect alignment markers through the deposited multilayered stack. Modern memory chips can contain more than 200 layers, with a stack thickness of tens of microns [59, 60], making optical detection of buried alignment markers more challenging. Furthermore, to protect layers during the etching process, a hard mask is usually deposited on top of the stack. This mask typically consists of a µm-thick layer of optically

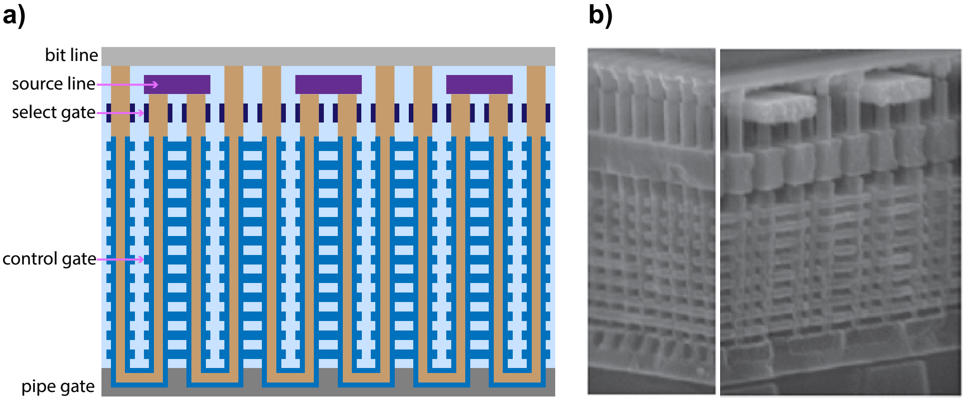

Figure 4: a) Schematic drawing of a 3D NAND device. b) Scanning electron microscope image of 3D NAND BiCS cell (image is taken from [61]).

opaque tungsten or carbon.

Luckily, almost all solids transmit sound. Thus, picosecond ultrasonics (ultrafast photoacoustics) has a potential to overcome the problem of alignment and imaging through optically opaque materials. The principle of photoacoustic alignment is similar to the one described earlier (Fig. 1) and is shown in Fig. 5. The ultrafast laser pulse (pump) illuminates the top opaque layer and gets absorbed. Absorbed energy is partially transferred via different physical mechanisms (depending on the material) into an acoustic wave that propagates towards the bottom of the stack. At the bottom, the acoustic wave reflects from the grating marker. Depending on the grating type, the reflected acoustic wave will have a modulated wavefront or amplitude (or both) with the periodicity of the grating marker. When the reflected acoustic wave returns to the top surface, it causes periodic modulation of both height and optical constants of the top layer. At this specific time delay, the surface is illuminated by the second ultrafast laser pulse (probe). Two approaches are possible. The first one is to illuminate the surface with a wide-area probe pulse, with a diameter larger than the grating pitch. This pulse will diffract on the periodic perturbation of the surface, and the alignment procedure will be similar to the one shown in Fig. 3. The second approach involves probing the surface with a tightly focused laser pulse while scanning the wafer's position. This will result in periodic modulation of the reflected light intensity, allowing for contrast imaging, which can also be modified into an alignment procedure. As mentioned earlier, alignment targets contain micron-pitch gratings, which can be sufficiently resolved by GHz-THz acoustics. Thus, alignment accuracy is determined by the strength of the detected signals and measurement time. Moreover, the imaging capability of PU should also be considered as an alternative tool for inspection purposes, such as overlay control.

Although the described photoacoustic metrology appears to be similar to con-

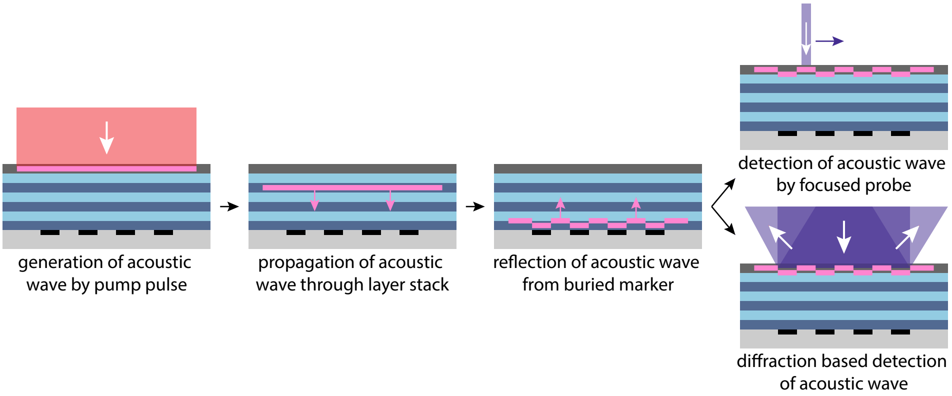

Figure 5: Schematic of photoacoustic detection of buried alignment markers. An ultrashort laser pulse hits an opaque layer, generating an acoustic pulse. The acoustic pulse propagates into the stack and reflects from the buried objects. A reflected acoustic pulse returns to the surface, where a delayed optical probe pulse detects it.

ventional optical metrology, there are several fundamental differences. In photoacoustics, the detection of buried alignment markers is inherently more complex, since the measurement does not access the markers directly but instead relies on acoustic waves as intermediate carriers of information. The nature of these elastic waves differs substantially from that of light. That results in differences in wave propagation aspects, such as polarization modes, refraction and reflection laws, etc. Furthermore, unlike optical metrology, which typically employs monochromatic light, light-induced elastic waves possess a broad frequency spectrum. This spectral broadness introduces more intricate diffraction and interference effects, making the interpretation of acoustic signals distinct from optical ones. Finally, while the detection step in photoacoustics remains optical, the probe pulse does not detect the alignment marker itself but rather an “acoustic copy” of it. The efficiency of this detection is governed by the strength of the strain-optic coupling, i.e., how effectively strain waves induce transient refractive index changes, which varies strongly with materials.

OUTLINE OF THE THESIS

Although the PU already has shown capability of hidden gratings detection and imaging through opaque layers in the samples similar to semiconductor devices [20–23], weak photoacoustic signals due to low amplitudes of light-induced acoustic waves and weak strain-optic coupling, require significant measurement integration time to achieve satisfactory signal-to-noise ratio. Due to this, for industrial applications of PU, further studies are needed to achieve efficient acoustic generation and sensitive acoustic detection. Additionally, there is an interest in developing high-resolution

PU imaging that could go beyond the optical diffraction limit. This is potentially possible since light-induced acoustics has significantly shorter wavelengths compared to optical wavelengths. These problems are addressed in our studies, and the results are summarized in this thesis.

In Chapter 1 we introduce a theoretical background of picosecond ultrasonics. Generation, propagation, and detection of acoustic waves are discussed. We introduce the governing equations, along with a numerical simulation model, which we use to simulate photoacoustic experiments. In Chapter 2 we describe the experimental technique used in our research. The developed pump-probe experimental setup is based on asynchronous optical sampling (ASOPS) with the ability to modulate the repetition frequency offset, enabling better performance compared to conventional designs that use ASOPS or a mechanical delay line. Chapter 3 presents results of studies on how thin transparent layers deposited on top of opaque layers influence photoacoustic signals. The deposition of thin layers typically leads to signal enhancement; however, the signals can be distorted due to a complex interplay of additional optical effects that occur in such structures. In Chapter 4 we investigate the possibility of sub-optical-wavelength grating characterization. We demonstrate that picosecond ultrasonics is capable of retrieving grating parameters, such as pitch, duty cycle, and grating lineshape, at grating pitches below the wavelength of the probing light. We also address the possibility of detecting grating defects. In Chapter 5, we examine the photoacoustic response of periodic structures to study the correlation between excited vibration modes in those structures and their geometrical shape.

1

THEORY

INTRODUCTION

Any ultrafast photoacoustic experiment involves repetitive exposure of the sample of interest by a pair of laser pulses. The first laser pulse (pump) induces the acoustic pulse that propagates throughout the sample, while the second time-delayed laser pulse (probe) detects changes in the sample reflectivity caused by present acoustic waves. Behind this seemingly simple experimental scheme, many physical processes involved in acoustics generation and propagation occur inside the sample. These processes, being not directly observable, determine changes in sample reflectivity, the only quantity measured experimentally. For this reason, a proper understanding of underlying physics is necessary to interpret experimental results correctly.

This chapter introduces theoretical models of light-induced acoustics generation, propagation, and detection.

1.1 THEORY OF LIGHT-INDUCED ELASTIC WAVES

1.1.1 GENERATION

When a laser pulse hits a solid, the interaction between the laser field and the solid's electrons actually happens. If the material is absorptive (e.g. metals or semiconductors), electrons get excited to higher energy levels. The change in electron energy distribution leads to a change in the equilibrium interatomic distance, causing internal stress. In order to release the stress, the material undergoes deformation that launches an elastic wave. This mechanism of elastic wave generation is called the deformation potential (DP) mechanism [62]. It takes place both in metals and semiconductors. However, in metals, due to the ultrafast thermalization of excited electrons with the lattice, the DP mechanism is efficient only within the first ps [63]. Afterward, the heating of the lattice gives rise to thermal stress, which becomes the dominant source of elastic wave generation in metals [62]. Since thin metal films are studied in current research, we will focus only on the thermal (thermoelastic) mechanism. There are other possible mechanisms of elastic wave generation, such as the inverse piezoelectric effect and electrostriction [62]. However, materials used in current research do not have piezoelectric properties. Regarding electrostriction, this effect occurs only in transparent media and has low efficiency in elastic wave generation [62].

Thermoelasticity is the volume change under the temperature variations. This effect originates from the anharmonicity of the interatomic potential [64]. The increase in lattice temperature increases the vibrational energy of the atoms. In the case of an anharmonic interatomic potential, a change in vibrational energy leads to a shift in mean interatomic distance that is observed as volume change. The thermal strain ε_{ij}^{th} that medium undergoes after heating (or cooling) when it reaches equilibrium state can be linearly linked to a temperature change ΔT: $\varepsilon_{ij}^{th} = \alpha_{ij}\Delta T$, where α_{ij} is the tensor of thermal expansion. To describe the elastodynamics of the medium, it is more convenient to operate not with thermal strain but with thermal stress. Thermal stress is the internal stress that evolves in the medium right after it undergoes the temperature change. This stress is basically an “internal force” that causes expansion or contraction of the medium under the temperature change. Thermal stress for the isotropic medium is also linearly linked to temperature change as

$$\sigma_{ij}^{th} = -3K\alpha\delta_{ij}\Delta T, \tag{1.1}$$

where K is the bulk modulus, α is the isotropic linear thermal expansion coefficient, δ_{ij} is the Kronecker delta tensor. The derivation of Eq. 1.1 will be shown later in Section 1.1.2.

From Eq. 1.1, one can see that the source of elastic waves is directly related to the temperature change. Thus, to properly describe the generation process, one needs to calculate temperature dynamics in the medium after a pump pulse absorption. As mentioned earlier, the energy of a laser pulse is transferred to the electrons of the solid. In metals, it can be interpreted as increased free electrons (electrons in the conductance band) temperature. Afterward, hot electrons thermalize with lattice via electron-phonon scattering. The process of energy transfer from electrons to lattice was described by Kaganov et al. [65] considering Fermi-Dirac distribution and Bose-Einstein distributions at different temperatures for free electrons and phonons, respectively. In the case of lattice temperature T_l and electronic temperature T_e being much higher than the Debye temperature T_D[1] and $T_e - T_l \ll T_l$, the rate of energy

---

[1] Debye temperature is the temperature at which all the possible vibrational modes of a solid are thermally excited.

transfer per unit volume from electrons to lattice can be aproximated as [65]

$$U = G(T_e - T_l), \qquad G = \frac{\pi^2 m_e c_s^2 n_e}{6\tau_e(T_l)T_l}. \tag{1.2}$$

Where m_e is the effective electron mass, c_s is the speed of sound[2], n_e is the concentration of free electrons, τ_e is the electron relaxation time. The constant G is called the electron-phonon coupling constant.

Based on results derived by Kaganov, Anisimov et al. [67] introduced a two-step model that describes electronic and lattice temperature dynamics in metals during a short laser pulse excitation. The model proposed by Anisimov is known as the Two Temperature Model (TTM), and it is widely used in the field of ultrafast photoacoustics. Later on, Qiu and Tien [68] refined the existing TTM model by solving the Boltzmann transport equation for electrons. The governing equations for the TTM model proposed by Qiu and Tien are:

$$\begin{aligned} C_e(T_e)\frac{\partial T_e}{\partial t} + \nabla \cdot \mathbf{Q}_e &= -G(T_e - T_l) + S(x,y,z,t); \\ \tau_e \frac{\partial \mathbf{Q}_e}{\partial t} + \mathbf{Q}_e &= -k_e(T_e, T_l)\nabla T_e; \\ C_l \frac{\partial T_l}{\partial t} &= G(T_e - T_l). \end{aligned} \tag{1.3}$$

Where $\mathbf{Q}_e$ is the vector of electron heat flux, C_e and C_l are the electron and lattice heat capacity, k_e is the electron thermal conductivity, τ_e is the electron relaxation time, and S is the source defined by laser light absorbed power density. The system 1.3 is quite intuitive. The first and last equations display the energy conservation law for electronic and lattice subsystems, respectively, while the second equation describes heat transport in the electronic subsystem. The difference in the TTM model proposed by Qiu and Tien compared to the one proposed by Anisimov is the wave-type of heat propagation (extra term $\tau_e \frac{\partial \mathbf{Q}_e}{\partial t}$ in Eq. 1.3, hyperbolic TTM) instead of diffusion (parabolic TTM). The wave-type of heat propagation occurs when the characteristic heating time τ_h is comparable to the electron relaxation time τ_e [69]. For the ultrafast photoacoustics, τ_h is related to the pump laser pulse length which is in the order of 100 fs. Meanwhile, electron relaxation time in metals can reach tens of femtoseconds. Thus, we will use the hyperbolic TTM in our theoretical calculations.

Another note about Eqs. 1.3 is that heat transfer happens only through electrons. This is due to relatively high electron heat conductivity compared to the heat conductivity of the lattice [66]. The thermal conductivity of metals (which

---

[2] Speed of sound is calculated from Debye temperature [66]: $c_s = T_D k_b/(6\pi^2\hbar^3 n_a)^{1/3}$, where k_b is the Boltzmann constant and n_a is the atomic number density.

is dominated by electrons) is usually on the order of $\sim$100 Wm^{-1}K^{-1}, while for dielectrics (dominated by phonons) it is $\sim$1 Wm^{-1}K^{-1}. However, in the case of strong gradients of lattice temperature, it might be reasonable to consider lattice heat transfer. This situation can occur on metal/dielectric boundaries or on the boundary between two metals with a big difference in electron-lattice thermalization time (electron-phonon coupling).

The electron heat capacity C_e is approximated from the Sommerfeld model of free electrons [64, 66]:

$$C_e = \gamma T_e, \qquad\qquad \gamma = \pi^2 n_e k_b^2 / 2E_F, \tag{1.4}$$

where n_e is the concentration of free electrons, k_b is the Boltzmann constant, and E_F is the Fermi energy. The Sommerfeld approximation for electron heat capacity works well for low temperatures. Otherwise, one needs to consider electron density of states (DOS) and temperature dependence of the chemical potential [64, 70]. In our experiments, we estimate the peak electron temperature to be below 1000 K-2000 K, and thus apply the Sommerfeld approximation.

According to the Drude model, the electron heat conductivity can be derived from the kinetic theory of gases [66]:

$$k_e = \frac{1}{3} C_e V_F^2 \tau_e = \frac{\pi^2 n_e k_b^2 T_e \tau_e}{3m_e}, \tag{1.5}$$

where V_F is the Fermi velocity. Qiu and Tien showed that electron heat conductivity is proportional to the ratio of electron and lattice temperatures [68]: $k_e = k_{eq}(T_l) T_e / T_l$, where k_{eq} is the heat conductivity at the thermal equilibrium of electrons and lattice. The same temperature dependence can also be retrieved from Eq. 1.5: electron relaxation time τ_e is mainly determined by electron-phonon collisions and is inversionally proportional to phonon concentration that is meanwhile proportional to lattice temperature [66]. The value of k_{eq} can be obtained from literature as a nominal heat conductivity. With the use of Eq. 1.5, we can then estimate the electron relaxation time:

$$\tau_e = \frac{3 m_e k_{eq}}{\pi^2 n_e k_b^2 T_l} = \frac{3 k_{eq}}{V_F^2 \gamma T_l}. \tag{1.6}$$

Now, the expression for electron relaxation time can be substituted into the expression for electron-phonon coupling (Eq. 1.2) [68, 71]:

$$G = \frac{\pi^4 (n_e c_s k_b)^2}{18 k_{eq}}. \tag{1.7}$$

As one can see, G does not depend on electron temperature. The constant value of electron-phonon coupling is commonly used in theoretical studies of thermodynamics in metals exposed by ultrafast laser pulses. However, it should be noted that for high electron temperatures (high energy laser pulses), the Sommerfeld model of free electron gas can not accurately describe electron-phonon energy exchange. In this case, electrons from below the Fermi level start contributing to the electron-phonon collisions. Thus, the electron DOS needs to be taken into consideration [70, 72].

The Two Temperature Model assumes that electrons are in thermal equilibrium, meaning that their state can be described by the Fermi-Dirac distribution function with a specific temperature. However, the absorption of a laser pulse leads to shifting the part of electrons from the vicinity of Fermi level towards higher energies by 1 eV-3 eV (depending on the laser wavelength). These excited nonthermal electrons then thermalize with the Fermi sea via electron-electron scattering. The Two Temperature Model is valid if the electron thermalization time is shorter than electron-phonon thermalization. Otherwise, scattering of nonequilibrium electrons can significantly affect the rate of electron-lattice energy transfer [2, 32, 73]. The effect of nonthermal electrons manifests at low temperatures or low laser fluence [2, 73] where the electron thermalization time can reach picoseconds. In our experimental conditions, the thermalization time is expected to be below 100 fs, which is shorter than the laser pulse duration.

By solving the system of Eqs. 1.3 we can obtain the spatial and temporal evolution of lattice temperature after pump absorption. The lattice temperature can then be used in Eq. 1.1 to define the source of elastic waves. We will introduce the theoretical model for elastic wave propagation in the following subsection.

1.1.2 PROPAGATION

To describe the propagation of elastic waves, we will use the theory of linear elasticity [74], which is based on Newton's second law and Hooke's law. Newton's second law is represented by the elastodynamics equation [74]:

$$\rho\frac{\partial v_i}{\partial t} = \frac{\partial \sigma_{ik}}{\partial x_k}, \tag{1.8}$$

where ρ is the mass density, σ_{ij} is the stress tensor, v_i is the velocity vector of an infinitely small volume of the medium, and x_i is the spatial coordinate vector. Here and for the following equations, we imply Einstein summation for repeating tensor indices. The stress tensor σ_{ij} is defined in such a way that the product $\sigma_{ij}n_j$, where n_j is the unity vector, determines the specific force (Newton per area) applied to the surface normal to the vector n_j. Meanwhile, Hooke's law links stress and strain of the medium:

$$\sigma_{ij} = c_{ijkl}\varepsilon_{kl}, \tag{1.9}$$

where c_{ijkl} is the tensor of elastic constants and ε_{ij} is the strain tensor. The strain tensor determines the *relative* deformation of the medium. It is linked to the vector of absolute displacement u_i of the infinitely small volume as

$$\varepsilon_{ij} = \frac{1}{2}\left(\frac{\partial u_i}{\partial x_j} + \frac{\partial u_j}{\partial x_i}\right). \tag{1.10}$$

The tensor of elastic constants has $3^4 = 81$ components. However, certain symmetry considerations can be applied. Since the energy of the deformed body is a quadratic form of strain $W = c_{ijkl}\varepsilon_{ij}\varepsilon_{kl}$, it should not depend on the permutation of ε_{ij} and ε_{kl}. Additionally, as one can see from Eq. 1.10, the strain tensor is symmetric. Thus, the tensor of elastic constants has the symmetry: $c_{ijkl} = c_{jikl} = c_{ijlk} = c_{klij}$. This reduces the amount of independent components of c_{ijkl} to 21. In the current research, we assume the medium is isotropic. In this case, the amount of independent components of the tensor of elastic constants reduces to 2, and Hooke's law can be written as [74]

$$\sigma_{ij} = K\delta_{ij}\varepsilon_{kk} + 2\mu\left(\varepsilon_{ij} - \frac{1}{3}\delta_{ij}\varepsilon_{kk}\right), \tag{1.11}$$

where K and μ are bulk and shear moduli, respectively, δ_{ij} is the Kronecker delta tensor. Note that stress is nicely separated into volumetric (first term) and shear (second term) components.

In general, the process of medium deformation is irreversible. That means that part of mechanical energy dissipates into heat. Phenomenologically, this can be considered as a presence of *friction forces*, which are linearly dependent on velocity. The tensor of *friction stress* can be defined as [74]:

$$\sigma^{v}_{ij} = \chi\delta_{ij}\dot{\varepsilon}_{kk} + 2\xi\left(\dot{\varepsilon}_{ij} - \frac{1}{3}\delta_{ij}\dot{\varepsilon}_{kk}\right), \tag{1.12}$$

where χ and ξ are viscous coefficients. The dot above the strain tensor depicts a time derivative.

To include the source of elastic waves, we need to add thermal stress σ^{th}_{ij}. Right after the temperature increase, the medium is constrained with respect to its new equilibrium state. Assuming isotropic thermal expansion, the thermal strain is $\varepsilon^{th}_{ij} = -\alpha\delta_{ij}\Delta T_l$, where α is the linear thermal expansion coefficient. By inserting thermal strain into Eq. 1.11, one gets the expression for thermal stress:

$$\sigma^{th}_{ij} = -\left[K\delta_{ij}\delta_{kk} + 2\mu\left(\delta_{ij} - \frac{1}{3}\delta_{ij}\delta_{kk}\right)\right]\alpha\Delta T_l = -3K\alpha\delta_{ij}\Delta T_l. \tag{1.13}$$

Equations 1.8 and 1.10-1.13 already form the system that describes elastodynamics, where the total stress should be considered as a sum $\sigma_{ij} + \sigma^{v}_{ij} + \sigma^{th}_{ij}$. However, this model can not fully describe the attenuation of elastic waves. The consideration

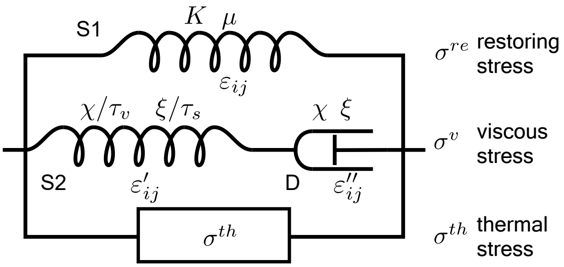

Figure 1.1: Schematics of the standard linear solid model. Total stress consists of restoring σ^{re}, viscous σ^{v}, and thermal σ^{th} components.

of viscous stress σ^{v}_{ij} proportional to a strain rate introduces losses with quadratic power dependence on acoustic frequency, but in several photoacoustic experiments relaxation damping which causes deviations from a quadratic dependence was observed [33–35, 75]. The relaxation damping behavior manifests in a noninstantaneous viscous stress response to the change of strain characterized by the relaxation time τ. To include relaxation damping, we use standard linear solid (SLS), also known as Zener model [76, 77], schematically depicted in Fig. 1.1. The spring S1 represents the static elasticity of a solid and thus is defined by bulk K and shear μ elastic moduli. The stress-strain relation in the spring S1 is described by Eq. 1.11. Since the stress in the spring S1 originates from the response of a solid to constant deformation, we will call it restoring stress σ^{re}. Spring S2 and dashpot D form the viscous stress σ^{v}. Without spring S2, the viscous stress would be defined just by Eq. 1.12 with viscous constants χ and ξ. The spring S2 introduces a relaxation type of acoustic attenuation. The bulk and shear moduli of the spring S2 can be defined as χ/τ_v and ξ/τ_s, where τ_v and τ_s are relaxation times of volumetric and shear deformation, respectively. The parallel connection of elements in Fig. 1.1 implies equality of strain and summation of stress values and vice versa for serial connection. Thus, the viscous stress according to the model shown in Fig. 1.1 is determined by the system of equations:

$$\begin{aligned}
\sigma^{v}_{ij} &= \frac{\chi}{\tau_v}\delta_{ij}\varepsilon'_{kk} + 2\frac{\xi}{\tau_s}\left(\varepsilon'_{ij} - \frac{1}{3}\delta_{ij}\varepsilon'_{kk}\right), \\
\sigma^{v}_{ij} &= \chi\delta_{ij}\dot{\varepsilon}''_{kk} + 2\xi\left(\dot{\varepsilon}''_{ij} - \frac{1}{3}\delta_{ij}\dot{\varepsilon}''_{kk}\right), \\
\varepsilon_{ij} &= \varepsilon'_{ij} + \varepsilon''_{ij},
\end{aligned} \tag{1.14}$$

where ε'_{ij} and ε''_{ij} are the strain values in the spring S2 and the dashpot D, respectively. To make this system more practical to use, one would prefer to exclude ε'_{ij} and ε''_{ij} variables and operate only with total strain ε_{ij}. This can be easily done for non-diagonal components of $\sigma^v_{ij,i\neq j}$:

$$\left.\begin{aligned}\sigma^v_{ij} &= 2\frac{\xi}{\tau_s}\varepsilon'_{ij}\\ \sigma^v_{ij} &= 2\xi\dot{\varepsilon}''_{ij}\end{aligned}\right. \quad\Rightarrow\quad \sigma^v_{ij}+\tau_s\dot{\sigma}^v_{ij}=2\xi\dot{\varepsilon}_{ij},\quad i\neq j. \tag{1.15}$$

Meanwhile, for diagonal components of $\sigma^v_{ij,i=j}$ equations become

$$\begin{aligned}\sigma^v_{ij} &= \left(\frac{\chi}{\tau_v}+\frac{4\xi}{3\tau_s}\right)\varepsilon'_{ij}+\left(\frac{\chi}{\tau_v}-\frac{2\xi}{3\tau_s}\right)\varepsilon'_{kk}=\eta_1\varepsilon'_{ij}+\zeta_1\varepsilon'_{kk}, \\ \sigma^v_{ij} &= \left(\chi+\frac{4}{3}\xi\right)\dot{\varepsilon}''_{ij}+\left(\chi-\frac{2}{3}\xi\right)\dot{\varepsilon}''_{kk}=\eta_2\dot{\varepsilon}''_{ij}+\zeta_2\dot{\varepsilon}''_{kk}.\end{aligned}\qquad \begin{aligned}&i=j,\\ &k\neq i\end{aligned} \tag{1.16}$$

Since the ratio η_1/η_2 is not equal to the ratio ζ_1/ζ_2, Eqs. 1.16 can not be transformed similar to Eqs. 1.15. However, the system of Eqs. 1.16 must hold for any values of ε_{ij}. This allows us to split it into two independent sets of equations:

$$\left.\begin{aligned}\sigma^{v1}_{ij} &= \eta_1\varepsilon'_{ij}\\ \sigma^{v1}_{ij} &= \eta_2\dot{\varepsilon}''_{ij}\end{aligned}\right. \quad\Rightarrow\quad \sigma^{v1}_{ij}+\frac{\eta_2}{\eta_1}\dot{\sigma}^{v1}_{ij}=\eta_2\dot{\varepsilon}_{ij},\qquad i=j; \tag{1.17}$$

and

$$\left.\begin{aligned}\sigma^{v2}_{ij} &= \zeta_1\varepsilon'_{kk}\\ \sigma^{v2}_{ij} &= \zeta_2\dot{\varepsilon}''_{kk}\end{aligned}\right. \quad\Rightarrow\quad \sigma^{v2}_{ij}+\frac{\zeta_2}{\zeta_1}\dot{\sigma}^{v2}_{ij}=\zeta_2\dot{\varepsilon}_{kk},\qquad \begin{aligned}&i=j,\\ &k\neq i.\end{aligned} \tag{1.18}$$

Where the diagonal components of total viscous stress are $\sigma^v_{ij,i=j}=\sigma^{v1}_{ij}+\sigma^{v2}_{ij}$.

Now, we have all the equations to describe elastic wave propagation with losses in isotropic solids. The complete set of equations is

$$\begin{aligned}
&\sigma_{ij}=\sigma^{re}_{ij}+\sigma^v_{ij}+\sigma^{th}_{ij}, && \rho\frac{\partial^2 u_i}{\partial t^2}=\frac{\partial\sigma_{ik}}{\partial x_k},\\
&\sigma^{th}_{ij}=-3K\alpha\delta_{ij}\Delta T_l, && \varepsilon_{ij}=\frac{1}{2}\left(\frac{\partial u_i}{\partial x_j}+\frac{\partial u_j}{\partial x_i}\right),\\
&\sigma^{re}_{ij}=K\delta_{ij}\varepsilon_{kk}+2\mu\left(\varepsilon_{ij}-\frac{1}{3}\delta_{ij}\varepsilon_{kk}\right), &&\\
&\sigma^v_{ij}=\sigma^{v1}_{ij}+\sigma^{v2}_{ij}, &&\\
&\sigma^{v1}_{ij}+\frac{\eta_2}{\eta_1}\dot{\sigma}^{v1}_{ij}=\eta_2\dot{\varepsilon}_{ij}, && i=j\\
&\sigma^{v2}_{ij}+\frac{\zeta_2}{\zeta_1}\dot{\sigma}^{v2}_{ij}=\zeta_2\dot{\varepsilon}_{kk,k\neq i}, &&\\
&\sigma^v_{ij}+\tau_s\dot{\sigma}^v_{ij}=2\xi\dot{\varepsilon}_{ij}. && i\neq j
\end{aligned} \tag{1.19}$$

ATTENUATION OF ELASTIC WAVES

Let us find out the attenuation behavior of elastic waves that exist in the model described by Eqs. 1.19. As an example we will consider longitudinal waves propagating along the z axis. However, the same analysis is applicable for shear waves. Considering only an ε_{zz} strain component and substituting solutions in the form $a = a_0 \exp(ikz - i\omega t)$ into Eqs. 1.19 we can get a dispersion relation:

$$k^2 = \frac{\omega^2}{c_{l0}^2} \frac{1 - i\omega\tau_l}{1 - i\omega\tau_l(1 + \eta_2/M\tau_l)}. \tag{1.20}$$

Here, $M = K + 4\mu/3$ is the P-wave modulus, $c_{l0} = \sqrt{M/\rho}$ is the phase velocity of a longitudinal wave in case of no attenuation, and $\tau_l = \eta_2/\eta_1$ is the relaxation time of the longitudinal elastic wave. The complex wavenumber k can be represented with real and imaginary parts: $k = k' + ik''$. The real part determines phase velocity, while the imaginary part defines attenuation. In the case of low attenuation, $k' \gg k''$ holds, which in combination with Eq. 1.20 gives condition:

$$\frac{\frac{\eta_2}{M\tau_l}\omega\tau_l}{1 + \omega^2\tau_l^2(1 + \frac{\eta_2}{M\tau_l})} = \frac{xy}{1 + y^2(1 + x)} \ll 1, \tag{1.21}$$

where we use notations $x = \eta_2/M\tau_l$ and $y = \omega\tau_l$. For $x \ll 1$ condition 1.21 holds for any y and thus for any acoustic frequency. From Eq. 1.20 the square of real part k'^2 is

$$k'^2 = \frac{\omega^2}{2c_{l0}^2(1 + y^2(1 + x)^2)} \left(1 + y^2(1 + x) + \sqrt{(1 + y^2(1 + x))^2 + x^2y^2}\right). \tag{1.22}$$

Expanding the last equation into Taylor series for $x = 0$ we get:

$$k'^2 \approx \frac{\omega^2}{2c_{l0}^2}\left(2 - \frac{2y^2}{y^2 + 1}x\right); \qquad k' = \frac{\omega}{c_{l0}}\sqrt{1 - \frac{\omega^2\tau_l^2}{1 + \omega^2\tau_l^2}\frac{\eta_2}{\tau_l M}}. \tag{1.23}$$

Therefore, the phase velocity is

$$c_l = c_{l0}/\sqrt{1 - \frac{\omega^2\tau_l^2}{1 + \omega^2\tau_l^2}\frac{\eta_2}{\tau_l M}} \approx c_{l0}\left(1 + \frac{\eta_2}{2\tau_l M}\frac{\omega^2\tau_l^2}{1 + \omega^2\tau_l^2}\right). \tag{1.24}$$

Repeating the same procedure for the imaginary part k'' of the wavenumber we get:

$$k''^2 = \frac{\omega^2}{2c_{l0}^2(1+y^2(1+x)^2)}\left(-1-y^2(1+x)+\sqrt{(1+y^2(1+x))^2+x^2y^2}\right) \approx$$
$$\approx \frac{\omega^2}{2c_{l0}^2}\left(\frac{y^2}{(y^2+1)^2}x^2-\frac{3y^4}{2(y^2+1)^3}x^3\right); \tag{1.25}$$

$$k'' = \frac{\eta_2}{2\rho c_{l0}^3}\frac{\omega^2}{1+\omega^2\tau_l^2}\sqrt{1-3\frac{\omega^2\tau_l^2}{1+\omega^2\tau_l^2}\frac{\eta_2}{\tau_l M}}. \tag{1.26}$$

Now, by using the expression for phase velocity from Eq. 1.24 and considering that $\left(\sqrt{1-ax}\right)^3 \approx \sqrt{1-3ax}$, we obtain an attenuation coefficient for longitudinal elastic waves:

$$\beta_l = \frac{\eta_2}{2\rho c_l^3(\omega)}\frac{\omega^2}{1+\omega^2\tau_l^2}. \tag{1.27}$$

In the same way we can derive an attenuation coefficient for shear waves:

$$\beta_s = \frac{\xi}{2\rho c_s^3(\omega)}\frac{\omega^2}{1+\omega^2\tau_s^2}, \tag{1.28}$$

where c_s is the frequency-dependent phase velocity of a shear wave.

The two well-known intrinsic mechanisms of acoustic losses in solids are thermoelastic damping and phonon viscosity loss. Thermoelastic damping happens due to temperature differences in compressed and expanded regions. The heat conductance leads to irreversible energy dissipation and, therefore, attenuation of acoustic waves. This type of loss occurs only for longitudinal acoustic waves since shear waves do not cause volume change. The attenuation coefficient for thermoelastic losses is [74, 77]

$$\beta_{therm} = \frac{\varkappa \rho T}{2c_l}\left(\frac{3\alpha}{C_p}\right)^2\left(1-\frac{4c_s^2}{3c_l^2}\right)^2\omega^2, \tag{1.29}$$

where $\varkappa$ is the thermal conductivity and C_p is the volumetric heat capacity at constant pressure. We can see that attenuation described by Eqs. 1.27 and 1.28 transforms into Eq. 1.29 when the following parameter values are used in Eqs. 1.19:

$$\begin{gathered}\tau_l = 0 \quad \Rightarrow \quad \eta_1 = \infty \quad \Rightarrow \quad \tau_s = \tau_v = 0, \\ \eta_2 = \varkappa \rho^2 c_l^2 T\left(\frac{3\alpha}{C_p}\right)^2\left(1-\frac{4c_s^2}{3c_l^2}\right)^2, \qquad \xi = 0.\end{gathered} \tag{1.30}$$

Another damping mechanism (phonon viscous loss) is caused by the interaction of acoustic and thermal phonons via anharmonicity of the interatomic potential [77, 78]. If the mean free path of thermal phonons is much larger than the acoustic wavelength, i.e. $\omega\tau_{th} \gg 1$, where τ_{th} is the thermalization time of thermal phonons, the attenuation can be viewed as collisions of acoustic phonons with thermal phonons that are in thermal equilibrium. Otherwise, thermal phonons are considered to be in a homogeneous oscillating strain field caused by the acoustic wave. The strain field perturbs the phonon distribution function, meaning that the phonon gas is out of thermal equilibrium. The thermalization process removes energy from an acoustic wave, leading to its attenuation. The attenuation region with low acoustic frequencies $\omega\tau_{th} \not\gg 1$ is known as the Akhiezer region. For light-induced acoustic frequencies on the order of 100 GHz and thermalization time of several picoseconds, the condition, $\omega\tau_{th} \not\gg 1$ is well satisfied. Thus, we can consider the Akhiezer region of phonon viscous loss. The attenuation coefficient in this case is [78]

$$\beta_{Akh} = \frac{E_0(D_{l,s}/3)}{2\rho c_{l,s}^3}\frac{\omega^2\tau_{l,s}}{1+\omega^2\tau_{l,s}^2}, \tag{1.31}$$

where E_0 is the thermal energy density, and D is the nonlinearity constant obtained from the third-order elastic moduli. Subscripts "l" and "s" define longitudinal and shear waves, respectively. Similar to thermoelastic damping, Akhiezer damping can be modeled by using the following viscous parameters in Eqs. 1.19:

$$\begin{aligned} \eta_1 &= E_0(D_l/3); & \tau_s &= \tau_s; \\ \eta_2 &= E_0(D_l/3)\tau_l; & \xi &= E_0(D_s/3)\tau_s. \end{aligned} \tag{1.32}$$

Thermoelastic and Akhiezer damping can be considered independently or simultaneously by adding the corresponding equations for viscous stress into Eqs. 1.19.

1.1.3 DETECTION

As mentioned before, the detection of elastic waves is done by measuring the optical reflectivity change of the sample at different time delays after illumination by the pump. Various detection schemes can be implemented. In our experiments, the pump and probe beams are co-aligned and focused onto the sample (see Chapter 2 for a detailed description). The detected signal is the intensity of the reflected probe beam. Other experimental techniques might involve interferometric measurements that detect both amplitude and phase of reflected light [79, 80]. The transient grating experiments use two pump beams that interfere on the sample's surface creating periodic acoustics excitation [14, 20, 35, 81, 82]. The probe beam diffracts on this periodic pattern, and the intensity of the first diffraction order is detected. Regardless of the experimental technique, one needs to calculate the reflected field of the probe pulse from the sample with known strain distribution to model the detection.

The change of optical properties of the sample under strain carried by an elastic wave happens due to the photoelastic effect, which relates strain with changes in dielectric permittivity [77]:

$$\Delta\epsilon_{ij} = -\epsilon_{ik} p_{klmn} \varepsilon_{mn} \epsilon_{lj}, \tag{1.33}$$

where ϵ_{ij} is the nominal dielectric permittivity and p_{ijkl} is the tensor of complex photoelastic constants. In the case of an isotropic medium, the nominal dielectric permittivity is the scalar ϵ_0, and the tensor p_{ijkl} has only two independent components: P_{11} and P_{12}. Equation 1.33 can then be rewritten in the following way [36]:

$$\Delta\hat{\epsilon} = -\epsilon_0^2 \begin{pmatrix} P_{11}\varepsilon_{xx} + P_{12}(\varepsilon_{yy} + \varepsilon_{zz}) & P_{44}\varepsilon_{xy} & P_{44}\varepsilon_{xz} \\ P_{44}\varepsilon_{xy} & P_{11}\varepsilon_{yy} + P_{12}(\varepsilon_{xx} + \varepsilon_{zz}) & P_{44}\varepsilon_{yz} \\ P_{44}\varepsilon_{xz} & P_{44}\varepsilon_{yz} & P_{11}\varepsilon_{zz} + P_{12}(\varepsilon_{xx} + \varepsilon_{yy}) \end{pmatrix}, \tag{1.34}$$

where $P_{44} = (P_{11} - P_{12})/2$. The hat above the dielectric permittivity symbol designates its tensor nature.

Knowing the perturbation of dielectric permittivity, one can calculate the reflected field of the probe pulse. The last equation shows that under the strain field, the medium becomes anisotropic. Furthermore, the anisotropy axes' orientation depends on the strain's shear components. An additional complication comes when the spatial inhomogeneity of strain is on the scale below the wavelength of the probe light. In this case, one needs to solve Maxwell's equations to obtain the reflected field of the probe pulse. However, since the perturbation of dielectric permittivity is usually below 0.01 % and light propagation into the absorptive sample is limited by a couple of tens of nanometers, we approximate the reflected probe intensity by solving a one-dimensional problem at each surface point of the sample with subsequent incoherent integration of the reflected field over simulation domain. At each sample's surface point, we determine the effective refractive index variation as a function of depth with the use of Eq. 1.34 for a given probe polarization. The reflectivity from each point is obtained with the transfer matrix method [83], which considers longitudinal inhomogeneities of the refractive index.

In various photoacoustic studies, the sizes of pump and probe focus spots are significantly larger than the thickness of the sample. In this case, the whole process is assumed to be one-dimensional, and all the model equations become scalar [8, 11, 12, 36, 37, 84]. In particular, the change of dielectric permittivity becomes $\Delta\epsilon = -\epsilon^2 P_{12}\varepsilon$. We can relate $\Delta\epsilon$ to the change in refractive index n:

$$\begin{aligned} \epsilon = n^2 \quad &\Rightarrow \quad \Delta\epsilon \approx 2n\Delta n, \\ \Delta n = -\frac{1}{2}n^3 P_{12}\varepsilon &= \frac{\partial n}{\partial \varepsilon}\varepsilon. \end{aligned} \tag{1.35}$$

The coefficient $\partial n/\partial \varepsilon$ is called the strain-optic coefficient and is commonly used in photoacoustics literature. However, using the strain-optic coefficient is only convenient for one-dimensional problems when the strain has only longitudinal components along the elastic wave propagation.

Additional changes in reflectivity occur due to the temperature increase of the sample. For small temperature variations, the refractive index change can be approximated by a linear function of the temperature:

$$\Delta n = \frac{\partial n}{\partial T}\Delta T \qquad \Rightarrow \qquad \Delta\epsilon = 2\sqrt{\epsilon}\frac{\partial n}{\partial T}\Delta T. \tag{1.36}$$

Correction for thermal effects can be added to Eq. 1.34 or Eq. 1.35. It should be noted that the electrons and lattice are not in thermal equilibrium right after pump absorption. Furthermore, the electron temperature can reach several hundred or even thousand Kelvin. In this case, the refractive index response can be strongly non-linear [85] and Eqs. 1.36 are not valid. For that reason, we try to fit experimental data to simulations only after several picoseconds when electrons are thermalized with the lattice.

1.1.4 ILLUSTRATIVE EXAMPLE OF A ONE-DIMENSIONAL CASE

For a more intuitive understanding of the processes involved in picosecond ultrasonics, it is helpful to illustrate a typical light-induced acoustic pulse and its corresponding optical response. Since this section is intended only for illustration, we will limit ourselves to the one-dimensional case in acoustically non-dissipative media. Furthermore, we neglect the material's thermal conductivity and assume that the energy from the pump pulse is instantaneously transferred to lattice heating. These simplifications enable an analytical solution of the elastic equations, allowing us to clearly observe how the shape of the acoustic pulse is formed.

TYPICAL SHAPE OF LIGHT-INDUCED STRAIN PULSES

To begin with, let us consider a scenario that may initially seem more complex than generating an acoustic pulse on the surface of an opaque material. Specifically, assume a double-layered sample where the bottom layer is opaque and the top layer is transparent (see Fig. 1.2a). Both layers possess identical elastic properties and densities, making them equivalent in terms of acoustic wave propagation. The laser pump pulse passes through the transparent layer without any losses and is absorbed by the opaque layer. This absorption creates an exponentially decaying temperature profile within the optical penetration depth of the pump. The resulting temperature increase induces thermal strain (expansion) that follows the same exponential spatial dependence. Since thermal expansion occurs over a finite time, defined by the speed of sound, two compression pulses are generated, propagating in opposite directions, as illustrated in Fig. 1.2a. These strain pulses retain the spatial shape of

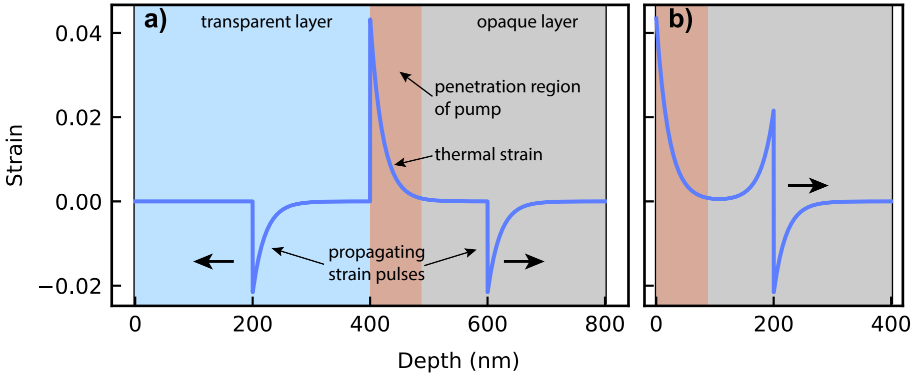

Figure 1.2: Spatial profile of laser-induced strain pulses at 20 ps after excitation. a) Generation of two compression pulses at the interface of two elastically equivalent materials. b) Strain pulse generated at the free surface. Parameters used in simulation: refractive index of opaque material $n = 1.5 + i3.0$, longitudinal speed of sound $c_{l0} = 10\,\mathrm{km/s}$, and pump wavelength $\lambda = 800\,\mathrm{nm}$.

the thermal strain but have opposite signs. From this example, we can deduce the shape of the strain pulse generated at the free surface of an opaque material. This situation is nearly identical to the previous one, except that the strain pulse, which would otherwise propagate into the transparent layer, is immediately reflected at the free surface. Upon reflection, the pulse undergoes a sign flip due to the free boundary condition, resulting in the formation of a complex bipolar strain pulse, as shown in Fig. 1.2b. It can also be noted that when the transparent and opaque layers possess different elastic properties, the strain pulse propagating into the transparent layer undergoes partial reflection at the interface between the two materials. The amplitude and phase (sign) of the reflected pulse are determined by the acoustic impedance mismatch at the interface [11].

The change of lattice temperature can be derived using the Beer-Lambert law for optical absorption:

$$\Delta T_l(z) = \frac{(1-R)F}{C_l \zeta_0} e^{-z/\zeta_0}, \tag{1.37}$$

where R is the optical intensity reflection coefficient, F is the pump fluence, C_l is the volumetric heat capacity, and $\zeta_0 = \lambda_0 / 4\pi\kappa_0$ is the optical penetration depth defined by optical wavelength λ_0 and imaginary part of refractive index κ_0. By using Eq. 1.37 in the initial condition for thermal stress, one can get an analytical solution to describe the strain field evolution shown in Fig. 1.2b [36]:

$$\varepsilon = \varepsilon_0 e^{-z/\zeta_0} - \frac{\varepsilon_0}{2}\left[e^{-(z+c_{l0}t)/\zeta_0} + e^{-|z-c_{l0}t|/\zeta_0}\operatorname{sgn}(z-c_{l0}t)\right], \quad z > 0; \tag{1.38}$$

where $\varepsilon_0 = 3K\alpha(1-R)F/C_l\zeta_0\rho c_{l0}$. The first term in the last equation determines nonpropagating thermal strain, and the second term corresponds to a propagating strain pulse. This bipolar pulse consists of two oppositely phased truncated exponents with a decay length ζ_0 equal to the penetration depth of the pump. Note that the propagating term itself consists of the two components enclosed in square brackets in Eq. 1.38. The second component inside the brackets defines the bipolar pulse that propagates away from the surface as shown in Fig. 1.2b. However, at time zero, this bipolar pulse is cut in half by the free surface, and its trailing half is mirrored over the interface with a corresponding sign flip. Therefore, the first component in square brackets in Eq. 1.38 describes the compression pulse that propagates into the interface before it reflects and forms the trailing half of the bipolar strain pulse.

Taking into account heat conductivity, the finite rise time of the lattice temperature due to non-instantaneous electron-phonon coupling, and acoustic attenuation, would affect the shape of the strain pulse, leading to its temporal broadening and smoothing. However, the present example provides a good qualitative description of light-induced strain waves.

TYPICAL SHAPE OF ΔR SIGNALS

Now, let us examine the reflectivity change induced by the strain pulse described by Eq. 1.38 as it reaches the sample surface. Consider a half-space occupied by a solid with a known strain distribution, $\varepsilon(z \geqslant 0, t)$. For a small perturbation of the dielectric constant due to strain, the variation of the surface reflectance can be obtained analytically [8, 36]:

$$\frac{\Delta r(t)}{r_0} = \frac{4ik\tilde{n}}{1-\tilde{n}^2}\left(\frac{\partial n}{\partial \varepsilon} + i\frac{\partial \kappa}{\partial \varepsilon}\right)\int_0^{\infty} \varepsilon(z,t)e^{2ik\tilde{n}z}dz, \tag{1.39}$$

where r_0 is the unperturbed reflectance, $k = 2\pi/\lambda$ is the wavenumber of the probe light, $\tilde{n} = n + i\kappa$ is the complex refractive index for the probe light, and $\partial n/\partial \varepsilon + i\partial \kappa/\varepsilon$ is the complex strain-optic coefficient. Since in our experiments we measure the intensity of reflected probe light, we are more interested in the variation of reflectivity $\Delta R/R_0$, which relates to $\Delta r/r_0$ as

$$\frac{\Delta R}{R_0} = 2\mathrm{Re}\left(\frac{\Delta r}{r_0}\right). \tag{1.40}$$

Then, the Eq. 1.39 can be rewritten as [8, 36]

$$\Delta R(t) = \int_0^{\infty} f(z)\varepsilon(z,t)dz, \tag{1.41}$$

where

$$\begin{gathered} f(z) = f_0\left[\frac{\partial n}{\partial \varepsilon}\sin(2knz-\phi) + \frac{\partial \kappa}{\partial \varepsilon}\cos(2knz-\phi)\right]e^{-z/\zeta}, \\ f_0 = 8k\frac{\sqrt{n^2(n^2+\kappa^2-1)+\kappa^2(n^2+\kappa^2+1)}}{(n+1)^2+\kappa^2}, \quad \tan\phi = \frac{\kappa(n^2+\kappa^2+1)}{n(n^2+\kappa^2-1)}. \end{gathered} \tag{1.42}$$

Here, $\zeta = \lambda/4\pi\kappa$ is the penetration depth of the probe light. From Eq. 1.41, we see that the variation in reflectivity is determined by the integral of the strain profile weighted by the function $f(z)$, known as the sensitivity function. If the strain field is a propagating strain wave, then $\Delta R(t)$ can be interpreted as the convolution of the strain pulse with the sensitivity function. The sensitivity function itself is an exponentially decaying sinusoid (see the example in Fig. 1.3). This means that the $\Delta R(t)$ signal must exhibit periodic behavior, defined by the time it takes the strain pulse to travel through one spatial period of the sinusoidal component of $f(z)$. From Eq. 1.42, one can find that the oscillation period in the $\Delta R(t)$ signal is $T = \lambda/2nc_{l0}$. The physical origin of these oscillations is the Brillouin effect. The probe light is reflected both from the sample surface and from the moving strain pulse inside the sample. These two reflected beams interfere, and the resulting intensity of the reflected light varies periodically with the distance between the strain pulse and the sample surface.

Let us calculate the variation in reflectivity using the shape of the strain pulse obtained in the previous section. We will define $t = \tau_{ref}$ as the moment when the strain pulse reflects off the sample surface, which is located at $z = 0$. Then we can describe the strain pulse as follows:

$$\varepsilon(z,t) = \mathrm{sgn}(s)e^{-|s|/\zeta_0}, \quad s = \begin{cases} z + c_{l0}(t - \tau_{ref}), & t < \tau_{ref}. \\ z - c_{l0}(t - \tau_{ref}), & t \geqslant \tau_{ref}. \end{cases} \tag{1.43}$$

If we now use the last equation in Eqs. 1.39 and 1.40 we get

$$\frac{\Delta R}{R_0} = \mathrm{Re}\left[\frac{8i\tilde{n}}{(1-\tilde{n}^2)(\tilde{n}^2+\kappa'^2)}\frac{\partial \tilde{n}}{\partial \varepsilon}\left(i\tilde{n}e^{2iknc_{l0}|t|}e^{-c_{l0}|t|/\zeta} + \kappa' e^{-c_{l0}|t|/\zeta_0}\right)\right], \tag{1.44}$$

where $\kappa' = \kappa_0\lambda/\lambda_0$. As expected, we obtain an oscillating component defined by the first term in the round brackets. The periodicity and damping of this oscillation are directly inherited from the sensitivity function (Eq. 1.42) and defined by the speed of sound and the optical properties of the solid. The second term in round brackets of Eq. 1.41 is called the transient term. It follows the temporal shape of the strain pulse from Eq. 1.43. In Fig. 1.4, we show a typical reflectivity change curve, along with its transient and oscillating components. The relative contribution of these two terms to the total signal is defined by the optical parameters of the solid [36].

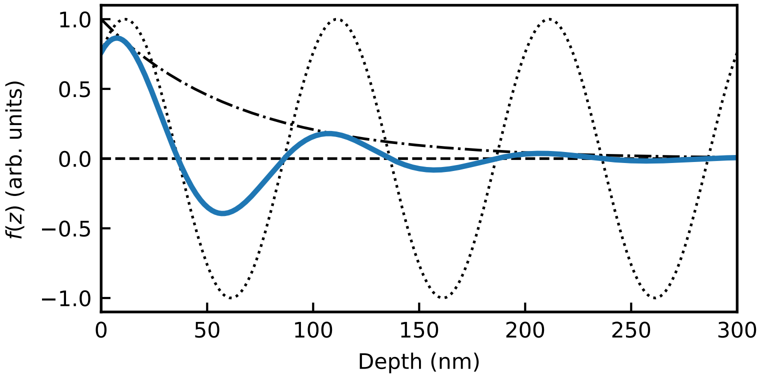

Figure 1.3: Normalized sensitivity function $f(z)$ calculated using the following optical parameters: wavelength of probe light $\lambda = 400\,\mathrm{nm}$, refractive index for probe light $\tilde{n} = 2.0 + i0.5$, and strain-optic coefficient $\partial\tilde{n}/\partial\varepsilon = 1.0 + i3.0$. The dotted and dash-dotted lines represent sinusoidal and exponentially decaying terms, respectively.

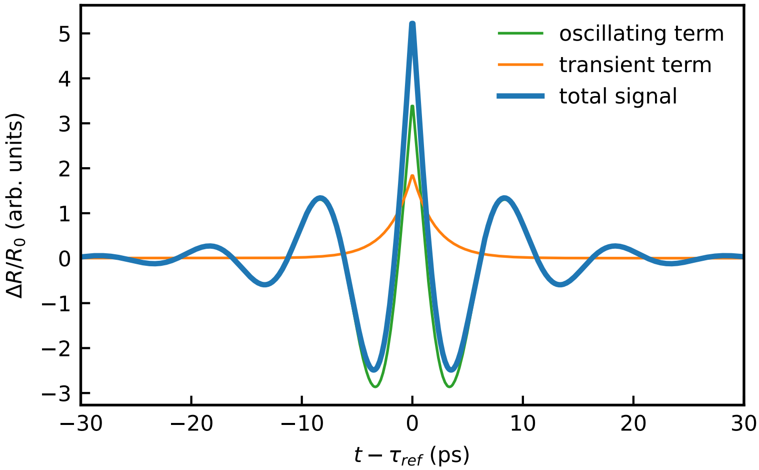

Figure 1.4: Reflectivity change calculated with the use of the same sensitivity function as in Fig. 1.3 and the strain pulse described in Fig. 1.2b.

1.2 NUMERICAL SIMULATIONS

1.2.1 FINITE-DIFFERENCE TIME-DOMAIN METHOD

To solve numerically Eqs. 1.3 and Eqs. 1.19 we use the finite-difference time-domaine (FDTD) method [86, 87]. Like any finite difference method, FDTD approximates time and spatial derivatives using finite differences. Due to the staggering scheme proposed by Yee [86], FDTD is very convenient and intuitive for solving hyperbolic partial differential equations (HPDE). Since wave processes are usually described by HPDEs, FDTD has become a common tool for modeling electromagnetic and acoustic waves.

Consider a one-dimensional physical model that contains two entities: A and B. Suppose A and B obey the following laws:

$$\frac{\partial A}{\partial t} = k\frac{\partial B}{\partial x}, \qquad \frac{\partial B}{\partial t} = p\frac{\partial A}{\partial x}. \tag{1.45}$$

One can see that these two equations can be easily transformed into well-known wave equations: $\partial^2 A/\partial t^2 = kp\partial^2 A/\partial x^2$ and $\partial^2 B/\partial t^2 = kp\partial^2 B/\partial x^2$, where $\sqrt{kp} = c$ is the phase velocity of wave propagation. To discretize Eqs. 1.45, we need to sample A and B in time and space. If the corresponding grid spacings are Δt and Δx, the sampled values will be

$$A(t,x) = A(q\Delta t, m\Delta x) = A[q;m], \qquad B(t,x) = B(q\Delta t, m\Delta x) = B[q;m]. \tag{1.46}$$

Indices q and m correspond to temporal and spatial steps. If now we shift the sampling points of B by $\Delta t/2$ and $\Delta x/2$ with respect to A as it is shown in Fig. 1.5, we can approximate derivatives with central differences using only two sample

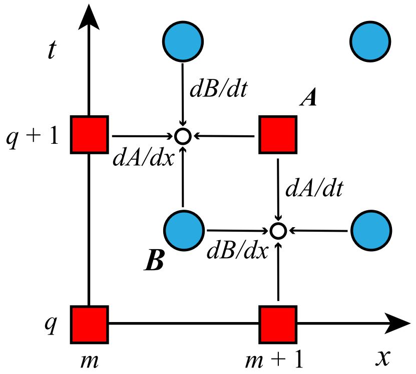

Figure 1.5: A staggered sampling scheme in the one-dimensional case. The horizontal and vertical axes represent spatial coordinates and time, respectively. Derivatives are approximated between the sampling nodes.

points while obtaining second-order accuracy. For the two points $[q+1/2;m+1]$ and $[q+1;m+1/2]$ shown in Fig. 1.5 the discretized Eqs. 1.45 will be:

$$\begin{aligned}\frac{A[q+1;m+1]-A[q;m+1]}{\Delta t} &= k\frac{B[q+1/2;m+3/2]-B[q+1/2;m+1/2]}{\Delta x},\\ \frac{B[q+3/2;m+1/2]-B[q+1/2;m+1/2]}{\Delta t} &= p\frac{A[q+1;m+1]-A[q+1;m]}{\Delta x}.\end{aligned} \tag{1.47}$$

From these equation we can retrieve update equations for A and B:

$$\begin{aligned}A[q+1;m] &= A[q;m]+\frac{k\Delta t}{\Delta x}\left(B[q+1/2;m+1/2]-B[q+1/2;m-1/2]\right),\\ B[q+3/2;m+1/2] &= B[q+1/2;m+1/2]+\frac{p\Delta t}{\Delta x}\left(A[q+1;m+1]-A[q+1;m]\right).\end{aligned} \tag{1.48}$$

After setting the initial conditions for $A[0;m]$ and $B[1/2;m+1/2]$, further calculations are done by iteratively applying update equations.

To obtain a stable solution, the speed of wave propagation must be lower than the slowest numerical speed (speed of information propagation). For the one-dimensional case, this numerical speed is $\Delta x/\Delta t$. Thus, to get a stable solution, we therefore need to satisfy the condition: $\Delta t \leqslant \Delta x/c$. For the n-dimensional case, this condition is known as the Courant condition [87]:

$$\Delta t \leqslant \frac{1}{c\sqrt{\sum_i^n \frac{1}{\Delta x_i^2}}}. \tag{1.49}$$

We should note that in the case of a medium with losses and dispersion, the phase velocity is frequency-dependent. Therefore, in the condition Eq. 1.49, one should consider the highest value of c for the simulated frequency bandwidth.

1.2.2 UPDATE EQUATIONS FOR THE TWO TEMPERATURE MODEL

We can apply the sampling strategy described in the previous subsection to discretize thermodynamic equations Eqs. 1.3. In these equations, electronic temperature T_e and electron heat flux $\mathbf{Q}_e$ are coupled in the same way as A and B in Eqs. 1.45. Thus, the sampling grid of $\mathbf{Q}_e$ should be shifted relative to the sampling grid of T_e by half of the sampling step both in time and space as it is shown for the one-dimensional case in Fig. 1.6a. Note that in the general case, $\mathbf{Q}_e$ has three components, and the spatial shift for each component should be done along the corresponding axis (Fig. 1.6b). Meanwhile, in the last equation of Eqs. 1.3, the time derivative of lattice temperature T_l is proportional to electronic temperature T_e. Hence, we spatially colocate sampling grids for T_l and T_e but stagger them in time (Fig. 1.6a).

Each equation in Eqs. 1.3 contains both physical quantities and their derivatives. In the applied discretization scheme, the derivative is defined between every two nodes of the sampling grid. If the physical quantity needs to be defined at the same position as its derivative, its value can be obtained by averaging the two neighbor nodes, e.g., $T_e[q;m] = (T_e[q-1/2;m] + T_e[q+1/2;m])/2$. Furthermore, Eqs. 1.3 are non-linear due to temperature dependence of electron heat capacity and heat conductivity. This results in non-linear discretized equations. However, the non-linearity is quadratic, and discretized equations can still be solved analytically to obtain explicit update equations:

$$\begin{aligned}
T_e[q+1/2;m_x;m_y;m_z] &= E\left(\sqrt{1+FZ}+1\right);\\
T_l[q+1;m_x;m_y;m_z] &= AT_l[q;m_x;m_y;m_z] + BT_e[q+1/2;m_x;m_y;m_z];\\
Q_e^x[q+1;m_x+1/2;m_y;m_z] &= CQ_e^x[q;m_x+1/2;m_y;m_z] - D^x J^x;\\
Q_e^y[q+1;m_x;m_y+1/2;m_z] &= CQ_e^y[q;m_x;m_y+1/2;m_z] - D^y J^y;\\
Q_e^z[q+1;m_x;m_y;m_z+1/2] &= CQ_e^z[q;m_x;m_y;m_z+1/2] - D^z J^z.
\end{aligned} \tag{1.50}$$

Where:

$$\begin{aligned}
Z = {} & R - GT_l[q;m_x;m_y;m_z] - S[q;m_x;m_y;m_z]\\
& - HT_e^2[q-1/2;m_x;m_y;m_z] + \frac{G}{2}T_e[q-1/2;m_x;m_y;m_z];\\
R = {} & \frac{Q_e^x[q;m_x+1/2;m_y;m_z] - Q_e^x[q;m_x-1/2;m_y;m_z]}{\Delta x}\\
& + \frac{Q_e^y[q;m_x;m_y+1/2;m_z] - Q_e^y[q;m_x;m_y-1/2;m_z]}{\Delta y}\\
& + \frac{Q_e^z[q;m_x;m_y;m_z+1/2] - Q_e^z[q;m_x;m_y;m_z-1/2]}{\Delta z};
\end{aligned} \tag{1.51}$$

$$\begin{aligned}
J^x &= \frac{T_e^2[q+1/2;m_x+1;m_y;m_z] - T_e^2[q+1/2;m_x;m_y;m_z]}{U + T_l[q;m_x+1;m_y;m_z] + T_l[q+1;m_x+1;m_y;m_z]};\\
J^y &= \frac{T_e^2[q+1/2;m_x;m_y+1;m_z] - T_e^2[q+1/2;m_x;m_y;m_z]}{U + T_l[q;m_x;m_y+1;m_z] + T_l[q+1;m_x;m_y+1;m_z]};\\
J^z &= \frac{T_e^2[q+1/2;m_x;m_y;m_z+1] - T_e^2[q+1/2;m_x;m_y;m_z]}{U + T_l[q;m_x;m_y;m_z+1] + T_l[q+1;m_x;m_y;m_z+1]};
\end{aligned} \tag{1.52}$$

$$U = T_l[q;m_x;m_y;m_z] + T_l[q+1;m_x;m_y;m_z];$$

and

$$\begin{aligned}
A &= \frac{2C_l - G\Delta t}{2C_l + G\Delta t}; & E &= \frac{G\Delta t}{2\gamma};\\
B &= \frac{2G\Delta t}{2C_l + G\Delta t}; & F &= \frac{8\gamma}{G^2\Delta t};\\
C &= \frac{2\tau_e - \Delta t}{2\tau_e + \Delta t}; & H &= \frac{\gamma}{2\Delta t}.\\
D^i &= \frac{4k_{eq}\Delta t}{(2\tau_e + \Delta t)\Delta x_i}; & &
\end{aligned} \tag{1.53}$$

Figure 1.6a shows the update process described by Eqs. 1.50. The update order is $T_e \to T_l \to \mathbf{Q}_e$. The temperature is defined in the center of the unit cell, while the heat flux is on the sides. This is when the staggered scheme becomes intuitively convenient. The difference of heat flux on the edges of a unit cell determines the change in energy of the cell, i.e., its temperature. Meanwhile, the difference in temperature of the two neighbor cells determines the heat flux across their common boundary. In this discretization scheme, the grid size of each heat flux component is one node larger along the corresponding axis, as shown in Fig. 1.6b. Note that one only needs to add update equations for corresponding heat flux components to go from one- to multi-dimensional cases.

Consider a boundary between two materials which, according to our sampling scheme, coincides with the sampling nodes for the heat flux (see Fig. 1.7). In general, there is no need to apply specific boundary conditions to material interfaces

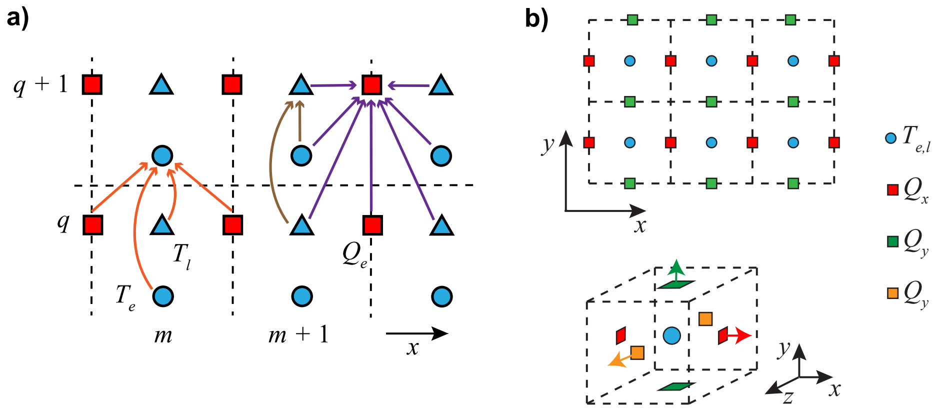

Figure 1.6: a) A sampling scheme for temperatures and heat flux in the one-dimensional case. The arrows visualize update procedure. b) A spatial grid (excluding time) in two- and three-dimensional cases. Temperatures are defined in the center while heat flux components are defined at the corresponding sides of the unit cell.

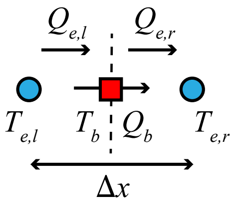

Figure 1.7: Interface of two materials goes through the heat flux node. Heat fluxes at the left and right sides must be equal.

if material constants are defined in all the nodes of the discretization grid. However, in our case, the grid of material constants is colocated with the temperature grid but not with the heat flux grid. To obtain material parameters between the materials grid nodes, let us apply a heat flux continuity restriction. Consider the material interface shown in Fig. 1.7. Let the temperature at the boundary be T_b. Then, according to Eq. 1.3, the left-side and right-side heat fluxes can be approximated as

$$\begin{aligned}\tau_{e,l}\frac{\partial Q_{e,l}}{\partial t}+Q_{e,l}&=-2k_{e,l}\frac{T_b-T_{e,l}}{\Delta x};\\ \tau_{e,r}\frac{\partial Q_{e,r}}{\partial t}+Q_{e,r}&=-2k_{e,r}\frac{T_{e,r}-T_b}{\Delta x};\\ \Delta T_e&=T_{e,r}-T_{e,l}.\end{aligned}\tag{1.54}$$

Subscripts l and r correspond to the left and right sides of the boundary, respectively. The heat fluxes and their rates must be equal at the left and right sides of the boundary i.e. $Q_{e,l}=Q_{e,r}=Q_b$. By summing the first two equations from Eqs. 1.54 we get

$$\tau_{eff}\frac{\partial Q_b}{\partial t}+Q_b=-k_{eff}\frac{\Delta T_e}{\Delta x},\tag{1.55}$$

where effective relaxation time and heat conductivity are

$$\tau_{eff}=\frac{\tau_{e,l}k_{e,r}+\tau_{e,r}k_{e,l}}{k_{e,l}+k_{e,r}},\qquad k_{eff}=\frac{2k_{e,l}k_{e,r}}{k_{e,l}+k_{e,r}}.\tag{1.56}$$

The edge nodes of the heat flux grid can not be calculated using update equations (see Fig. 1.6). However, various boundary conditions according to the chosen geometry can be applied. In our calculations, samples are usually thermally isolated in the longitudinal direction (direction of sound propagation) and either thermally isolated or periodically structured and assumed infinite in a transversal direction. Isolating boundary condition implies zero heat flux across the boundary surface. Meanwhile, in the case of periodic boundaries, the heat flux values on the edges of the grid are calculated using the update equations and temperature values on the opposite sides of the temperature grid.

1.2.3 UPDATE EQUATIONS FOR ELASTICS

Due to the specific geometry of the experimental samples studied in the current work, we consider either one or two-dimensional problems in our simulations. In this subsection, we will show update equations for the elastic systems described by Eqs. 1.19 in a two-dimensional case. We consider an elastic wave that propagates along the z axis, with y as the transverse coordinate. Expanding Eqs. 1.19 in two-dimensional cartesian coordinates gives equations for stress components:

$$\begin{aligned}
\sigma_{yy}^{re} &= M\varepsilon_{yy} + \lambda\varepsilon_{zz}, & \sigma_{yy}^{v1} + \frac{\eta_2}{\eta_1}\dot{\sigma}_{yy}^{v1} &= \eta_2\dot{\varepsilon}_{yy},\\
\sigma_{zz}^{re} &= \lambda\varepsilon_{yy} + M\varepsilon_{zz}; & \sigma_{yy}^{v2} + \frac{\zeta_2}{\zeta_1}\dot{\sigma}_{yy}^{v2} &= \zeta_2\dot{\varepsilon}_{zz},\\
\sigma_{yz}^{re} &= 2\mu\varepsilon_{yz}, & \sigma_{zz}^{v1} + \frac{\eta_2}{\eta_1}\dot{\sigma}_{zz}^{v1} &= \eta_2\dot{\varepsilon}_{zz},\\
\sigma_{yy}^{th} &= \sigma_{zz}^{th} = -3K\alpha\Delta T_l, & \sigma_{zz}^{v2} + \frac{\zeta_2}{\zeta_1}\dot{\sigma}_{zz}^{v2} &= \zeta_2\dot{\varepsilon}_{yy},\\
& & \sigma_{yz}^{v} + \tau_s\dot{\sigma}_{yz}^{v} &= 2\xi\dot{\varepsilon}_{yz},
\end{aligned} \tag{1.57}$$

where $M = K + 4\mu/3$ is the P-wave modulus and $\lambda = K - 2\mu/3$ is the Lame's first parameter. The equations for the strain components are:

$$\frac{\partial\varepsilon_{yy}}{\partial t} = \frac{\partial v_y}{\partial y}, \qquad \frac{\partial\varepsilon_{zz}}{\partial t} = \frac{\partial v_z}{\partial z}, \qquad \frac{\partial\varepsilon_{yz}}{\partial t} = \frac{1}{2}\left(\frac{\partial v_y}{\partial z} + \frac{\partial v_z}{\partial y}\right); \tag{1.58}$$

and the equations for the velocity components:

$$\begin{aligned}
\rho\frac{\partial v_y}{\partial t} &= \frac{\partial\sigma_{yy}^{re}}{\partial y} + \frac{\partial\sigma_{yy}^{v1}}{\partial y} + \frac{\partial\sigma_{yy}^{v2}}{\partial y} + \frac{\partial\sigma_{yy}^{th}}{\partial y} + \frac{\partial\sigma_{yz}^{re}}{\partial z} + \frac{\partial\sigma_{yz}^{v}}{\partial z},\\
\rho\frac{\partial v_z}{\partial t} &= \frac{\partial\sigma_{zz}^{re}}{\partial z} + \frac{\partial\sigma_{zz}^{v1}}{\partial z} + \frac{\partial\sigma_{zz}^{v2}}{\partial z} + \frac{\partial\sigma_{zz}^{th}}{\partial z} + \frac{\partial\sigma_{yz}^{re}}{\partial y} + \frac{\partial\sigma_{yz}^{v}}{\partial y}.
\end{aligned} \tag{1.59}$$

From the equations above, we can see that upon discretization, velocity and strain components should be staggered in time and space. Meanwhile, strain and stress components remain colocated. A spatial sampling grid is shown in Fig. 1.8. Diagonal components of strain and stress are placed in the center, while non-diagonal components are defined in the corners of the unit cell. Velocity components v_y and v_z are placed at the unit cell's y and z edges, respectively. The update order is *strain→ stress → velocity*. We get update equations for strain by discretizing Eqs. 1.58

according to the scheme shown in Fig. 1.8:

$$
\begin{aligned}
\varepsilon_{yy}[q+1,m_y,m_z] &= \varepsilon_{yy}[q,m_y,m_z] \\
&\quad + C_y(v_y[q+1/2,m_y+1/2,m_z] - v_y[q+1/2,m_y-1/2,m_z]), \\
\varepsilon_{zz}[q+1,m_y,m_z] &= \varepsilon_{zz}[q,m_y,m_z] \\
&\quad + C_z(v_z[q+1/2,m_y,m_z+1/2] - v_z[q+1/2,m_y,m_z-1/2]), \\
\varepsilon_{yz}[q+1,m_y+1/2,m_z+1/2] &= \varepsilon_{yz}[q,m_y+1/2,m_z+1/2] \\
&\quad + 0.5C_z(v_y[q+1/2,m_y+1/2,m_z+1] - v_y[q+1/2,m_y+1/2,m_z]) \\
&\quad + 0.5C_y(v_z[q+1/2,m_y+1,m_z+1/2] - v_z[q+1/2,m_y,m_z+1/2]).
\end{aligned}
\tag{1.60}
$$

Descretizing Eqs. 1.57 provides update equations for restoring stress:

$$
\begin{aligned}
\sigma^{re}_{yy}[q,m_y,m_z] &= M\varepsilon_{yy}[q,m_y,m_z] + \lambda\varepsilon_{zz}[q,m_y,m_z], \\
\sigma^{re}_{zz}[q,m_y,m_z] &= \lambda\varepsilon_{yy}[q,m_y,m_z] + M\varepsilon_{zz}[q,m_y,m_z], \\
\sigma^{re}_{yz}[q,m_y+1/2,m_z+1/2] &= 2\mu\varepsilon_{yz}[q,m_y+1/2,m_z+1/2];
\end{aligned}
\tag{1.61}
$$

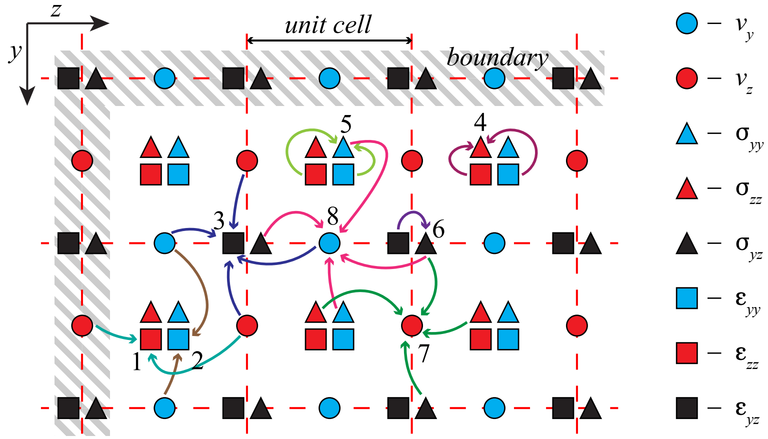

Figure 1.8: A spatial sampling scheme for elastics in the two-dimensional case. Arrows represent update equations. Numbers define update order.

and for viscous stress:

$$\begin{aligned}
\sigma_{yy}^{v1}[q+1,m_y,m_z] &= D_{vl}^1\sigma_{yy}^{v1}[q,m_y,m_z]+E_{vl}^1(\varepsilon_{yy}[q+1,m_y,m_z]-\varepsilon_{yy}[q,m_y,m_z]),\\
\sigma_{yy}^{v2}[q+1,m_y,m_z] &= D_{vl}^2\sigma_{yy}^{v2}[q,m_y,m_z]+E_{vl}^2(\varepsilon_{zz}[q+1,m_y,m_z]-\varepsilon_{zz}[q,m_y,m_z]),\\
\sigma_{zz}^{v1}[q+1,m_y,m_z] &= D_{vl}^1\sigma_{zz}^{v1}[q,m_y,m_z]+E_{vl}^1(\varepsilon_{zz}[q+1,m_y,m_z]-\varepsilon_{zz}[q,m_y,m_z]),\\
\sigma_{zz}^{v2}[q+1,m_y,m_z] &= D_{vl}^2\sigma_{zz}^{v2}[q,m_y,m_z]+E_{vl}^2(\varepsilon_{yy}[q+1,m_y,m_z]-\varepsilon_{yy}[q,m_y,m_z]),\\
\sigma_{yz}^{v}[q+1,m_y+1/2,m_z+1/2] &= D_{vs}\sigma_{yz}^{v}[q,m_y+1/2,m_z+1/2]\\
&\quad +E_{vs}(\varepsilon_{yz}[q+1,m_y+1/2,m_z+1/2]-\varepsilon_{yz}[q,m_y+1/2,m_z+1/2]).
\end{aligned} \tag{1.62}$$

Finally, from motion equations Eqs. 1.59 we get update equations for velocity:

$$\begin{aligned}
v_y[q+1/2,&m_y+1/2,m_z] = v_y[q-1/2,m_y+1/2,m_z]\\
&+A_y(\sigma_{yy}^{re}[q,m_y+1,m_z]-\sigma_{yy}^{re}[q,m_y,m_z]\\
&\quad+\sigma_{yy}^{v1}[q,m_y+1,m_z]-\sigma_{yy}^{v1}[q,m_y,m_z]\\
&\quad+\sigma_{yy}^{v2}[q,m_y+1,m_z]-\sigma_{yy}^{v2}[q,m_y,m_z]\\
&\quad+\sigma_{yy}^{th}[q,m_y+1,m_z]-\sigma_{yy}^{th}[q,m_y,m_z])\\
&+B_y(\sigma_{yz}^{re}[q,m_y+1/2,m_z+1/2]-\sigma_{yz}^{re}[q,m_y+1/2,m_z-1/2]\\
&\quad+\sigma_{yz}^{v}[q,m_y+1/2,m_z+1/2]-\sigma_{yz}^{v}[q,m_y+1/2,m_z-1/2]),\\
v_z[q+1/2,&m_y,m_z+1/2] = v_z[q-1/2,m_y,m_z+1/2]\\
&+A_z(\sigma_{zz}^{re}[q,m_y,m_z+1]-\sigma_{zz}^{re}[q,m_y,m_z]\\
&\quad+\sigma_{zz}^{v1}[q,m_y,m_z+1]-\sigma_{zz}^{v1}[q,m_y,m_z]\\
&\quad+\sigma_{zz}^{v2}[q,m_y,m_z+1]-\sigma_{zz}^{v2}[q,m_y,m_z]\\
&\quad+\sigma_{zz}^{th}[q,m_y,m_z+1]-\sigma_{zz}^{th}[q,m_y,m_z])\\
&+B_z(\sigma_{yz}^{re}[q,m_y+1/2,m_z+1/2]-\sigma_{yz}^{re}[q,m_y-1/2,m_z+1/2]\\
&\quad+\sigma_{yz}^{v}[q,m_y+1/2,m_z+1/2]-\sigma_{yz}^{v}[q,m_y-1/2,m_z+1/2]).
\end{aligned} \tag{1.63}$$

Where the constants are

$$\begin{aligned}
&A_y=\frac{\Delta t}{\rho\Delta y}, && A_z=\frac{\Delta t}{\rho\Delta z}, && D_{vl}^1=\frac{2\eta_2-\Delta t\eta_1}{2\eta_2+\Delta t\eta_1}, && E_{vl}^1=\frac{2\eta_1\eta_2}{2\eta_2+\Delta t\eta_1},\\
&B_y=\frac{\Delta t}{\rho\Delta z}, && B_z=\frac{\Delta t}{\rho\Delta y}, && D_{vl}^2=\frac{2\zeta_2-\Delta t\zeta_1}{2\zeta_2+\Delta t\zeta_1}, && E_{vl}^2=\frac{2\zeta_1\zeta_2}{2\zeta_2+\Delta t\zeta_1},\\
&C_y=\frac{\Delta t}{\Delta y}, && C_z=\frac{\Delta t}{\Delta z}, && D_{vs}=\frac{2\tau_s-\Delta t}{2\tau_s+\Delta t}, && E_{vs}=\frac{4\xi}{2\tau_s+\Delta t}.
\end{aligned} \tag{1.64}$$

For a given unit cell configuration, material parameters such as density and elastic moduli are defined in the grid nodes for diagonal components of stress and strain. To define material parameters for other spatially staggered grids, we do arithmetic averaging for densities and harmonic averaging for elastic moduli [88, 89]. This averaging automatically satisfies boundary conditions at material interfaces.

Different approaches can be implemented for the boundaries at the edges of the simulation domain: periodic boundary, perfectly matched layer, free boundary, and fixed boundary. As mentioned in the previous subsection, we use only periodic and free boundaries. Periodic boundary implies wrapping the domain by setting the same values for velocities, shear strain, and shear stress on the opposite sides of the grid. In the case of free boundaries, shear stress and shear strain are fixed to zero values. At the same time, velocity is calculated by assuming a half value for mass density and by considering only the first inner layer of the stress grid.

1.2.4 NUMERICAL DISPERSION AND ARTIFICIAL DAMPING

Applying any numerical method to solve differential equations that describe wave propagation corrupts the dispersion and attenuation properties of the system. As a result, the simulated wave packet undergoes a shape distortion that lacks physical significance [90]. For instance, if the wave packet propagates in a medium with linear dispersion, its shape must be conserved. However, the discretization of the space and time domains used in numerical calculations introduces nonlinearity in the dispersion relation. Thus, higher frequencies can not propagate with the same velocity as low frequencies. This velocity difference causes oscillatory behavior around steep edges of the wave packet, similar to the Gibbs phenomenon.

For illustrative purposes, let us see how discretization changes the dispersion relation in the case of a one-dimensional nondissipative medium. We start with the following system of differential equations describing an elastic wave propagation:

$$\begin{aligned} \frac{\partial \varepsilon}{\partial t} &= \frac{\partial v}{\partial x}, \\ \frac{\rho}{M}\frac{\partial v}{\partial t} &= \frac{\partial \varepsilon}{\partial x}. \end{aligned} \tag{1.65}$$

After the substitution of a planar wave in the form of $A = A_0 \exp(ikx - i\omega t)$, we get a dispersion relation for a nondiscretized system:

$$\begin{aligned} -i\omega\varepsilon_0 &= ikv_0 \\ -i\frac{\rho}{M}\omega v_0 &= ik\varepsilon_0 \end{aligned} \qquad \Rightarrow \qquad \frac{\omega}{k} = \sqrt{\frac{M}{\rho}} = c_{l0}. \tag{1.66}$$

Meanwhile, the discretized system for the FDTD method, system 1.65, is

$$\begin{aligned} \frac{\varepsilon[q+1/2,m]-\varepsilon[q-1/2,m]}{\Delta t} &= \frac{v[q,m+1/2]-v[q,m-1/2]}{\Delta x}; \\ \frac{\rho}{M}\frac{v[q+1,m+1/2]-v[q,m+1/2]}{\Delta t} &= \frac{\varepsilon[q+1/2,m+1]-\varepsilon[q+1/2,m]}{\Delta x}. \end{aligned} \tag{1.67}$$

If we now substitute a planar wave, we get

$$\begin{aligned} -\frac{\varepsilon_0 \sin(\omega\Delta t/2)}{\Delta t} &= \frac{v_0 \sin(k\Delta x/2)}{\Delta x} \\ -\frac{\rho}{M}\frac{v_0 \sin(\omega\Delta t/2)}{\Delta t} &= \frac{\varepsilon_0 \sin(k\Delta x/2)}{\Delta x} \end{aligned} \quad \Rightarrow \quad \frac{\sin^2(k\Delta x/2)}{\sin^2(\omega\Delta t/2)} = \frac{\Delta x^2}{\Delta t^2}\frac{\rho}{M}. \tag{1.68}$$

From the last equation, we can write out the frequency as a function of wavenumber:

$$\omega = \frac{2}{\Delta t}\arcsin\left(\sqrt{\frac{M}{\rho}}\frac{\Delta t}{\Delta x}\sin(k\Delta x/2)\right). \tag{1.69}$$

One can see that Eq. 1.69 transforms into Eq. 1.66 when the ratio $\Delta x/\Delta t$ exactly matches the speed of sound c_{l0} in the media. Figure 1.9 shows dispersion curves for different ratios $\Delta x/\Delta t$. We see that ω-k space is limited by the domain of the *arcsin* function that corresponds to spatial and temporal Nyquist frequencies $\pi/\Delta x$ and $\pi/\Delta t$, respectively. If $\Delta x/\Delta t \neq c_{l0}$, the dispersion curve deviates from the linear behavior. Furthermore, this deviation increases with spatial frequency. The

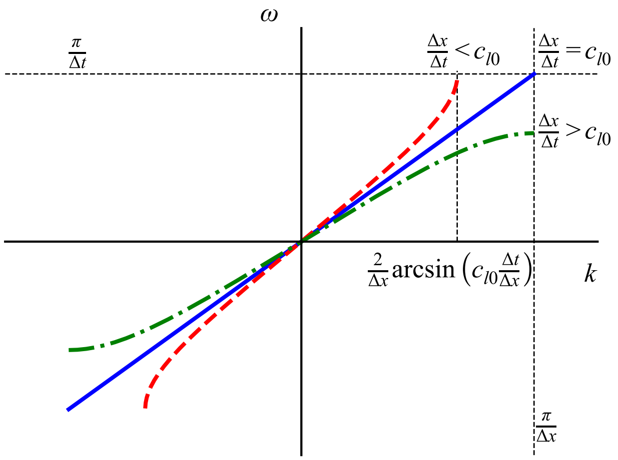

Figure 1.9: Dispersion curves for different values of $\Delta x/\Delta t$.

case of $\Delta x/\Delta t < c_{l0}$ is of particular interest. As shown in Section 1.2.1, this case violates the Courant condition Eq. 1.49, causing instability in numerical calculations. From Fig. 1.9, we can see that at $k\Delta x = 2\arcsin(\sqrt{M\Delta t^2/\rho\Delta x^2})$ temporal frequency ω reaches the Nyquist limit. This means that higher spatial frequencies in the range $2\arcsin(\sqrt{M\Delta t^2/\rho\Delta x^2}) < k\Delta x < \pi$ can not be correctly represented, implying instability in numerical calculations.

Notably, the same stability criterion can be obtained by applying the Von Neumann stability analysis [91] (also known as spectral stability analysis). Let us analyze Eqs. 1.67 after substituting the following trial solutions:

$$\varepsilon[q,m] = \varepsilon_0 \lambda^q \exp(ik\Delta x m), \qquad v[q,m] = v_0 \lambda^q \exp(ik\Delta x m). \tag{1.70}$$

Here, λ is a complex amplification factor. For the system to remain stable, the condition $|\lambda| \leqslant 1$ must hold. Without loss of generality, we set $q = 0$ and $m = 0$. The system 1.67 then becomes

$$\begin{aligned} \frac{\varepsilon_0}{\Delta t}(\lambda^{1/2} - \lambda^{-1/2}) &= \frac{v_0}{\Delta x}(e^{ik\Delta x/2} - e^{-ik\Delta x/2}), \\ \frac{\rho}{M}\frac{v_0}{\Delta t}(\lambda - 1)e^{ik\Delta x/2} &= \frac{\varepsilon_0}{\Delta x}(e^{ik\Delta x} - 1)\lambda^{1/2}. \end{aligned} \tag{1.71}$$

Multiplying these two equations yields

$$\lambda + \frac{1}{\lambda} = 2 - 4\frac{M}{\rho}\frac{\Delta t^2}{\Delta x^2}\sin^2(k\Delta x/2). \tag{1.72}$$

Analysis of this expression shows that $|\lambda| \leqslant 1$ holds for any value of k only if $\Delta x/\Delta t \geqslant c_{l0}$. Conversely, if $\Delta x/\Delta t < c_{l0}$, then $|\lambda| \leqslant 1$ holds only when $|k\Delta x| \leqslant 2\arcsin(\sqrt{M\Delta t^2/\rho\Delta x^2})$. This result is consistent with the dispersion curve shown in Fig. 1.69.

The presented case serves only an illustrative purpose, as it considers a nondissipative and nondispersive one-dimensional medium. A dissipative medium already exhibits nonlinear dispersion, making analytical analysis considerably more challenging. Furthermore, in multidimensional simulations, discretization introduces numerical directional anisotropy, meaning that the phase velocity becomes dependent on the direction of wave propagation. These effects prevent the selection of an optimized $\Delta x/\Delta t$ ratio that would completely eliminate numerical dispersion effects for all frequencies and propagation directions.

From Fig. 1.9, one can see that the deviation between the natural and numerical dispersion curves becomes more pronounced at higher frequencies. Consequently, one effective approach to mitigate numerical dispersion effects is to restrict the frequency bandwidth of the simulated fields. This can be achieved by introducing frequency-dependent "artificial attenuation" [92]. In Section 1.1.2, we introduced a physical model in which attenuation of elastic waves was represented through viscous stress. In that formulation, the viscosity of the medium is governed by viscous constants and the relaxation time. The resulting attenuation exhibits a quadratic dependence on frequency at low frequencies, while approaching a plateau in the high-frequency region. If we set the relaxation time $\tau = 0$, the attenuation reduces to a purely quadratic frequency dependence, which is particularly effective in suppressing high-frequency components. In the limit $\tau \to 0$, the attenuation coefficient from Eq. 1.27 becomes

$$\beta_l = \frac{\eta_2}{2\rho c_{l0}^3}\omega^2. \tag{1.73}$$

We now introduce the attenuation length δx, defined as the propagation distance over which the spatial Nyquist frequency component $k_N = \pi/\Delta x$ decays by a factor of e, i.e., $\beta_l(k_N)\,\delta x = 1$. From this condition, the viscous parameter η_2 can be expressed as

$$\frac{\eta_2}{2\rho c_{l0}^3}\left(\frac{\pi c_{l0}}{\Delta x}\right)^2 \delta x = 1 \quad \Rightarrow \quad \eta_2 = \frac{2\rho c_{l0}}{\pi^2}\frac{\Delta x^2}{\delta x}. \tag{1.74}$$

Figure 1.10 shows one-dimensional simulations of a light-induced strain pulse using various values of the $\Delta x/\Delta t$ ratio. We can see an emerging calculation instabil-

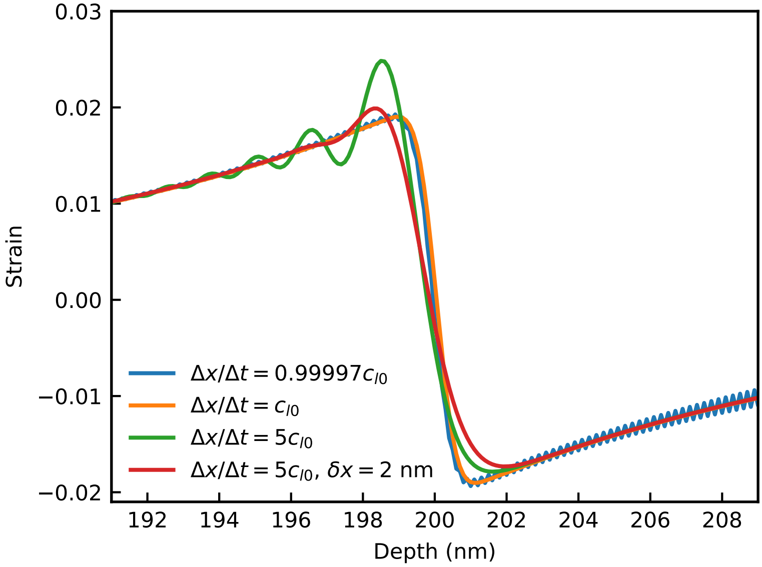

Figure 1.10: One-dimensional simulation of light-induced strain pulse in nondissipative and nondispersive medium for various values of $\Delta x/\Delta t$ ratio. A spatial grid spacing is fixed to $\Delta x = 0.1\,\mathrm{nm}$ in all simulation cases, while the time step is varied. The speed of sound is set to $c_{l0} = 10\,\mathrm{km/s}$. In the simulation represented by the red curve, an artificial damping is applied with $\delta x = 2\,\mathrm{nm}$.

ity when this ratio is slightly lower than the speed of sound (blue curve in Fig. 1.10). In contrast, the green curve in Fig. 1.10 represents the case where $\Delta x/\Delta t > c_{l0}$, showing oscillatory behavior near a steep gradient, which indicates a significant numerical dispersion effect. However, this oscillatory behavior is effectively suppressed by adding artificial attenuation with $\delta x = 2\,\mathrm{nm}$, as shown by the red curve in Fig. 1.10.

2

EXPERIMENTAL METHODS

INTRODUCTION

In the previous chapter, we introduced the theoretical essentials of picosecond ultrasonics. Now we can look at a practical implementation. The core of our experimental method is pump-probe spectroscopy, which is the primary experimental technique in picosecond ultrasonics [31, 36, 62, 94, 95]. This technique has been developed in the last decades as a tool for time-resolved studies of ultrafast processes such as molecular and electron dynamics, chemical kinetics, etc. [4]. In our case, pump laser pulses excite acoustic waves in a sample while probe pulses are used for detection. Compared to piezo-electric actuation and detection, this approach enables much higher frequency acoustic waves to be generated and detected. The frequency of light-induced acoustic waves can easily exceed tens of gigahertz, while piezo-electric emitters work in a megahertz range. Another advantage is non-invasiveness due to contact-free interactions.

In this chapter, we describe the practical implementation of the pump-probe technique as used in our current research.

2.1 PUMP-PROBE EXPERIMENTS IN PHOTOACOUSTICS

A typical setup for pump-probe measurements is demonstrated in Fig. 2.1a. The setup shown is designed for photoacoustic experiments; however, the concept also applies to other pump-probe experiments. The femtosecond laser source emits a pulse train at a specific repetition rate, typically in the kHz-MHz range. The laser beam is split into two arms: a pump arm and a probe arm. One usually applies orthogonal polarization or wavelength conversion to distinguish between the pump and probe beams, as shown in Fig. 2.1a. The pump pulse train repetitively excites

---

Parts of this chapter have been published in Rev. Sci. Instrum. 94, 103002 (2023) [93]

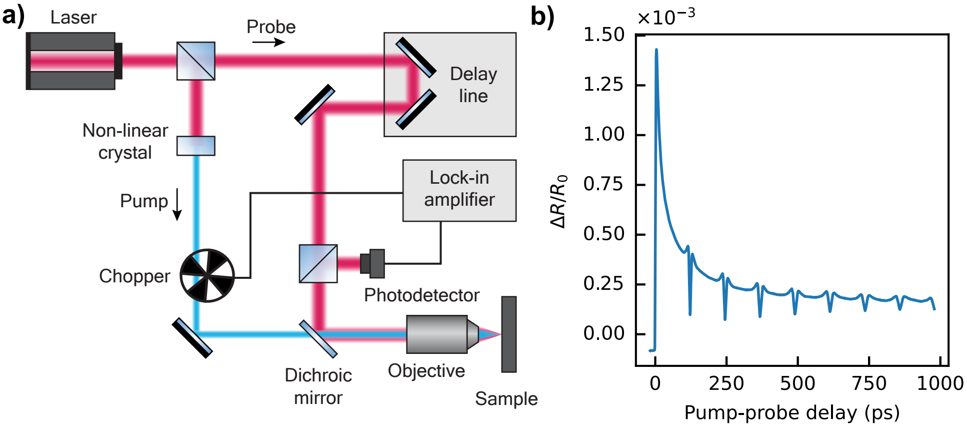

Figure 2.1: a) Schematic of a pump-probe setup for photoacoustics. b) Photoacoustic measurements on the 400 nm freestanding aluminium membrane. The acoustic wavepackets are visible as rapid variations in the normalized reflectivity ($\Delta R/R_0$).

specific dynamics in the sample of interest. It is important that the decay time of excited dynamics is significantly shorter than the time gap between neighboring pump pulses and fully reversible (i.e. the sample returns to its original state and is not permanently modified).

Meanwhile, laser pulses from the probe arm hit the sample with a delay controlled by the moving linear stage. Upon reflection from the sample, the probe pulses are detected by a photodetector. To suppress noise, lock-in detection is usually implemented by introducing a mechanical chopper in the pump arm. By observing the photodetector signal as a function of the stage position, one can monitor the dynamic processes that happen in the sample after pump excitation. In this scheme, the temporal resolution is fundamentally limited only by the duration of the probe and pump pulses.

Figure 2.1b shows a typical photoacoustic measurement obtained with the pump-probe technique. In this case, acoustic waves are excited in 400 nm thick aluminium freestanding membrane. Immediately after pump excitation, one observes a rapid and substantial change in the reflectivity of the sample. This change is caused by photo-excited electrons. Later, electrons thermalize with the lattice, leading to a rise in temperature. Due to thermal conductivity, the lattice temperature decays on the nanosecond timescale. This thermal effect is observed as a slowly varying background in Fig. 2.1b. The sequence of rapid drops in reflectivity change indicates a pump-induced strain pulse traveling back and forth in the membrane at the speed of sound.

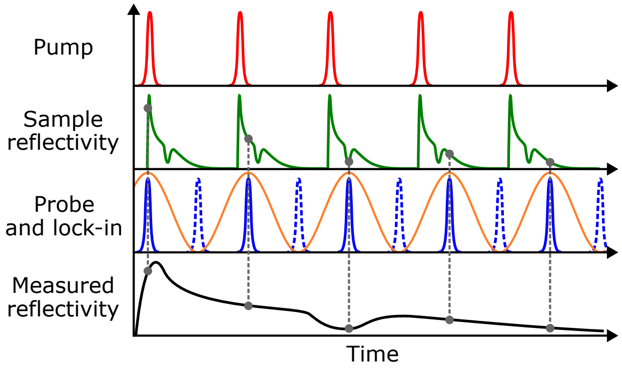

Figure 2.2: Schematic depiction of asynchronous optical sampling. The pump repeats slightly faster than half the probe repetition rate, causing an increasing pump-probe delay. Measuring the probe intensity then recovers the ultrafast dynamics in the sample reflectivity. The dashed probe pulses are not affected by the pump but are used for noise reduction with lock-in detection, as explained in the setup description. Figure is taken from [93].

2.2 MODULATED ASYNCHRONOUS OPTICAL SAMPLING

The pump-probe setup with mechanical delay stage shown in Fig. 2.1a has multiple drawbacks. The length of the delay line limits the pump-probe delay range. Furthermore, at large delay ranges, the system starts suffering from beam pointing variation and divergence changes. Additionally, the stage movement speed limitation does not allow fast delay scan measurements. These problems are eliminated in the asynchronous optical sampling (ASOPS) technique [96], where two separate but electronically synchronized lasers are used for pumping and probing. For the current research, we developed an ASOPS-based experimental apparatus for ultrafast pump-probe reflectivity measurements capable of reaching shot-noise-limited detection sensitivity. Below, we introduce technical details on the designed setup.

2.2.1 ASYNCHRONOUS OPTICAL SAMPLING

The concept of ASOPS is schematically depicted in Fig. 2.2. Each pump pulse induces the same reflectivity change in the sample, which is detected by a probe pulse. Because the pump repeats slightly faster than the probe, the delay between the probe and the pump slowly increases. In this way, the fast reflectivity dynamics are sampled at a different delay for each probe pulse. With a nominal repetition rate f_0 and an offset Δf, every probe pulse arrives $\Delta t \approx \Delta f / f_0^2$ later, giving an effective delay scan speed of $v = f_0 \times \Delta t \approx \Delta f / f_0$. The delay scan speed of ASOPS typically far exceeds that of mechanical delay lines. For example, scan speeds of $400\,\mathrm{ns/s}$ and higher are readily achievable, which would require a mechanical stage moving at $60\,\mathrm{m/s}$ for a single-reflection delay line.

Usually, the pump and probe in ASOPS run at similar repetition rates. Instead, in our setup, the pump runs at approximately half the probe repetition rate. This allows us to use lock-in detection at half the probe repetition rate, as indicated in Fig. 2.2, which reduces electronic noise.

In conventional ASOPS, the repetition rate offset of the pump is fixed, and many rapidly acquired traces are averaged together. This has the disadvantage that the resulting trace is as long as the pump pulse interval, making measurements of a short range in time inefficient. High-speed ASOPS systems with increased repetition rates of 1 to 10 GHz can already improve this inefficiency [97–103], but such systems do not have the flexibility to measure longer delay times as well. Instead, by modulating the repetition rate offset in time, the pump-probe delay can be alternated back and forth over the range of interest. Such a modified scanning scheme enables much greater efficiency in data collection. A similar approach has been explored before in terahertz radiation experiments [104–106]. However, our approach does not require delay time calibration and is easy to apply to ASOPS systems with a tunable repetition rate. An alternative efficient solution with synchronized lasers is to measure at a small repetition rate offset, slowly scanning the range of interest only once but with increased integration time per unit delay. This is similar to using a mechanical delay stage in a traditional pump-probe setup (as in Fig. 2.1a). Thus, we can apply three measurement schemes with our setup: Modulated ASOPS (MASOPS), conventional ASOPS, and single slow scan. We compared these three methods and found that the MASOPS scheme has the best measurement efficiency [93].

2.2.2 EXPERIMENTAL SETUP

Our setup for measuring laser-induced ultrafast photoacoustics is sketched in Fig. 2.3. The pump laser is a 1030 nm ytterbium fiber laser with 180 fs pulse duration at 50 MHz (Menlo Systems Orange). It is electronically synchronized to the free-running probe laser, an erbium fiber laser with 70 fs pulse duration at 100 MHz, from which we use the 780 nm second-harmonic output (Menlo Systems C-Fiber 780). The pump and probe are collinearly focused on the sample. A beam expander in the probe path ensures that the probe spot is smaller than the pump on the sample ($\sim 4\,\mu$m vs $\sim 8\,\mu$m, respectively).

Half of the reflected probe light is then detected in one port of a multimode fiber-coupled balanced detector, with a reference probe beam in the other port. An OD6 low-pass dichroic filter in the probe arm prevents any pump light from being detected. The fast balanced detector (500 MHz, Femto HBPR) has a 5 kV/A transimpedance gain, allowing for shot-noise-limited probe detection at mW-level intensities. In addition, a lock-in amplifier (Zurich Instruments UHFLI) filters and amplifies the detector signal at half the probe repetition rate. The lock-in output can

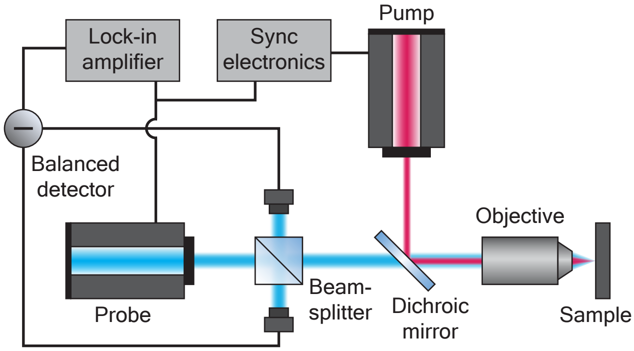

Figure 2.3: Sketch of the measurement setup. The pump and probe are collinearly focused on the sample. Half of the reflected probe light is coupled into a multimode fiber and detected by a fast detector, which is balanced with a reference probe beam. The detector signal is then filtered and amplified at half the probe rate.

either be saved directly or captured by an oscilloscope for trace averaging in the case of (M)ASOPS. Because the balanced detector also outputs a DC voltage, we can extract the relative reflectivity change as $\Delta R/R_0 = \sqrt{2} \cdot V_{\mathrm{RMS}}/V_{\mathrm{DC}}$ (see the following section). Here, V_{RMS} is the RMS voltage as measured by the lock-in amplifier, V_{DC} is the DC voltage, ΔR is the absolute reflectivity change, and R_0 is the reflectivity without the pump. We assume that any pump-induced effects have vanished before the secondary probe pulses (dashed in Fig. 2.2) are reflected.

The control electronics are shown schematically in Fig. 2.4. The pump and probe pulses are internally detected with fast photodiodes, and their repetition rate harmonics at 1 GHz are electronically bandpass filtered. A 20 MHz reference is subtracted from the probe's 1 GHz, after which the resulting 980 MHz is compared to the pump's 1 GHz, creating a 20 MHz intermediate frequency. This frequency is phase-locked via a proportional-integral-derivative (PID) loop to a digitally generated 20 MHz signal, which can be frequency and/or phase modulated to provide a modulated pump repetition rate. The PID loop with a 100 kHz bandwidth controls the pump laser with an intracavity mirror that can be moved in large steps by a stepper motor and fine-tuned with a piezo-element. Detecting pump and probe phases at 1 GHz increases sensitivity, as any phase fluctuations in the fundamentals are multiplied by the harmonic number (20 for the pump and 10 for the probe, respectively). Furthermore, the effect of phase noise in the 20 MHz reference is reduced by a factor of 10 as well, compared to phase detection at 100 MHz. The complete synchronization setup is a commercial system (Menlo Systems RRE-SYNCRO), with a jitter of 59 fs as measured by Menlo Systems. In practice, the time resolution is limited by the 180 fs pump pulse duration, which we have verified with a pump-probe intensity cross correlation on a two-photon GaP photodetector.

We have added an arbitrary waveform generator (AWG, Keysight 33522B) to allow for modulation of the frequency and phase offset. A frequency shift Δf or phase shift $\Delta\varphi$ of the AWG output will result in a repetition rate offset of $\Delta f/20$ or a phase shift of $\Delta\varphi/20$, respectively. Previously, the modulation was applied as a voltage offset to the PID loop, which requires accurate voltage-to-phase calibration [104] or a known repetitive signal [105]. Instead, in our approach, the modulation is essentially directly applied to the 1 GHz harmonic of the pump, giving a quantitative and calibration-free conversion to the resulting time delay scan. For example, a 1 Hz offset of the AWG results in a delay scan speed of 1 ns/s. Due to the AC voltage limitations of the intracavity piezo-element in the pump laser, the scan speed modulation is limited from -20 to $+20$ ns/s. Alternating traces of 1 ns long can, thus, be measured at a maximum rate of 20 traces per second.

With modulated ASOPS in our experiments, the pump usually runs at $+1$ Hz offset for $\tau/20$ s and then -1 Hz offset for $\tau/20$ s, where τ is the measured pump-probe delay range in nanoseconds. On average, the scan speed v is 20 ns/s. The modulation is applied via phase modulation, as frequency modulation otherwise results in a slight timing drift after every cycle with our AWG. A triangle wave defines the modulation waveform, with the transitions smoothed in order to prevent sharp PID input jumps. The normalized upswing $\hat{\phi}$ of the waveform is a piecewise

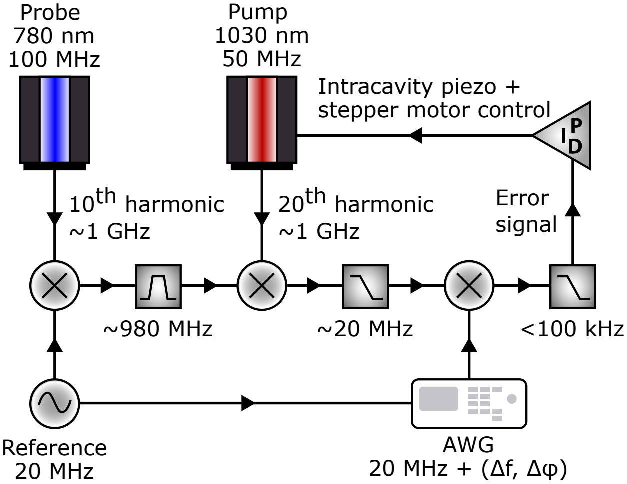

Figure 2.4: Block diagram of the MASOPS synchronization electronics. The pump and probe repetition rates are compared by their 1 GHz electronic harmonics at a 20 MHz offset. The resulting intermediate frequency is locked to the signal from an arbitrary waveform generator (AWG) via a PID-loop that controls an intracavity mirror in the pump laser. Any desired modulation can be added with the AWG. Figure is taken from [93].

continuous function of the normalized time $\hat{t}$, given by

$$\hat{\phi}\,(\hat{t}) = \begin{cases} (1-p)\frac{1-\cos(\omega\hat{t})}{2}, & 0 \leqslant \hat{t} \leqslant T, \\ \frac{1-a}{2} + a\hat{t}, & T < \hat{t} < 1-T, \\ 1-\hat{\phi}(1-\hat{t}), & 1-T \leqslant \hat{t} \leqslant 1. \end{cases} \tag{2.1}$$

Here, $0 \leqslant p < 1$ parametrizes how much of the total modulation range should be scanned linearly, with derived parameters $\omega = \pi + 2\pi/(1-p)$, $T = \pi/(2\omega)$, and $a = \omega(1-p)/2$. In our experiments, we typically use $p = 0.9$. Since $\hat{\phi}(0) = 0$ and $\hat{\phi}(1) = 1$, the waveform $\Delta\varphi(t)$ for any arbitrary modulation range or modulation rate can simply be found by scaling $\hat{\phi}$ or $\hat{t}$, respectively. The waveform is then combined with its mirror image to form the final updown modulation waveform that can be uploaded to the arbitrary waveform generator. As the phase maps directly to a pump-probe delay, in the analysis, the nonlinear cosine part can be interpolated to give a linear time delay axis. The conversion between a phase shift $\Delta\varphi$ and the effective pump-probe delay depends on the synchronization details, but in our case, 360° results in 1 ns of delay.

The lock-in amplifier uses a fourth-order cascaded digital lowpass filter, with its bandwidth set such that the equivalent measurement bandwidth is usually 1 THz. Thus, it is set to 20 kHz for 20 ns/s average scan speed. The sample rate of the data acquisition is approximately ten times higher to minimize aliasing.

EXTRACTING RELATIVE REFLECTIVITY

For a fixed pump-probe delay Δt, the probe repeats exactly twice as fast as the pump, as indicated in Fig. 2.2. In general, the n-th probe pulse that reflects from the sample has an intensity $I_n(t) = R(n)E_0\delta(t-\pi\tau/2)$, with $R(n)$ as the reflectivity, E_0 as the incident pulse energy, $\delta(t)$ as the Dirac delta function, and τ as the pump pulse interval. If the detector is linear and has infinite bandwidth, the unbalanced voltage in the sample beam detector is simply $V(t) = S \cdot I(t)$, with S being the detector sensitivity including experimental losses. We only need to consider the effect of a single pump pulse on the two following probe pulses since all signals are periodic with the pump. We assume that any pump-induced reflectivity modulation vanishes quickly so that the second probe pulse observes the unmodified reflectivity $R(1) = R_0$. The first probe pulse is, however, modified and observes $R(0) = R_0 + \Delta R$. With the pump pulse arriving at $t = -\Delta t$, the DC voltage over the two probe pulses until the next pump pulse is given by

$$\begin{aligned} V_{\mathrm{DC}} &= \frac{1}{\tau}\int\limits_{-\Delta t}^{-\Delta t+\tau} V(t)dt = \frac{SE_0}{\tau}\int\limits_{-\Delta t}^{-\Delta t+\tau}\left[R(0)\delta(t)+R(1)\delta(t-\tau/2)\right]dt \\ &= \frac{SE_0}{\tau}\left[2R_0+\Delta R(\Delta t)\right] \approx 2R_0\frac{SE_0}{\tau}, \end{aligned} \tag{2.2}$$

where we have assumed $\Delta R \ll R_0$. We always use the unbalanced DC voltage for V_{DC}, as the balanced signal has no DC component. The lock-in amplifier demodulates at half the probe repetition rate and in phase with the probe pulse train by multiplying the voltage with $\sqrt{2}\cos(2\pi t/\tau)$ and averaging. The resulting RMS voltage is given by

$$\begin{aligned} V_{\mathrm{RMS}} &= \frac{\sqrt{2}}{\tau}\int\limits_{-\Delta t}^{-\Delta t+\tau}\cos(2\pi t/\tau)V(t)dt = \frac{\sqrt{2}SE_0}{\tau}\left[R(0)-R(1)\right] \\ &= \sqrt{2}\Delta R(\Delta t)\frac{SE_0}{\tau}, \end{aligned} \tag{2.3}$$

With balancing, V_{RMS} is the same, but laser noise will be reduced. Note that, in practice, the detector bandwidth is finite. However, as long as the bandwidth is greater than $1/\tau$, V_{RMS} remains unchanged, as the signal at half the probe repetition rate will not be filtered out. Hence, we can reconstruct the relative reflectivity change by $\Delta R/R_0 = \sqrt{2}V_{\mathrm{RMS}}/V_{\mathrm{DC}}$.

3

UNDERSTANDING PHOTOACOUSTIC SIGNAL FORMATION IN THE PRESENCE OF TRANSPARENT THIN FILMS

INTRODUCTION

Strain-induced variation of the refractive index is the main mechanism of strain detection in ultrafast photoacoustic experiments. However, weak strain-optic coupling in many materials limits the application of photoacoustics as an imaging tool. A straightforward deposition of a transparent thin film as a top layer has previously been shown to provide signal enhancement due to elastic boundary effects [108]. In this chapter, we study photoacoustic signal formation in metal covered by thin transparent films of different thicknesses and demonstrate that in addition to boundary effects, the photoacoustic response is affected by optical effects caused by the presence of the top layer. The interplay of optical effects leads to a complex temporal signal shape that strongly depends on the thickness of the thin film.

3.1 CHALLENGE OF WEAK SIGNALS IN PHOTOACOUSTIC EXPERIMENTS

For the purpose of nanoscale imaging and detection through optically opaque materials, high-frequency ultrasound can become an intermediate carrier of information about buried nanostructures [21–23, 31]. As sound frequencies on the order of

---

This chapter has been published in Photoacoustics 38, 100617 (2024) [107] several hundred gigahertz correspond to an acoustic wavelength of only tens of nanometers in most materials, such acoustic waves may be used for high-resolution imaging [23, 26, 31]. Ultrafast photoacoustics (or picosecond ultrasonics) allows generation and detection of such high-frequency acoustic waves. These laser-induced acoustic waves propagate longitudinally into the sample and are reflected from any internal interfaces or structures. The resulting acoustic echoes cause refractive index variations near the surface of the sample that can be detected by a time-delayed probe laser pulse (Fig. 3.1(a)). The imaging or detection of internal structures of the sample of interest can be done by investigating the probe reflectivity change $\Delta R/R_0$ dependance on the pump-probe delay [21–23].

A weak strain-optic coupling in many materials and low strain amplitudes of laser-induced strain pulses lead to a very low reflectivity change obtained in experiments. To achieve a satisfactory signal-to-noise ratio, the measurement time needs to be long, limiting the application of photoacoustics in industry. Improving signal levels by increasing pump pulse energy is limited by the finite optical damage threshold of materials. In general, strategies to increase signal ideally result in a stronger coupling between the strain wave and the probe light. Therefore, a detailed understanding of such photoelastic interactions is important, and provides a route towards signal optimization and the design of improved photoacoustic transducers. Furthermore, in many applications the strain generation does not take place at the surface of a structure, but at the interface between an opaque material and a transparent coating layer. In such cases, the generated strain may travel into the transparent layer, resulting in additional photoacoustic signal contributions such as Brillouin oscillations and vibrations of transparent layer interfaces [10–12, 37, 49, 109]. A specific approach to increasing detection sensitivity is to add a partial reflector above the material under study, forming a Fabry-Perot resonator that can be designed to strongly enhance the optical response to strain variations [48]. Here, we study the photoacoustic response of metals covered by transparent thin films with a thickness at or below the spatial extent of the strain pulse. Such stack configurations are found in various applications, ranging from precision optical coatings to photoresists in nanolithography. The use of photoacoustic metrology in such applications requires a detailed understanding of the signal formation in the presence of thin transparent films. In previous experiments, we observed signal enhancements in such a geometry [108]. We now investigate the origin of this enhancement, and identify several contributions to the photoelastic interaction. The interplay between these effects results in a complex temporal response, with signals that differ considerably from the characteristic Brillouin oscillations observed in thicker transparent layers.

In the presence of a transparent layer, the total $\Delta R/R_0$ signal is made up of three contributions: a thickness change of the transparent layer, strain-induced refractive index variations in the transparent layer, and strain-induced refractive index variations in the opaque layer (Fig. 3.1(b)). For small changes of reflectivity, the total $\Delta R/R_0$ signal can be treated as a linear sum of these three contributions. An additional effect is that in the presence of a transparent top layer, the $\Delta R/R_0$ variation due to strain in the opaque layer itself will be different. We call this difference an optical coating effect of the transparent layer. Depending on material parameters such as strain-optic coupling and nominal refractive index, and the thickness of the transparent layer, the $\Delta R/R_0$ signal can be dominated by either of the three mentioned effects, leading to significant variations in signal shape and amplitude.

The deposited transparent top layer acts as a Fabry Perot interferometer (FPI) attached to the sample. When the strain wave returns to the sample surface it causes changes in FPI parameters, affecting the $\Delta R/R_0$ signals. An FPI-based detection system can significantly enhance detection sensitivity when designed for that purpose [48]. In our configuration, the strain wave propagates through the entire “interferometer”. Furthermore, FPI-type sensors are used for ultrasonic detection [110, 111] and photoacoustic imaging in biomedicine [112]. However, in biomedical applications, the optical pump pulse usually propagates into the sample and is absorbed by internal features of interest. Those features become sources of strain waves which are then detected on the sample surface. Also in that application, the FPI sensors themselves have no effect on the generation process of strain waves. Conversely, in our case, both the generation and detection of strain waves happen near the surface of the sample and any modification of the surface also influences strain generation.

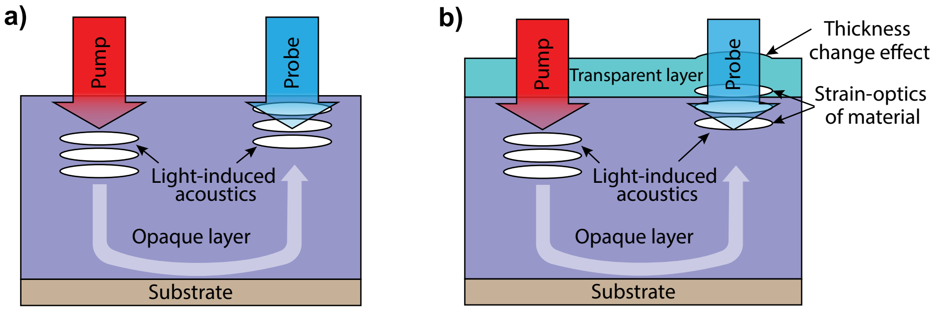

Figure 3.1: The schematic of the acoustics generation and detection process in a single opaque layer a) and a sample with a transparent top layer b).

3.2 RESEARCH METHODS

3.2.1 EXPERIMENTAL SETUP AND SAMPLES

Experiments were performed with a setup described in Chapter 2, which incorporates the pump-probe technique via modulated asynchronous optical sampling. The schematic of the setup is shown in Fig. 2.3. The pump source is an Ytterbium-doped fiber laser operating at 1030 nm wavelength, generating pulses with 180 fs duration at 50 MHz repetition rate (Menlo System Orange). The probe source is the frequency-doubled output of an Erbium-doped fiber laser at 780 nm wavelength, which emits 70 fs pulses at 100 MHz repetition rate (Menlo System C-Fiber 780). The probe pulses can be further upconverted to a wavelength of 390 nm through second harmonic generation in a beta-barium borate (BBO) crystal. The pump laser is electronically synchronized to the free-running probe laser, and the pump-probe delay can be tuned by adding a controlled offset to the pump laser repetition frequency [96].

Both pump and probe laser beams are collinearly focused by a microscope objective (Olympus LUCPLFLN20X, x20, N.A. 0.45) onto the sample surface. The reflected probe beam is filtered by a dichroic mirror and detected in one of the ports of a multimode fiber-coupled balanced detector (500 MHz, Femto HBPR), with a reference beam straight from the probe laser in the other port. The detector signal is then amplified by a lock-in amplifier (Zurich Instruments UHFLI) at 50 MHz demodulation frequency.

We use 780 nm and 390 nm probe light to measure strain-induced reflectivity change in aluminium and gold, respectively. Different probe wavelengths are used to maximize strain-optic coupling in a particular material.

The experimental samples shown in Fig. 3.2 were fabricated on glass coverslips (borosilicate 0.5 mm). To reduce losses of strain waves due to coupling into the glass substrate, a layer of 1 µm-thick PMMA layer was first deposited by spin coating. PMMA has a significantly lower acoustic impedance than the metals used in our experiments. Thus, a strain wave that propagates to the rear side of the metal layer

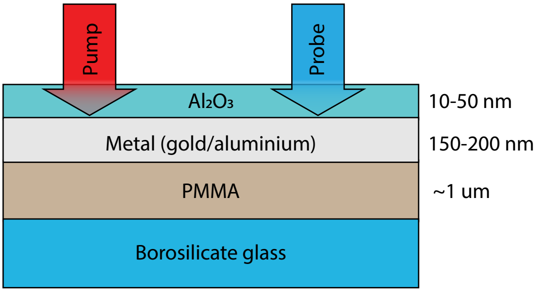

Figure 3.2: The schematic of an experimental sample.

is strongly reflected from the metal-PMMA interface. The metal layers (gold and aluminium) and transparent layers of varying thickness (Al_2O_3) were deposited by electron beam physical vapor deposition (E-Flex, Polyteknik).

3.2.2 THEORETICAL MODEL

To study the process of strain waves generation and detection in bi-layered structures, we use a physical model described in Chapter 1. Since the pump illumination area is typically much larger than both the total thickness of a sample and generated strain wavelength, we neglect any diffraction effects and only consider a one-dimensional problem. In this case, assuming sound propagation along the z axis, thermodynamic equations Eqs. 1.3 become:

$$\begin{aligned} \gamma T_e \frac{\partial T_e}{\partial t} + \frac{\partial Q_e}{\partial z} &= -G(T_e - T_l) + S(z,t), \\ \tau_e \frac{\partial Q_e}{\partial t} + Q_e &= -k_{eq} \frac{T_e}{T_l} \frac{\partial T_e}{\partial z}, \\ C_l \frac{\partial T_l}{\partial t} &= G(T_e - T_l). \end{aligned} \tag{3.1}$$

Meanwhile, in one-dimensional case system of elastic equations Eqs. 1.19 can be written without tensor notations:

$$\begin{aligned} \sigma^{re} &= M\varepsilon, & \frac{\partial \varepsilon}{\partial t} &= \frac{\partial v}{\partial z}, \\ \sigma^{v} &= -\tau_l \frac{\partial \sigma^{v}}{\partial t} + \eta \frac{\partial \varepsilon}{\partial t}, & \rho \frac{\partial v}{\partial t} &= \frac{\partial}{\partial z}\left(\sigma^{re} + \sigma^{v} + \sigma^{th}\right). \\ \sigma^{th} &= -3K\alpha\Delta T_l, \end{aligned} \tag{3.2}$$

where the viscous parameters are: $\eta = \eta_2$ and $\tau_l = \eta_2/\eta_1$ (see Eqs. 1.19). Detection of strain waves is modeled by calculating the reflectivity of the sample with perturbated refractive index due to photoelastic and thermo-optic effects (see Section 1.1.3):

$$\Delta n = \frac{\partial n}{\partial \varepsilon}\varepsilon + \frac{\partial n}{\partial T} T_l. \tag{3.3}$$

Physical samples are fabricated by sequential deposition of poly(methyl methacrylate) (PMMA), metal, and transparent layers onto glass substrates (see Fig. 3.2). The measured time delay range is significantly smaller than the acoustic roundtrip time in the PMMA layer. Thus, the simulation domain excludes glass substrates, considering a three-layer structure with free surfaces. In dielectrics, the heat conductivity is determined by heat transfer via the lattice, which is much weaker than via free electrons in metals [118]. We, therefore, exclude heat transport effects in

Table 3.1: Aluminium parameter values used in simulations.

Parameter	Description	Value	Units	Source
TTM parameters				
γ	Electron volumetric heat capacity constant	91.2	$\mathrm{J/m^3K^2}$	[70]
G	Electron-phonon coupling coefficient	3.0×10^{17}	$\mathrm{W/m^3K}$	[70]
τ_e	Electron relaxation time	6.45	fs	calculated from Eq. 1.6
k_{eq}	Electron heat conductivity	235	$\mathrm{W/mK}$	[113]
C_l	Lattice volumetric heat capacity	2.4×10^6	$\mathrm{J/m^3K}$	[113]
Elastic parameters				
ρ	Mass density	2700	$\mathrm{kg/m^3}$	[113]
α	Thermal expansion coefficient	2.36×10^{-5}	$1/\mathrm{K}$	[113]
K	Bulk modulus	81.3	GPa	[113]
M	P-wave modulus	111.9	GPa	[113]
η	Viscous parameter	5×10^{-3}	Pa s	adjusted
τ_l	Elastic relaxation time	neglected	ps	–
Optical parameters				
n_{pump}	Complex refractive index at 1030 nm	$1.40 + i9.85$	–	[114]
n_{probe}	Complex refractive index at 780 nm	$2.65 + i8.46$	–	[114]
$\partial n / \partial \varepsilon$	Complex strain-optic coefficient at 780 nm	$-29.19 - i25.16$*	–	[16]
$\partial n / \partial T$	Complex thermo-optic coefficient at 780 nm	$(-1.18 + i1.62) \times 10^{-3}$*	$1/\mathrm{K}$	[16]

*The magnitude of strain-optic and thermo-optic coefficients is adjusted for better agreement with experiments keeping the ratio of real and imaginary parts.

Table 3.2: Gold parameter values used in simulations.

Parameter	Description	Value	Units	Source
		TTM parameters		
γ	Electron volumetric heat capacity constant	62.7	$\mathrm{J/m^3K^2}$	[70]
G	Electron-phonon coupling coefficient	2.45×10^{16}	$\mathrm{W/m^3K}$	[70]
τ_e	Electron relaxation time	26.3	fs	calculated from Eq. 1.6
k_{eq}	Electron heat conductivity	315	$\mathrm{W/mK}$	[113]
C_l	Lattice volumetric heat capacity	2.48×10^6	$\mathrm{J/m^3K}$	[113]
		Elastic parameters		
ρ	Mass density	19 280	$\mathrm{kg/m^3}$	[113]
α	Thermal expansion coefficient	1.42×10^{-5}	$\mathrm{1/K}$	[113]
K	Bulk modulus	180	GPa	[113]
M	P-wave modulus	217	GPa	[113]
η	Viscous parameter	2×10^{-2}	Pa s	adjusted
τ_l	Elastic relaxation time	neglected	ps	–
		Optical parameters		
n_{pump}	Complex refractive index at 1030 nm	$0.24 + i6.70$	–	[115]
n_{probe}	Complex refractive index at 390 nm	$1.47 + i1.94$	–	[115]
$\partial n/\partial \varepsilon$	Complex strain-optic coefficient at 390 nm	$-0.83 - i1.25$	–	adjusted
$\partial n/\partial T$	Complex thermo-optic coefficient at 390 nm	neglected	$\mathrm{1/K}$	–

Table 3.3: PMMA parameter values used in simulations.

Parameter	Description	Value	Units	Source
ρ	Mass density	1190×5	kg/m^3	[116]
M	P-wave modulus	$9/5$	GPa	[116]

Table 3.4: Al_2O_3 parameter values used in simulations.

Parameter	Description	Value	Units	Source
		Elastic parameters		
ρ	Mass density	3950	kg/m^3	[116]
K	Bulk modulus	165	GPa	[116]
M	P-wave modulus	150	GPa	[116]
η	Viscous parameter	neglected	Pa s	–
τ_l	Elastic relaxation time	neglected	ps	–
		Optical parameters		
n_{pump}	Complex refractive index at 1030 nm	$1.67 + i0.0$	–	[117]
n_{pr390}	Complex refractive index at 390 nm	$1.70 + i0.0$	–	[117]
n_{pr780}	Complex refractive index at 780 nm	$1.67 + i0.0$	–	[117]
$\partial n/\partial \varepsilon$	Complex strain-optic coefficient at 390 nm and 780 nm	$-0.4 - i0.0$	–	adjusted

the top dielectric and bottom PMMA layers. Also, since the dielectric layers are not absorptive for the pump wavelength used in our experiments, the strain generation is localized within the metal layer. Thus, temperature dynamics are only considered in a metal film with thermal-insulation boundary conditions $Q_e = 0$ applied to the dielectric-metal and metal-substrate interfaces, and initial conditions:

$$T_e(z,t=0) = T_l(z,t=0) = 300\mathrm{K}, \qquad Q_e(z,t=0) = 0. \tag{3.4}$$

Equations Eqs. 3.1 and 3.2 are solved numerically using FDTD method (see Section 1.2).

In this study, we consider two types of experimental samples containing aluminium and gold metal layers. Tables 3.1-3.4 contain material parameter values used in simulations. Some parameter values are taken from literature; others are either theoretically estimated or adjusted for better agreement with experiments. Table 3.3 contains only elastic parameter values for PMMA since thermal dynamics and optical penetration are neglected in this layer. Furthermore, mass density is artificially increased and P-wave modulus is reduced, both by factor 5. This results in 5 times lower speed of sound but does not affect acoustic impedance, keeping acoustic reflectivity at the metal-PMMA interface the same. Thus, the thickness of the PMMA layer can be reduced to save computational time. Table 3.4 contains parameter values for Al_2O_3 excluding TTM parameters since thermal effects in the oxide layer are neglected.

3.3 RESULTS AND DISCUSSION

3.3.1 PHOTOACOUSTIC SIGNALS IN ALUMINIUM FILMS

Figure 3.3a shows the reflectivity change due to laser-induced strain waves in a 170 nm thick aluminium film with Al_2O_3 top layer. The first echo reaches the front surface around 50 ps after the pump excitation, causing a dip in the reflectivity curves. This dip repeats approximately every 50 ps corresponding to the roundtrip time in this Al_2O_3 / aluminium structure. At zero pump-probe time delay, a peak is observed both in simulations (Fig. 3.3b) and experiments. The origin of this peak is the thermo-optic effect and thermal strain near the surface of the alumini um film.

The experimental curves show strong echo decay caused by sound attenuation in aluminium and strain wave coupling into the PMMA layer. The sound attenuation is frequency dependent and acts as a lowpass filter leading to signal smoothing and dispersive broadening. The coupling of strain waves into the PMMA layer is also significant. For speed of sound $v_{Al} = 6440\,\mathrm{m/s}$, $v_{PMMA} = 2750\,\mathrm{m/s}$ and density $\rho_{Al} = 2700\,\mathrm{kg/m^3}$, $\rho_{PMMA} = 1190\,\mathrm{kg/m^3}$ the acoustic impedance mismatch leads to 68 % reflectivity at the aluminium-PMMA interface. The thickness of the deposited PMMA layer is around 1 µm corresponding to a roundtrip time more than 700 ps. Hence, there are no strain waves coupled back into aluminium from the PMMA layer within the measured pump-probe delay range.

The echo amplitude increases and the shape of the reflectivity curves changes with the thickness of Al_2O_3. Strain waves generated at the surface of the aluminium also propagate into the Al_2O_3 layer. After a round trip in Al_2O_3 the strain wave partially enters the aluminium film causing an additional peak around 10–20 ps time delay. For thicker Al_2O_3 layers the roundtrip time is longer, resulting in an increased time delay of this peak.

The echoes from the aluminium layer are found to increase in signal strength for thicker Al_2O_3 layers. This enhancement is caused by free surface elimination [108] and the optical effects mentioned in Section 3.1. To understand the free surface effect, consider a strain pulse generated in an aluminium film (Fig. 3.4a). After the pump absorption, two negative counter-propagating unipolar strain pulses are generated. One of them propagates into the sample while another one immediately reflects from the free surface and undergoes a sign flip [8, 11]. This results in a bipolar pulse with a negative part followed by a positive strain. If thermal diffusion and dispersion effects are excluded, the strain pulse has the shape of two mirrored truncated exponential functions with an infinite gradient in the point of symmetry. Thermal diffusion and strain wave dispersion lead to pulse broadening and smoothing, which results

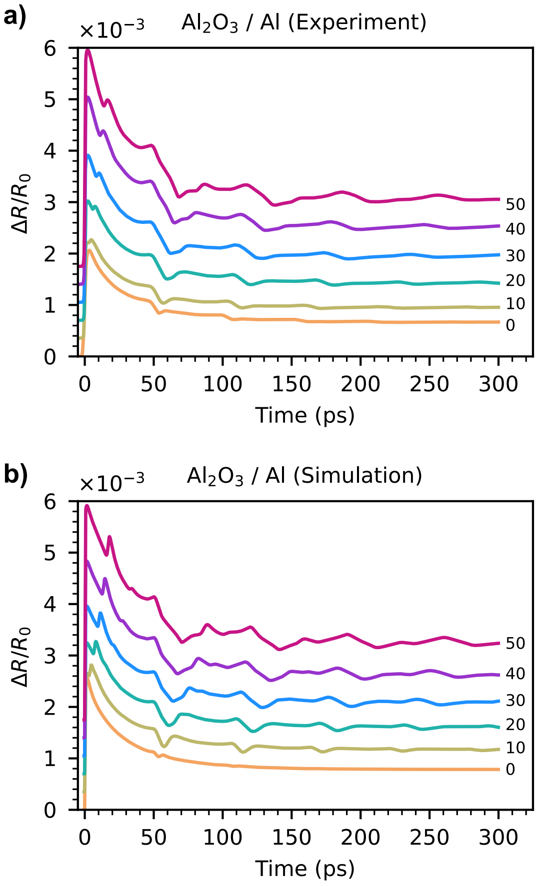

Figure 3.3: Measured a) and simulated b) reflectivity change in Al_2O_3 / aluminium samples. Pump pulse energy 1 nJ. Probe wavelength 780 nm. Aluminium thickness 170 nm. Al_2O_3 thickness is shown on the graph in nm. A vertical offset between the different traces is applied for clarity.

in a sine-like shape of the strain pulse. Upon the reflection from a free surface or any interface with lower acoustic impedance material, the pulse undergoes a sign flip. Thus, the strain distribution near the free surface is effectively a sum of two mirrored counter-propagating pulses with opposite phases. Because the strain pulse generated in aluminium has a bipolar shape, the strongest strain field in the vicinity of the surface occurs when the leading half of the pulse is fully reflected. At this moment the reflected part constructively interferes with the following rear half of the pulse. This can be observed in the top subplot of Fig. 3.4b at 54 ps. However, due to the non-instantaneous transition between negative and positive parts of a strain pulse, the point of maximum strain does not reach the surface. Furthermore, strain at the surface is fixed to its thermal value [108]. That is why all the curves in the top subplot of Fig. 3.4b have almost the same value at the edges. The small deviations are caused by thermal decay in aluminium. As optical detection of the strain wave happens in a thin layer defined by the probe penetration depth (indicated by the green area in Fig. 3.4b), this situation results in a small detectable reflectivity change (Fig. 3.4c, blue). In contrast, the presence of a transparent layer allows the strain pulse to pass through the interface, into the Al_2O_3 layer. That effectively shifts the detection region deeper into the sample and enhances detection sensitivity (Fig. 3.4c) [108].

The signal enhancement due to this free boundary elimination effect increases with top layer thickness, but saturates when the thickness reaches around half the strain pulse extent. In our case this happens at 20–30 nm thickness of Al_2O_3, as shown by simulations (Fig. 3.5a). However, the experiments clearly show that the signal enhancement continues beyond this saturation thickness, which points to the existence of additional effects. By including the influence of optical effects caused by the presence of strain in the Al_2O_3 layer, this continued enhancement can be explained, and good agreement between simulation and experiment can be obtained (Fig. 3.5). Three main optical effects are identified, namely the strain-optic effect in the Al_2O_3 that changes its refractive index, the physical thickness variation of the Al_2O_3 layer induced by the strain, and the coating effect of the Al_2O_3 layer. The last effect means that for a given strain-induced refractive index change in aluminium, the samples with different thicknesses of Al_2O_3 show different $\Delta R_0/R$ signal.

To better understand the contribution of these optical effects to the reflectivity curve, it is sufficient to decompose the total signal into individual components. Figure 3.6 shows the reflectivity change caused by the thickness change of Al_2O_3 (red curve), by strain-induced refractive index variation of Al_2O_3 (green curve) and by strain-induced refractive index variation of aluminium (orange curve). A linear decomposition of the total signal into these three components is justified as the effects can be treated as a small perturbation of the reflectivity. The roundtrip times in the Al and Al_2O_3 layers are indicated by vertical lines. The green and red curves

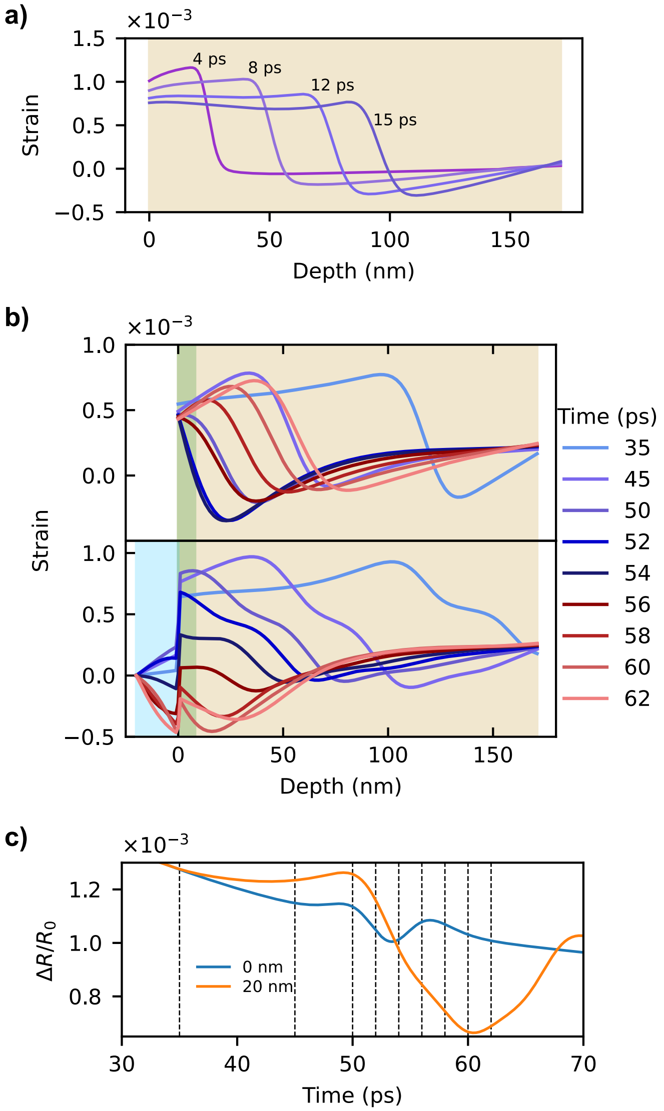

Figure 3.4: Simulation of light-induced strain waves in the Al_2O_3 / aluminium structure. Beige filling depicts aluminium, blue – Al_2O_3, green – penetration depth of 780 nm probe light into aluminium. Penetration depth is defined as $\lambda/4\pi\kappa$, where κ is the imaginary part of the refractive index $n = 2.65 + 8.45i$. a) Strain wave evolution at increasing time delays after pump excitation from the left in a 170 nm thick aluminium film. b) The strain wave shape at different time delays, around the expected return time at the front surface. Top subplot is a bare aluminium film, bottom – with 20 nm of Al_2O_3. Because of the different elastic constants of aluminium and Al_2O_3, the strain experiences a discontinuity at the interface between the materials. c) Reflectivity change around the first echo for bare aluminium (blue) and in the presence of a 20 nm Al_2O_3 layer (orange). The vertical dashed lines correspond to the time labels in b).

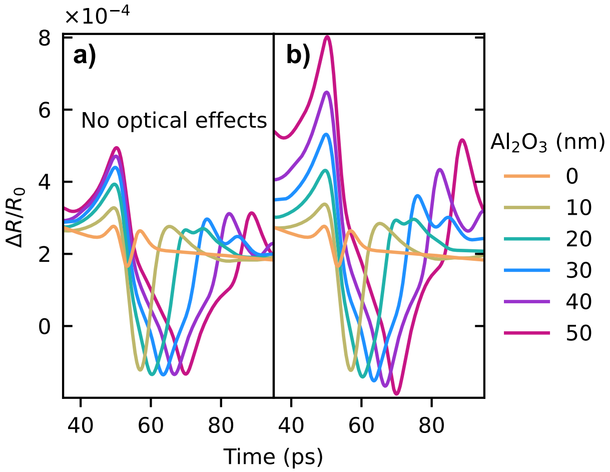

Figure 3.5: Simulation of the first echo in the freestanding aluminium film excluding a) and including b) optical effects for different Al_2O_3 thicknesses. Thermo-optic effects are excluded both in a) and b) for clarity. Optical effects are excluded by setting the refractive index of Al_2O_3 for both pump and probe to 1, and strain-optic coefficient of Al_2O_3 to 0.

correspond to strain dynamics in Al_2O_3 and the orange curve to strain dynamics in aluminium. After the pump is absorbed by the aluminium film, two unipolar compressive strain pulses are generated. One pulse propagates into the aluminium and the other into Al_2O_3. The strain pulse in the Al_2O_3 rapidly reflects within the layer, changing its polarity upon each reflection from the air / Al_2O_3 interface. The polarity change can be observed in the red and green curves as a decaying oscillation with the period of the Al_2O_3 roundtrip time. Upon each full round trip in the Al_2O_3 layer the strain pulse partially couples into the aluminium, giving rise to spikes in the orange curve in Fig. 3.6. After 2-3 round trips in Al_2O_3, the strain energy is almost fully transferred to the aluminium. Around 50 ps the strain pulse that was originally propagating in the aluminium film reaches the Al_2O_3 / aluminium interface, which can be observed as a spike in the orange curve. After a roundtrip in Al_2O_3 this pulse constructively interferes with the following strain pulse that was propagating in Al_2O_3. That interference results in a dip around 70 ps.

From Fig. 3.6 one can see that the total signal is mostly determined by the strain-induced refractive index modulation in aluminium. This is because aluminium has relatively strong strain-optic coupling. For aluminium we use the value $\partial n/\partial \varepsilon = -29.19 - 25.15i$ which has the same phase as in [16]. The amplitude of $\partial n/\partial \varepsilon$ was adjusted for a better fit with experimental results. For Al_2O_3 we use $\partial n/\partial \varepsilon = -0.4$ which agrees well with our experimental results. From this analysis, the influence of the thickness change and strain-optic coupling in Al_2O_3 is found to be weak, and the coating effect of the Al_2O_3 layer is identified as the main reason for the

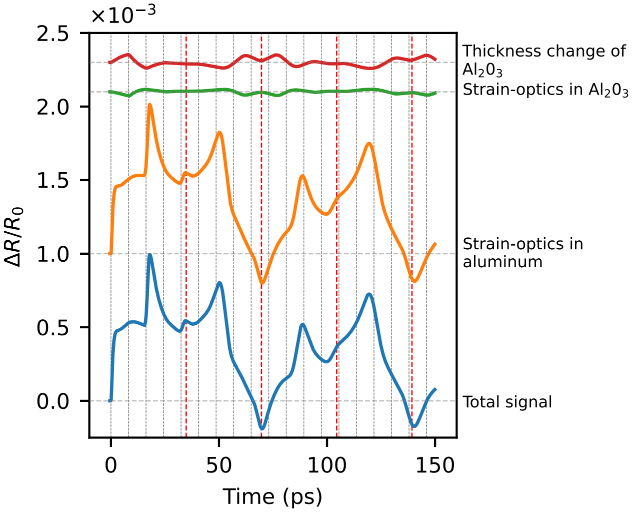

Figure 3.6: Separated optical effects in aluminium with 50 nm thick Al_2O_3 layer. Vertical black and red lines represent half of the roundtrip time in Al_2O_3 and in the whole sample respectively. Horizontal lines indicate the vertical offset applied for clarity.

optical enhancement of the strain detection. Furthermore, as the thickness change of Al_2O_3 and strain-optic effects in Al_2O_3 counteract each other, the coating effect becomes even more apparent. Such a destructive interference effect is the result of a negative strain-optic coefficient in most materials. While the positive strain expands the Al_2O_3 layer, the average refractive index of the layer is decreased due to the negative strain-optic coefficient. As a result, the contribution of these two effects on the phase accumulation within the Al_2O_3 layer is partially canceled.

3.3.2 PHOTOACOUSTIC SIGNALS IN GOLD FILMS

Photoacoustic signals as observed in Al_2O_3 / gold bi-layers are shown in Fig. 3.7. In these structures, a similar signal enhancement for increasing Al_2O_3 layer thickness is observed, but it is accompanied by much more dramatic changes in the shape of the signals as compared to the Al_2O_3 / aluminium bi-layers.

To begin with, the reflectivity change curve shape for thin layers of Al_2O_3 requires some explanation since it strongly differs from the aluminium case. Gold has much lower electron-phonon coupling and higher electron heat conductivity compared to aluminium (see Tables 3.1 and 3.2). Those differences lead to a broadening of the pump-heated region. Specifically in our case, the gold layer becomes almost homogeneously heated, with expansion starting from both edges. Two expansion fronts then move towards the center of the layer at the speed of sound, forming two step-like strain pulses. The first detected strain pulse at 50 ps is the one that is generated on the back surface of the sample. Because it does not undergo a sign-flip due to reflection, it has an opposite polarity compared to the first echo pulse at 100 ps. Thus, the reflectivity curves for 0–30 nm thick Al_2O_3 (Fig. 3.7) contain two sequences of signals that are staggered in time, one being positive and the other negative. The echo decay is weaker than in the case of Al_2O_3 / aluminium samples due to higher acoustic impedance mismatch between gold and PMMA. For $v_{Au} = 3350\,\mathrm{m/s}$ and $\rho_{Au} = 19\,280\,\mathrm{kg/m^3}$ the reflectivity at the gold-PMMA interface is 90 %. The gold viscosity parameter η is adjusted to a value $2 \times 10^{-2}\,\mathrm{Pa\,s}$.

To understand the significant signal shape change that happens for layer thicknesses upward of 40 nm of Al_2O_3 (Fig. 3.7), we do a signal decomposition (Fig. 3.8)

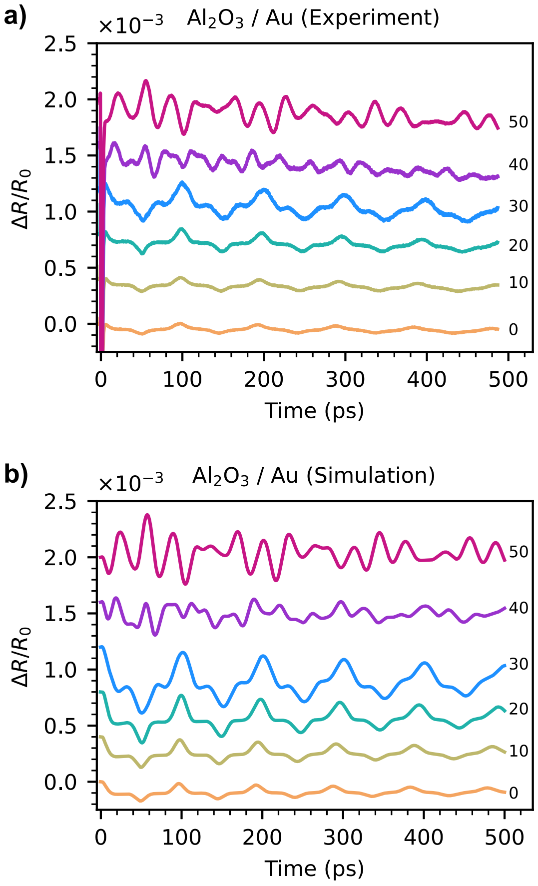

Figure 3.7: Measured a) and simulated b) reflectivity change in Al_2O_3 / gold samples. Pump pulse energy 2 nJ. Probe wavelength 390 nm. Gold thickness 160 nm. Al_2O_3 thickness is shown on the graph. A vertical offset between the different traces is applied for clarity.

similar to the Al_2O_3 / aluminium case (Fig. 3.6).

The effect of a thickness change of Al_2O_3 (Fig. 3.8, red trace) has the same behavior as in the Al_2O_3 / aluminium stack (Fig. 3.6). However, a sign flip of the curve is observed at 40 nm of Al_2O_3. The reason for this sign flip is visualized in Fig. 3.9, which shows the reflectivity of the Al_2O_3 / gold stack as a function of Al_2O_3 thickness. Around 35 nm the reflectivity curve has a local minimum that corresponds to the point where the derivative crosses zero, thus changing the sign of the reflectivity change due to layer thickness variation. The reflectivity change is determined both by the slope of the reflectivity curve and by the total deformation, i.e. the integral of strain. While the thickness of the Al_2O_3 layer does not affect the amplitude of the strain pulse, it does influence the deformation of the layer. As long as the Al_2O_3 layer thickness is smaller than the strain pulse length, the total deformation (namely Δh in Fig. 3.9) increases with Al_2O_3 thickness, causing

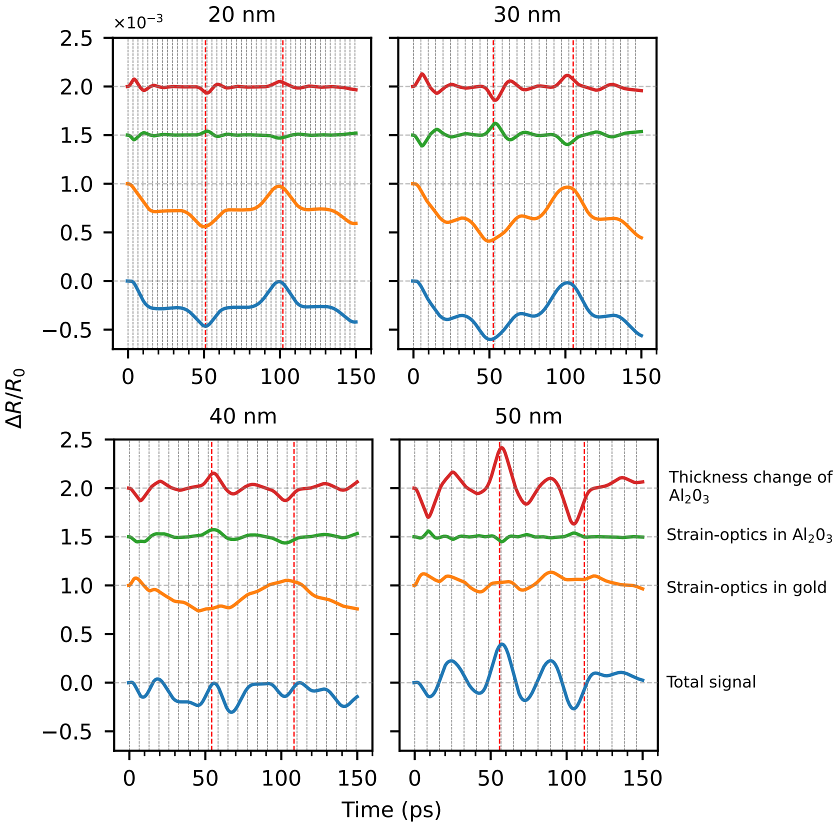

Figure 3.8: Separated optical effects in gold with different thickness of Al_2O_3 layer. Vertical black and red lines represent half of the roundtrip time in Al_2O_3 and in the whole sample respectively. Horizontal lines indicate the vertical offset applied for clarity.

a higher reflectivity change even if the slope is the same. Furthermore, the echo signals are defined by the $\Delta R/R_0$ value (Fig. 3.7) which depends on the nominal reflectivity R_0 and therefore also on the Al_2O_3 thickness. Thus, the $\frac{\Delta R/R_0}{\varepsilon}$ value (Fig. 3.9 dash-dotted grey) gives the best intuition for the amplitude of the signals induced by thickness change of Al_2O_3.

For an Al_2O_3 layer thickness up to 40 nm, the strain-optic effect in Al_2O_3 (Fig. 3.8, green) behaves as discussed in Section 3.3.1, showing an opposite effect on ΔR as the thickness changes. At layer thicknesses of 40 nm and higher, this relation changes. At this point, the Al_2O_3 thickness becomes comparable to the probe wavelength. Thus, the non-homogeneous distribution of the strain-induced refractive index change in Al_2O_3 can not be approximated by an effective average change of refractive index of the Al_2O_3 layer.

A similar evolution happens with the part of the signal that corresponds to the strain-optic coupling in gold (Fig. 3.8 orange). Although, here it is due to the complexity of the refractive index profile within the penetration depth of the probe light in gold. Multiple strain pulses that evolve in the sample due to partial reflections at the Al_2O_3 / gold interface effectively create a dynamic multi-layered stack.

From Fig. 3.8 one can see that the strain dynamics in gold is the main contribution to the total signal for the 20 nm and 30 nm thick Al_2O_3, while for the 40 nm and 50 nm the total signal is mostly determined by the strain dynamics in Al_2O_3. This change in the dominant mechanism responsible for a ΔR variation explains the significant reflectivity curve shape change that is observed for thicker layers of Al_2O_3 in Fig. 3.7. The more prominent effect of the strain dynamics in Al_2O_3 for Al_2O_3 / gold bi-layers compared to Al_2O_3 / aluminium ones in the same range of

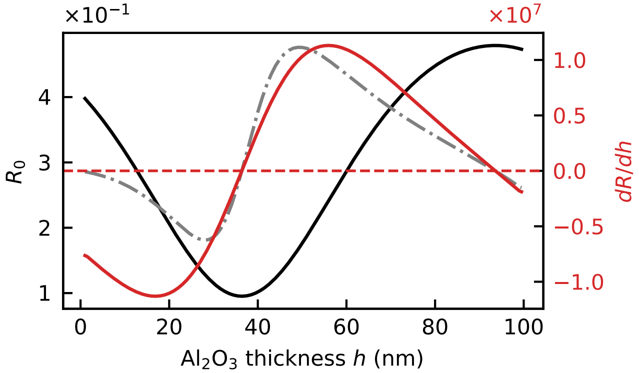

Figure 3.9: Calculated reflectivity of the Al_2O_3 / gold stack (black solid curve) as a function of Al_2O_3 thickness. The red solid curve is a thickness derivative of the reflectivity. The grey dash-doted curve shows the arbitrarily y-scaled $\frac{\Delta R/R_0}{\varepsilon}$ value ($\frac{dR}{dh} \approx \frac{\Delta R}{h\varepsilon} \rightarrow \frac{\Delta R}{h\varepsilon} \cdot \frac{h}{R_0} = \frac{\Delta R/R_0}{\varepsilon}$).

Al_2O_3 thickness is due to a shorter probe wavelength (390 nm vs 780 nm) and lower strain-optic coefficient of gold ($-0.83 - 1.25j$ vs $-29.19 - 25.15i$).

3.4 CONCLUSION

The effect of transparent nanolayers on the optical detection of light-induced strain waves has been systematically studied. We showed that, in addition to signal enhancements caused by free boundary effects [108], the presence of a transparent layer introduces several additional optical phenomena that influence the detection sensitivity. These optical effects were classified into three types: the coating effect of the transparent layer, the strain-optic effect in the transparent layer, and a physical thickness variation of the transparent layer induced by the strain. It was shown that the relative contribution of each type of these optical effects to the total $\Delta R/R_0$ signal depends on the thickness of the transparent layer. Through the interplay of these different effects, the time-dependent variation in $\Delta R/R_0$ can display complex structure compared to a bare metal film. Although it is impossible to observe experimentally all three optical effects separately, theoretical calculations of the total $\Delta R/R_0$ show good agreement with experimental results.

4

CHARACTERIZATION OF SUB-OPTICAL-WAVELENGTH STRUCTURES THROUGH OPTICALLY OPAQUE FILMS USING PICOSECOND ULTRASONICS

INTRODUCTION

Periodic arrays of nanostructures form an important building block of modern integrated circuits and photonic devices. Functionality of such devices is often critically dependent on detailed structure. Moreover, multi-step lithographic processing requires accurate metrology tools to characterize device morphology non-invasively, often after the deposition of additional layers of material. In this chapter we show that ultrafast picosecond ultrasonics enables accurate characterization of periodic structures below optically opaque thin films. By optically generating and detecting ultrahigh-frequency ultrasound at the surface of the film, we quantitatively characterize the main features of subsurface gratings with linewidths down to 100 nm. We find that the acoustic diffraction is sensitive to the shape of the grating lines at the scale of tens of nanometers.

This chapter has been published in Nano Lett. 25, 8909-8914 (2025) [119]

4.1 ULTRAFAST PHOTOACOUSTICS FOR METROLOGY APPLICATIONS

Lithographic fabrication of nanostructures is the core technology driving integrated circuit (IC) manufacturing. The miniaturization of electronics and development of increasingly powerful computing systems is made possible by continuous improvements in IC technology. Modern IC designs feature complex three-dimensional nanostructures, which require extremely precise lithography. Reliable manufacturing is therefore critically dependent on sub-nanometer-level positioning accuracy, as well as measurement methods to quantitatively characterize fabricated nanostructures [58, 120]. This field of semiconductor metrology involves characterization of the fabricated nanostructures in between lithography steps and on the completed devices, but also covers methods that ensure accurate positioning of the silicon wafers before printing, and position verification of the printed features relative to previously printed layers. Such methods are known as wafer alignment and overlay metrology, and are typically performed on dedicated markers printed near the actual devices [58]. These markers are typically periodic structures such as diffraction gratings, as they have a distinct and efficient optical response. In semiconductor metrology, optical methods are preferred because they are fast and non-invasive. However, as structures become much smaller than an optical wavelength, and IC designs increasingly contain materials that are optically opaque, such optical methods are reaching their limits in terms of resolution and contrast. While alignment and overlay metrology can in principle be performed on larger structures that are optically detectable, their accuracy improves for smaller feature sizes. Importantly, as metrology markers are typically printed in the first lithography step, they may become covered by large amounts of material during fabrication of complex multilayer devices such as 3D-NAND memory. To realize the ambitious scaling of IC device size and complexity pursued by the semiconductor industry, the development of new metrology concepts that are effective for optically opaque 3D nanostructures becomes crucial [120].

In this chapter, we demonstrate the potential of ultrafast-laser-driven photoacoustics, also known as picosecond ultrasonics, for metrology on sub-optical-wavelength markers, through layers of optically opaque material. When a femtosecond laser pulse strikes a partially absorbing surface, the interaction with electrons and subsequent electron-phonon coupling results in the generation of coherent acoustic phonons with extremely high frequencies, approaching the THz range [7, 62, 84, 121–123]. These coherent acoustic phonons form a localized wavepacket that travels into the material at the speed of sound. Upon propagation, internal interfaces and structures give rise to reflection and diffraction [14, 26, 121]. As such high-frequency wavepackets can contain wavelength components well below 100 nm, efficient diffraction from structures in the 10-100 nm range can occur.

When the diffracted wavepackets return to the surface, they can be characterized optically through their influence on the surface reflectivity, using a time-delayed probe laser pulse [36, 62, 123].

Picosecond ultrasonics has been used to study thin-film layer properties [8, 14–16, 124], detection of buried structures [21, 24], and as a contrast mechanism for microscopy [23, 25, 27, 28]. We now show that the technology can be extended to characterize far-sub-optical-wavelength structures, by analyzing the temporal structure of the diffracted wavepackets that return to the surface.

We perform a series of experiments in which we generate and detect such acoustic pulses inside layers of zirconium with different periodic nanostructures patterned on the back surface. We detect the reflected and diffracted ultrasound wavepackets, and retrieve the properties of the nanostructures from these signals. By comparing the experimental observations to simulation results, we can retrieve structural parameters and nanoscale shape variations of the markers.

The concept of picosecond ultrasonics on nanoscale buried periodic markers is shown in Figure 4.1. The sample is a uniform layer of opaque material with etched grating on the back surface. The thickness of the layer and the pitch of the grating are on the order of several hundreds of nanometers. For clarity, we will refer to the etched and unprocessed areas of the grating as lines and valleys, respectively. Pump and probe pulses from two separate but electronically synchronized lasers are focused into micron-sized spots onto the flat top surface of the sample (Figure 4.1a). The relative time delay between pump and probe pulses is scanned electronically, and probe reflectivity is detected with shot-noise-limited sensitivity through balanced detection and lock-in amplification [93]. Details of the experimental setup are given in the Section 2.2.2.

Measuring probe reflectivity within a certain pump-probe time-delay range gives a specific reflectivity change pattern determined by the buried grating (Figure 4.1b). Two-dimensional finite-difference time-domain (FDTD) simulations of the generated and propagating strain profiles [35] are shown in Figure 4.1c for different times after excitation by the pump pulse. For details on numerical simulation approach see Section 4.2.2.

As illustrated in Figure 4.1c, the pump pulse initially induces a planar longitudinal strain pulse that propagates towards the buried grating. Upon reflection from the grating, two time-separated groups of strain pulses are formed by the reflection from the lines and valleys (marked by 1 and 2). In addition, diffraction from the line edges leads to curved wavefronts around those edges. Reflection from the top surface leads to a second roundtrip of the strain pulses, which is largely a copy of the first roundtrip, with one important difference: the diffracted part of the acoustic strain wave from the line now couples into the space, and vice versa. The expected normalized reflectivity change $\Delta R/R_0$ at the surface is plotted in Figure 4.1b. Five distinct peaks can be identified, which correspond to the different strain wave components from lines and valleys returning to the surface, as numbered in Figure 4.1c. Whereas peaks 1,3 and 2,5 correspond to the first and second roundtrips on lines and valleys, peak 4 results from the line edge diffraction described above. This "diffraction echo" is specifically sensitive to the shape of the grating lines, as will be

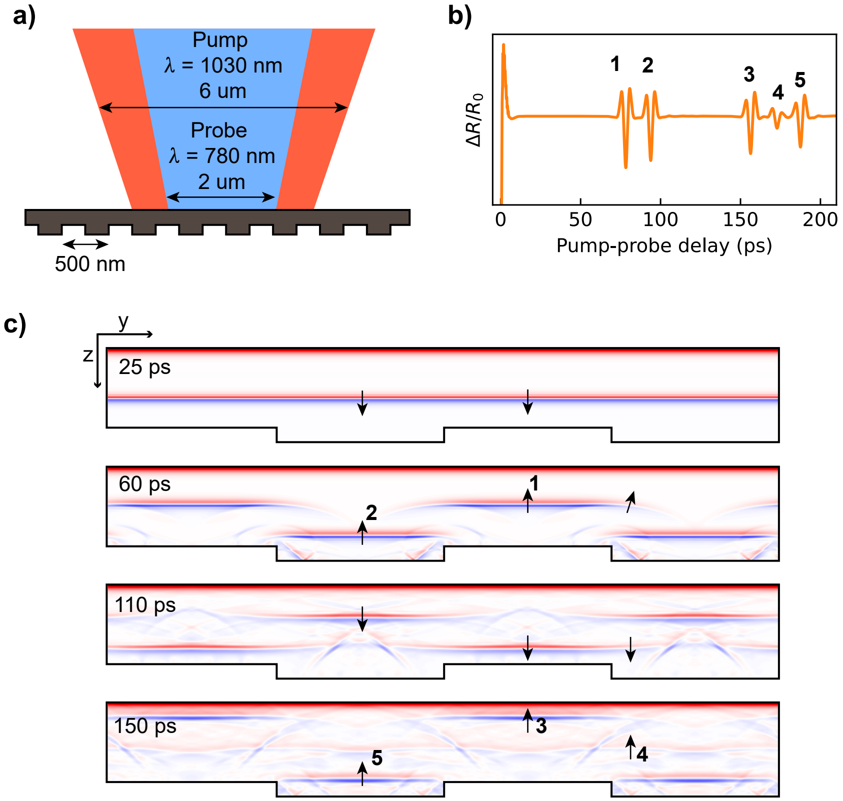

Figure 4.1: Concept of photoacoustics on nanoscale buried gratings. a) Cross-section sketch of the interaction with pump and probe beams. b) Simulated reflectivity change vs time. c) Four consecutive snapshots of the simulation of light-induced strain waves in the structure. The longitudinal strain component ε_{zz} is displayed, with red and blue colors indicating positive and negative strain, respectively. Black arrows indicate the direction of wave propagation. At 25 ps, a planar strain pulse is traveling towards the back surface of the sample. At 60 ps, two groups of strain pulses are seen returning to the surface, resulting from the splitting of the initial planar pulse by the first reflection from grating lines and valleys. Numbered arrows correspond to the peaks in the reflectivity change. One can also see the lateral diffraction of the strain pulse indicated by a tilted arrow. At 110 ps, the first group of pulses reaches the grating line again. Due to lateral broadening, part of the strain pulses couples into the valleys. In the same way, the second group of pulses partially reflects from the lines. As a result, after the second reflection from the grating (150 ps) there is an additional strain pulse labeled by arrow 4. The constant strain at the top surface of the sample is caused by thermal expansion of the sample.

shown below.

The time dependence of $\Delta R/R_0$ can thus be used to retrieve structural properties. As the roundtrip time delay encodes layer thickness [8, 14, 15] and local thickness variation [23], the time delay between peaks 1 and 2 encodes grating line height. If the wavelength of the strain wave is much shorter than the grating linewidth, the ratio of signals 1 and 2 can directly be interpreted as the duty cycle of the grating, i.e. the relative width of lines and valleys. However, as the finite acoustic wavelength leads to diffraction, this also affects the reflected wave from lines and valleys in a different way. As can already be seen at $t = 60\,\text{ps}$ in Figure 4.1c, edge diffraction in the valley leads to part of the strain pulse being strongly diffracted, which results in a reduction of the signal returning from the valley relative to the line, such that this second peak will be weaker than the first for a grating with 50 % duty cycle. Through this mechanism, the detected signal is sensitive to the pitch of the grating. In addition, grating pitch determines the relative amount of coupling of strain waves between lines and spaces. This effect makes the amplitude of the diffraction peak dependent on grating pitch.

Given this sensitivity to grating parameters, a logical question is whether quantitative retrieval of those parameters from the measured time-dependent $\Delta R/R_0$ signals is possible. A complicating factor for such quantitative retrieval is that in addition to the grating parameters, the resulting $\Delta R/R_0$ signal is strongly influenced by the elastic, optical, and thermodynamic properties of the material. These properties determine the process of strain pulse generation and propagation, as well as the sample's optical response to a given strain distribution near the top surface. However, if these material properties are known, numerical simulations of the photoacoustic interactions [35, 107] can quantitatively predict the time-dependence of $\Delta R/R_0$ in the presence of a grating structure. Such models can then be used to solve the inverse problem of retrieving the structural properties of the buried features. The accuracy of such a procedure naturally depends on the completeness of the model and the quality of the data, but especially on the sensitivity to the nanoscale structural properties. To address these aspects, we performed systematic experiments and simulations on a range of different nanostructures.

4.2 RESEARCH METHODS

4.2.1 EXPERIMENTAL SAMPLES

For the experiments, a series of 10×10 µm gratings with various pitches and duty cycles were milled in the 400 nm thick zirconium freestanding membrane with the use of a gallium focused ion beam (FEI Helios NanoLab 600). A typical photoacoustic response is shown in Figure 4.2a. For reference, a measurement at an unstructured part of the Zr membrane is shown as the blue trace, showing two clear echo signals that correspond to consecutive roundtrips of the acoustic wavepacket. The orange trace is the result of a measurement at the location of a grating with 600 nm pitch and 50 % duty cycle. The measurement clearly shows the expected five peaks as discussed above. A scanning electron microscope (SEM) image of the grating, recorded from the patterned side, is shown in Figure 4.2b.

4.2.2 NUMERICAL SIMULATIONS

In the chosen geometry where the optical spots are significantly larger than the grating period and the probe spot is smaller than the pump (see Figure 4.1a for typical numbers), we can consider homogeneous acoustic excitation and detection across the probe spot. Such a geometry allows the simulation of a single grating period with homogeneous pump excitation and periodic lateral boundary conditions. The theoretical model and numerical simulation approach are explained in detail in Chapter 1.

In order to perform simulations, we need to know material properties. To retrieve unknown photoacoustic properties of zirconium, we first fit the measurements taken on the unprocessed membrane to our numerical model (see Chapter 1) with the use of a non-linear least squares algorithm (Fig. 4.3). The retrieved material parameters are then used to simulate the expected measurement response in the presence of the grating structures. These parameters are the refractive index at probe wavelength, the photoelastic constants, the viscous coefficients, and the elastic relaxation time (see Table 4.1). Other parameters are either taken from the literature or theoretically

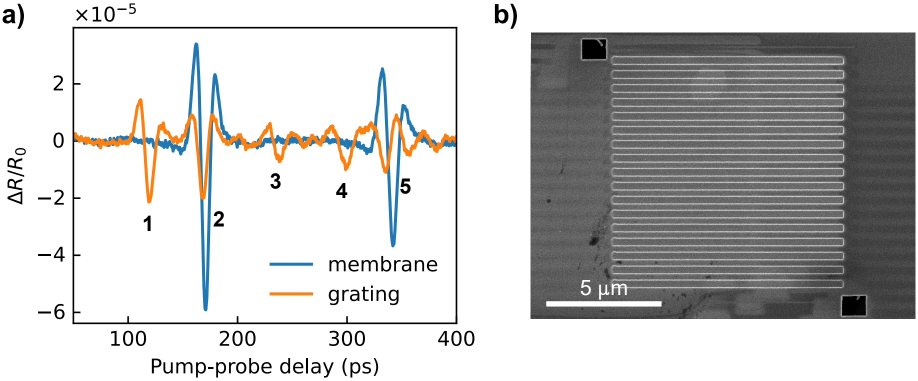

Figure 4.2: a) Experimentally observed time-dependent reflectivity variation for a flat 400 nm thick freestanding membrane of Zr and the film with imprinted 600 nm pitch and 50 % duty cycle grating. Initially, measurements contain a significant thermal background that is caused by nanosecond-scaled temperature dynamics in the sample. This thermal background is removed by 15 GHz high-pass filtering (for more details see Section 4.2.2). Five peaks are visible in the signal from the grating, which correspond to the expectation from simulations. b) SEM image of a 600 nm pitch grating milled into a Zr film.

Table 4.1: Best-fit parameter values on 400 nm thick flat Zr membrane

Parameter	Explanation	Value	Units
n_{probe}	Complex refractive index at 780 nm	$4.47 + i3.26$	–
P_{12}	Complex photoelastic constant	$-0.021 + i0.128$	–
η_2	Viscous parameter	1.14×10^{-2}	Pa s
τ_l	Elastic relaxation time	2.46	ps

estimated (see Table 4.2).

Since the focus spots of the pump and probe are much bigger than the thickness of the membrane, we consider a one-dimensional problem for the fitting procedure. In this case, we can fit only two (η_1 and η_2) out of four (η_1, η_2, ζ_1, and ζ_2) viscous parameters (see Eqs 1.19). For further two-dimensional simulations of the patterned membrane, we assume $\eta_2 = \chi$, i.e., $\xi = 0$ and $\tau_v = \tau_s = \tau_l$.

Table 4.2: Zirconium parameter values used in simulations

Parameter	Explanation	Value	Units	Source
γ	Electron volumetric heat capacity constant	89.5	J/m^3K^2	calculated from Eq. 1.4
G	Electron-phonon coupling coefficient	7.74×10^{18}	W/m^3K	calculated from Eq. 1.7
τ_e	Electron relaxation time	0.65	fs	calculated from Eq. 1.6
k_{eq}	Electron heat conductivity	22.6	W/mK	[113]
C_l	Lattice volumetric heat capacity	1.8×10^6	J/m^3K	[125]
ρ	Mass density	6505	kg/m^3	[125]
α	Thermal expansion coefficient	5.69×10^{-6}	1/K	[125]
K	Bulk modulus	91.7	GPa	[125]
μ	Shear modulus	32.8	GPa	[125]
n_{pump}	Complex refractive index at 1030 nm	$4.16 + i3.84$	–	[126]

A one-dimensional fitting also retrieves only one (P_{12}) out of two photoelastic constants (see Eq. 1.34). However, for two-dimensional simulations of samples with periodic structuring, knowledge of P_{11} photoelastic constant is not necessary. Let us consider the y axis oriented along the grating vector and the z axis oriented along laser/acoustics propagation. The strain tensor then contains only ε_{yy}, ε_{zz}, and ε_{yz} components and the tensor of strain-induced change of dielectric permittivity (Eq. 1.34) becomes:

$$\Delta\hat{\epsilon} = -\epsilon_0^2 \begin{pmatrix} P_{12}(\varepsilon_{yy}+\varepsilon_{zz}) & 0 & 0 \\ 0 & P_{11}\varepsilon_{yy}+P_{12}\varepsilon_{zz} & P_{44}\varepsilon_{yz} \\ 0 & P_{44}\varepsilon_{yz} & P_{12}\varepsilon_{yy}+P_{11}\varepsilon_{zz} \end{pmatrix}. \tag{4.1}$$

A perturbed dielectric tensor is then $\hat{\epsilon} = \epsilon_0\hat{I} + \Delta\hat{\epsilon}$, where $\hat{I}$ is the identity matrix. Phase velocity (refractive index) and polarization of optical waves in solids for a given propagation direction can be found by solving eigenvalues/eigenvector problem [127]:

$$\hat{\beta}\boldsymbol{D} - \boldsymbol{s}\left(\boldsymbol{s}\cdot\hat{\beta}\boldsymbol{D}\right) = \frac{1}{n^2}\boldsymbol{D}, \tag{4.2}$$

where $\boldsymbol{s}$ is the normalized wavevector, $\boldsymbol{D} = \hat{\epsilon}\boldsymbol{E}$ is the electric displacement vector, and $\hat{\beta} = \hat{\epsilon}^{-1}$ is the tensor of dielectric non-permittivity. In case of propagation along the z axis, $\boldsymbol{s} = (0,0,1)$ and $\boldsymbol{D} = (D_x, D_y, 0)$. Then, Eq. 4.2 gives two pairs of eigenvalues and eigenvectors:

$$n_1^2 = 1/\beta_{xx}, \qquad \boldsymbol{D}_1 = (1,0,0); \tag{4.3}$$

$$n_2^2 = 1/\beta_{yy}, \qquad \boldsymbol{D}_2 = (0,1,0). \tag{4.4}$$

We can see that two eigen polarizations are coaligned with x and y axes. By substituting Eq. 4.1 into Eq. 4.3 we get the refractive index for x-polarized light:

$$n_x^2 = \epsilon_0 + \Delta\epsilon_{xx}. \tag{4.5}$$

Small variations of refractive index can then be defined as

$$\Delta n_x \approx \frac{\Delta\epsilon_{xx}}{2n_0} = -\frac{n_0^3 P_{12}}{2}\varepsilon_{yy} - \frac{n_0^3 P_{12}}{2}\varepsilon_{zz}, \tag{4.6}$$

where $n_0^2 = \epsilon_0$. In the same way by substituting Eq. 4.1 into Eq. 4.4 we can derive the change of refractive index for y-polarized light:

$$\Delta n_y \approx \frac{1}{2n_0}\left[\Delta\epsilon_{yy} - \frac{\Delta\epsilon_{yz}^2}{\epsilon_0 + \Delta\epsilon_{zz}}\right]. \tag{4.7}$$

One can notice that $\Delta\epsilon_{yz}$ component has the second-order effect on the change of refractive index and thus can be neglected:

$$\Delta n_y \approx \frac{\Delta\epsilon_{yy}}{2n_0} = -\frac{n_0^3 P_{11}}{2}\varepsilon_{yy} - \frac{n_0^3 P_{12}}{2}\varepsilon_{zz}. \tag{4.8}$$

Equations 4.6 and 4.8 define refractive index changes for two orthogonal polarizations of the probe light. However, since we consider periodic structures and simulate one grating period with periodic lateral boundary conditions, a certain symmetry of the strain profile along the y axis is implied. In particular, the integral of both components ε_{yy} and ε_{yz} within a period of the grating along the y axis is zero. This means that ε_{yy} strain component does not contribute to reflectivity change and can be excluded from Eqs. 4.6 and 4.8. The change of refractive index can then be considered polarization-independent and calculated similarly to a one-dimensional case:

$$\Delta n = -\frac{n_0^3 P_{12}}{2}\varepsilon_{zz}. \tag{4.9}$$

Figure 4.3a shows the raw experimental data for a flat Zr membrane with a thickness of 400 nm that was used in the fitting procedure. Significant reflectivity drop at time delay $t = 0$ is caused by the high temperature of the electron subsystem, which undergoes instant heating upon pump pulse absorption. Within several picoseconds, the electron subsystem thermalizes with the lattice, leading to strain wave generation and thermally induced reflectivity change. The thermal effect is observed as a slowly decaying background in Fig. 4.3a. Since only signals caused by strain waves are relevant, we remove the thermal background by applying a zero-phase high pass filtering with 15 GHz cutoff frequency. The filtered signals and fitted curve are shown in Fig. 4.3b.

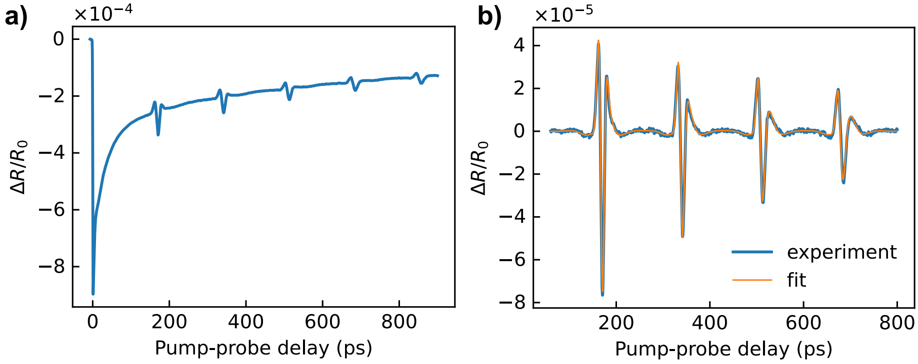

Figure 4.3: a) Experimental measurement performed on 400 nm thick flat Zr membrane. b) Experimental curve after applying 15 GHz high-pass filtering and best-fit simulation curve.

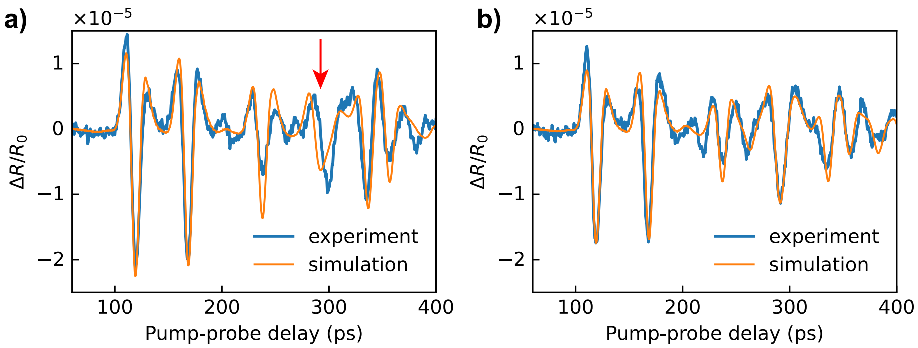

Figure 4.4: Experimental results and simulations for 50 % duty cycle gratings with a) 600 nm and b) 400 nm pitch. The red arrow highlights the diffraction peak, of which the timing is influenced by the grating lineshape (see text for details).

4.3 RESULTS AND DISCUSSION

4.3.1 RETRIEVING GRATING PITCH, DUTY CYCLE, AND GRATING LINESHAPE

In Figure 4.4 we show measured and simulated reflectivity curves for 600 nm and 400 nm pitch gratings, both with 50 % duty cycle. The simulations show a clear sensitivity to the structural properties, and the best match between simulation and experiment is found for grating linewidths of 264 nm and 164 nm respectively. A further analysis of the sensitivity of these experiments to pitch and duty cycle is given in Section 4.3.2 (Fig. 4.6). The observed correspondence between simulations and measurements shows the ability to quantitatively determine structural properties of such buried nanostructures using picosecond ultrasonics.

However, in the results of Fig. 4.4 some discrepancy between theory and measurements remains. In particular, the timing of the diffraction echo (peak 4) does not match the expectation for the 600 nm pitch grating, and simulations show that this timing is not sensitive to the grating pitch and linewidth (see Fig. 4.6). As this particular peak originates from acoustic diffraction at the line edges, we therefore hypothesize that the diffraction echo shape and timing is sensitive to the exact shape of the buried features. While the simulations shown in Fig. 4.4 assumed grating lines with a rectangular profile, the finite spot of the focused ion beam and redeposition effects during the milling process typically result in a non-rectangular profile of the fabricated patterns.

To investigate this possibility, we measured the $\Delta R/R_0$ response of multiple gratings with varying parameters and performed simulations that include varying lineshapes, which we compared to SEM cross sections of the gratings. We fabricated a set of 600 nm pitch gratings with nominal linewidths 100 nm, 200 nm and 300 nm, as well as 400 nm and 800 nm pitch gratings with 50 % duty cycle. All gratings were fabricated on the same freestanding Zr membrane. The resulting signals are shown in Fig. 4.5a, together with the fit results. As a reference for the lineshape model, side-view images of the fabricated structures were recorded by milling a rectangular aperture through the membrane near the side of each structure and taking an SEM image at oblique angle (Fig. 4.5b). The oblique SEM viewing angle did not allow a quantitative comparison, as the exact viewing angle could not be calibrated and the resolution was limited in this configuration. Nevertheless, these images clearly show more rounded lineshapes, with significant variations for different linewidths, and consistent sidewall angles.

To assess the sensitivity of the photoacoustic response to such shapes, we expand the simulations to model the grating sides with a smoother lineshape consistent with the shapes seen in the SEM images. This lineshape is an inverted isosceles trapezoid with rounded corners which is parametrized by base angle and radii of top and bottom curvatures. Figure 4.5c shows the optimized shape for each grating, while the corresponding simulated $\Delta R/R_0$ signals for all these structures are overlaid with the measured data in Fig. 4.5a. For comparison, the grey traces correspond to the best-matching simulations when assuming rectangular lineshapes. For all signals, the improvement resulting from the optimized lineshapes is clear, especially around the diffraction echo, which is indicated by the red arrow in each trace. A general observation is that the simulated signals using the optimized lineshape accurately predict the timing of the diffraction echo. Thus, the measured time dependence of $\Delta R/R_0$ indeed contains sufficient information to determine both the grating parameters and the lineshapes. Overall, very good agreement is obtained between simulation and experiment. This agreement persists even for the narrowest lines used in these experiments, with a width of only 100 nm. Using a parametrization of the nanostructures, such as the rounded trapezoid-type lineshapes discussed above, enables a fitting procedure to determine the lineshape that best matches the experimental data (see Section 4.3.2, Fig. 4.8). We find that other parametrizations can be used in a similar way, such as a sigmoidal lineshape (see Section 4.3.2, Fig. 4.9).

4.3.2 SENSITIVITY TO GRATING PARAMETERS

Figure 4.6 shows measured signals from a grating with a nominal pitch of 600 nm and 50 % duty cycle, together with simulation results for different pitches and duty cycles, assuming a rectangular profile of grating lines. In Fig. 4.6a, simulations with varying pitch are compared to the data, and it can be concluded that the sensitivity to pitch is limited, although a variation of 60 nm leads to a detectable difference in signal. Pitch mainly affects the amplitude of the diffraction peak. The sensitivity to duty cycle is much higher, having a strong effect on the relative height of peaks 1

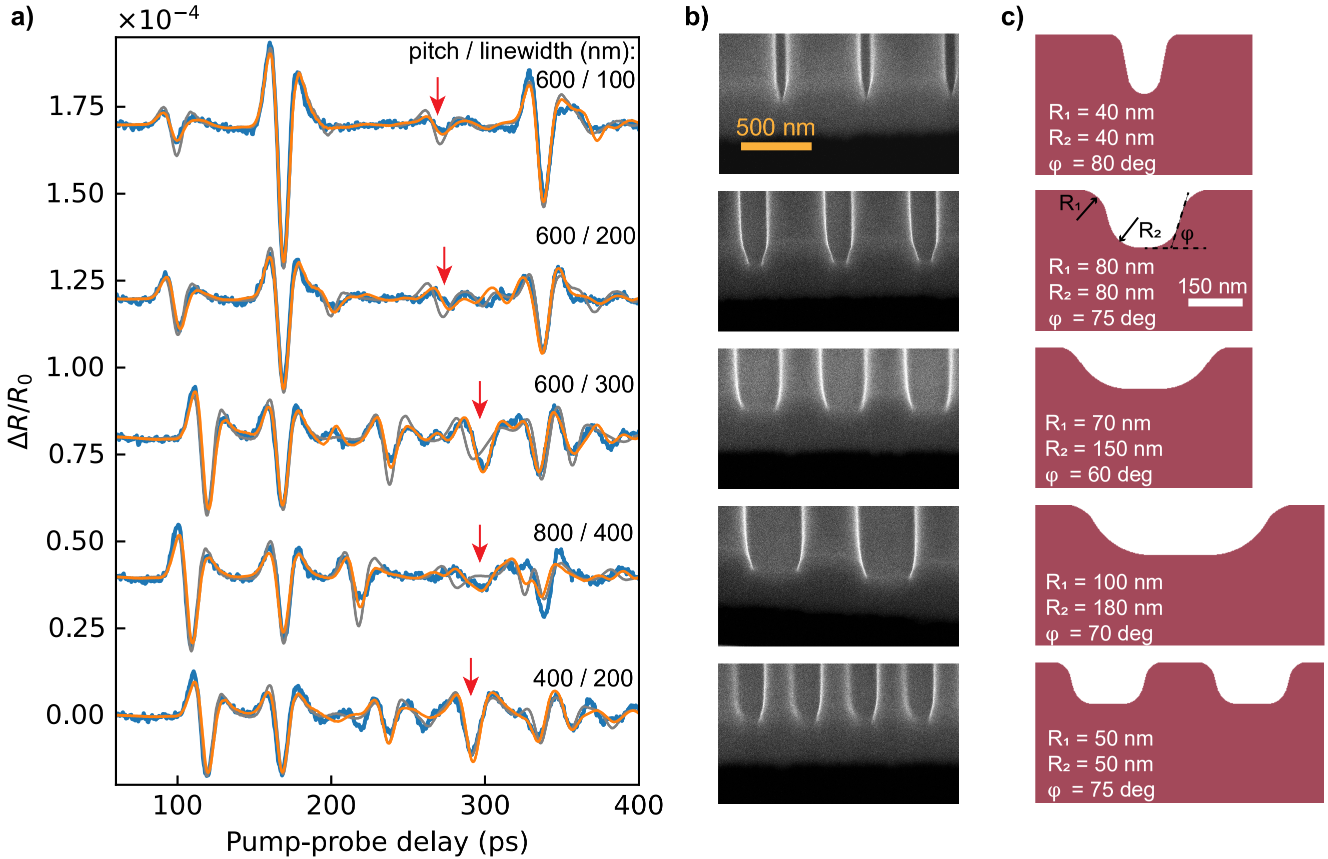

Figure 4.5: Sensitivity to nanoscale shape variations. a) $\Delta R/R_0$ traces for various values of pitch and duty cycle. Blue curves represent experimental measurements, grey - best-matching simulations with rectangular lineshapes, and orange - simulations with rounded lineshapes. Orange curves show reasonably better agreement with experimental measurements, especially around the diffraction peak (depicted by red arrows). b) SEM images of gratings cross sections taken at an oblique angle. Significant deviations from the rectangular shape of grating lines are observed. c) Rounded profiles of grating lines used to simulate orange traces in a).

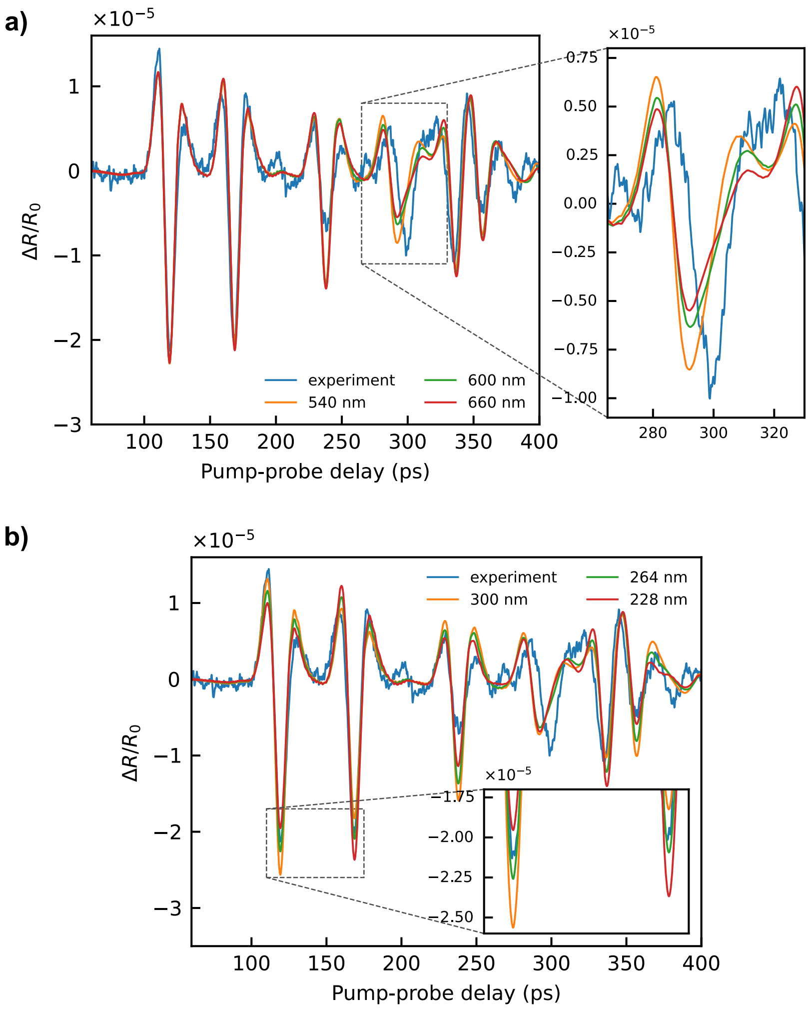

Figure 4.6: Dependence of the time-dependent reflectivity on pitch and linewidth of the grating. a) Simulated reflectivity change curves for different pitch (values indicated in the legend). The linewidth is fixed at 264 nm. b) Simulated reflectivity change curves for different linewidths (values indicated in the legend). The pitch is fixed at 600 nm.

and 2. Comparing simulation results to the experimental data, the 30 nm variations shown in Fig. 4.6b are readily discernible.

However, one can see from Fig. 4.6 that the discrepancy between theory and measurements can not be fully eliminated by adjusting only the pitch and linewidth of the grating. The disagreement is the strongest for the longer delay when the acoustics diffraction plays a significant role. A particular mismatch is the wrong timing of the diffraction peak highlighted in Fig. 4.6a. We hypothesize that the shape of the grating lines affects the shape of later echoes. The simplest modification of the grating lineshape is to introduce the inclination of the side walls of the lines. Figure 4.7 shows the reflectivity curves for different inclination angles. Note that for different inclination angles, the duty cycle of the grating was adjusted (Fig. 4.7b) to maintain the correct ratio of the amplitudes of the first two echoes. One can see that the inclination of the line walls changes the reflectivity curves. For an inclination of 70 degrees, the shape of the diffraction peak is very close to the one measured in the experiment. However, the mismatch in the amplitude of the echo 3 remains.

The fits in Figs. 4.6 and 4.7 show the clear limitations when comparing experimental data with rectangular or trapezoidal lineshapes. As shown in Section 4.3.1, including the rounded shapes at the top and bottom corners of the grating lines leads to a much more accurate fit to the experimental data. To assess the sensitivity to these structural parameters, Fig. 4.8 shows the effect of a variation of each parameter separately. In each panel, the green trace represents the best fit to the data, while the red and orange curves show the effect of increasing or decreasing the value of one

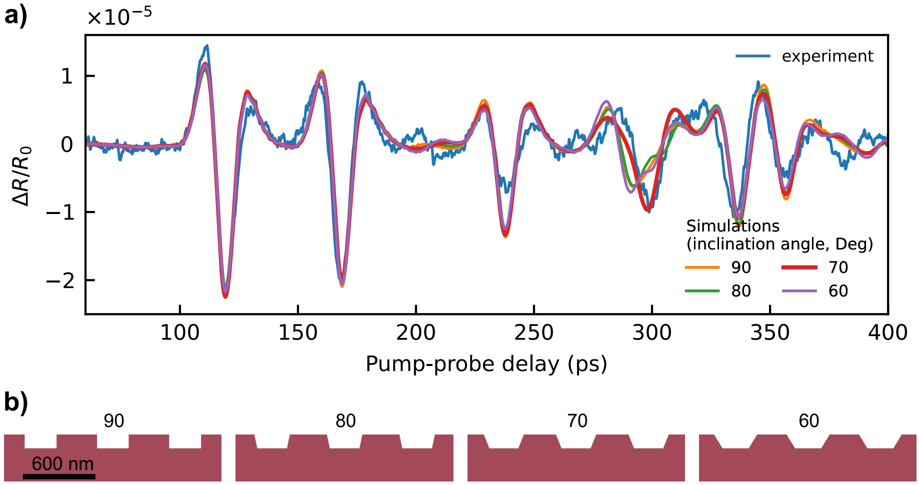

Figure 4.7: a) Dependence of the time-dependent reflectivity curves on the inclination of grating line walls. The peak associated with acoustic diffraction is most sensitive to small lineshape variations. b) Profiles of grating lines used in simulations.

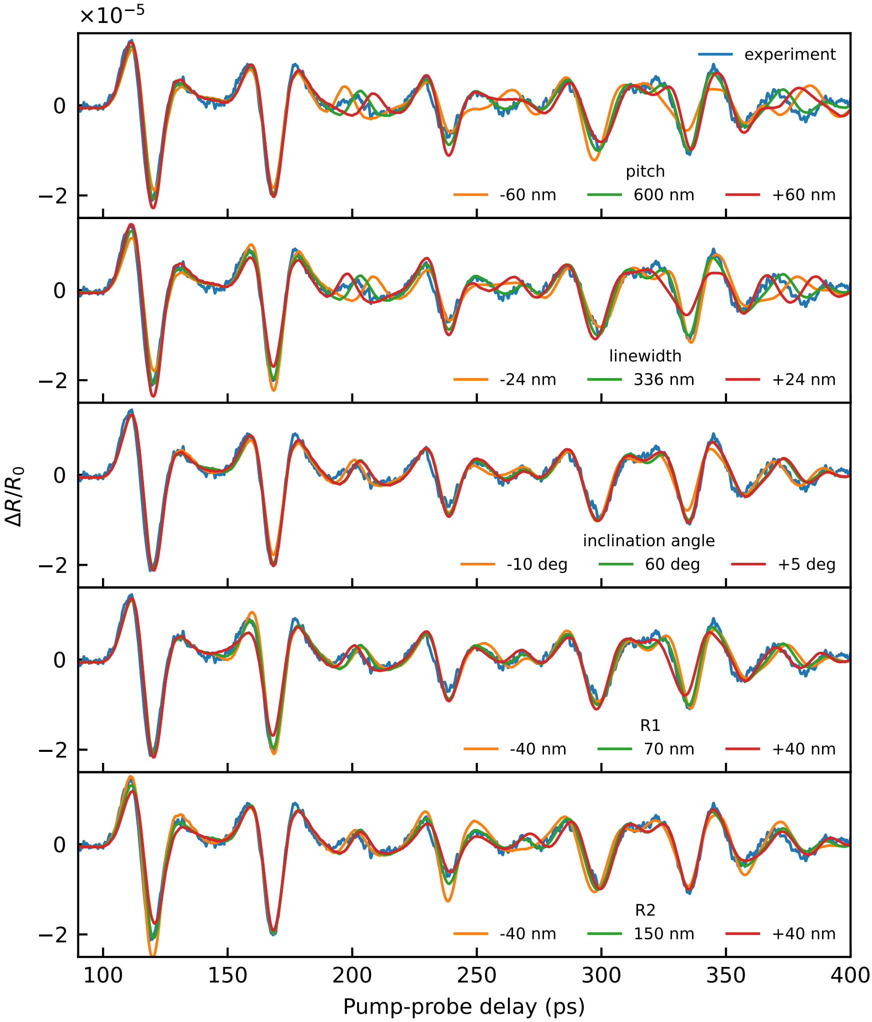

Figure 4.8: Sensitivity of simulated reflectivity curves of a nominal 600 nm pitch grating with 300 nm linewidth to grating parameter variations. Each subplot represents variations in one grating parameter depicted in the legend. Blue curves represent experimental measurements. Green curves show the simulation with optimal grating parameters. Orange and red curves show simulations with deviations in grating parameters from optimal values. Inclination angle is the angle of the sidewalls (where 90 degrees corresponds to a rectangular lineshape). R1 is the radius of curvature of the top corners of the lines, while R2 is the radius of curvature of the bottom corners. See Fig. 4.5 in Section 4.3.1 for a graphical representation.

parameter by an amount that leads to a clear deviation from an optimal fit. From these traces, it can be seen that the sensitivity to each parameter is in the range of 20-60 nm for our Zr samples. The sensitivity to a change in sidewall angles seems to be on the order of 10 degrees, although this parameter is not fully independent of the curvatures and line height: for the present fit, a sidewall angle above 65 degrees would not be realistic, as it would not be possible to parametrize a lineshape with the optimized curvatures, line height and line width using such steep angles. While the multi-parameter nature of the fits makes it challenging to define error bars on each individual parameter, Fig. 4.8 shows that each parameter has a distinct effect on the overall time-dependent reflectivity signal, giving further confidence in the uniqueness of the fits.

As an alternative, intuitive way to parametrize such rounded gratings, we also considered a sigmoidal lineshape of the form:

$$h = \frac{1}{1+\exp\left(\frac{x-x_0}{m}\right)} \tag{4.10}$$

in which x_0 is the center position of the edge, and the parameter m controls the amount of smoothing of the edge (with $m \to 0$ describing a step-like edge, and larger m values correspond to increased smoothing). Simulations with various amounts of curvature are shown in Fig. 4.9. One can see that the inclination of line walls and the rounding of line edges helps both with the time position of the diffraction peak and the amplitude of the peak 3. While these simulations are illustrative, the chosen sigmoidal lineshape links the inclination and roundness of edges, limiting

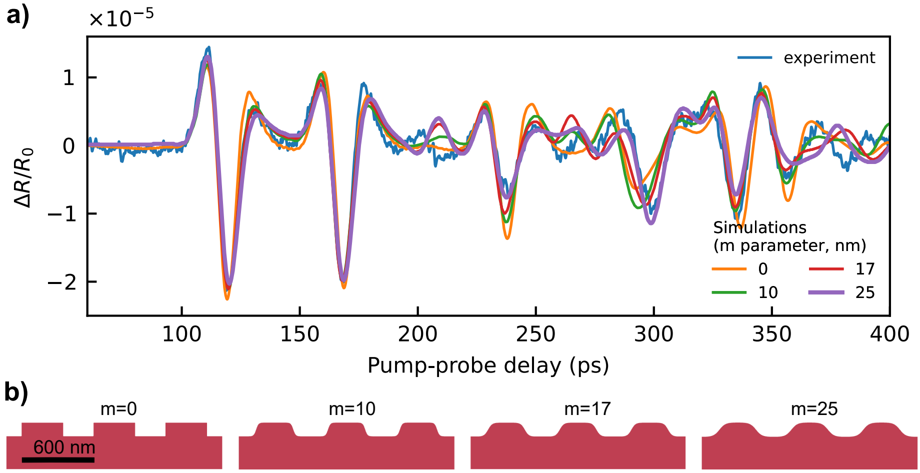

Figure 4.9: a) Dependence of the time-dependent reflectivity curves on the m parameter of the grating lineshape. Rounded lineshapes give better agreement with experiments than just inclined line walls. b) Profiles of grating lines used in simulations.

the freedom of fitting. Even better agreement between theory and experiments is achieved (see Section 4.3.1 and Fig. 4.8) by independently adjusting the inclination and roundness of the edges, although this sigmoidal shape already provides a simple and intuitive lineshape model.

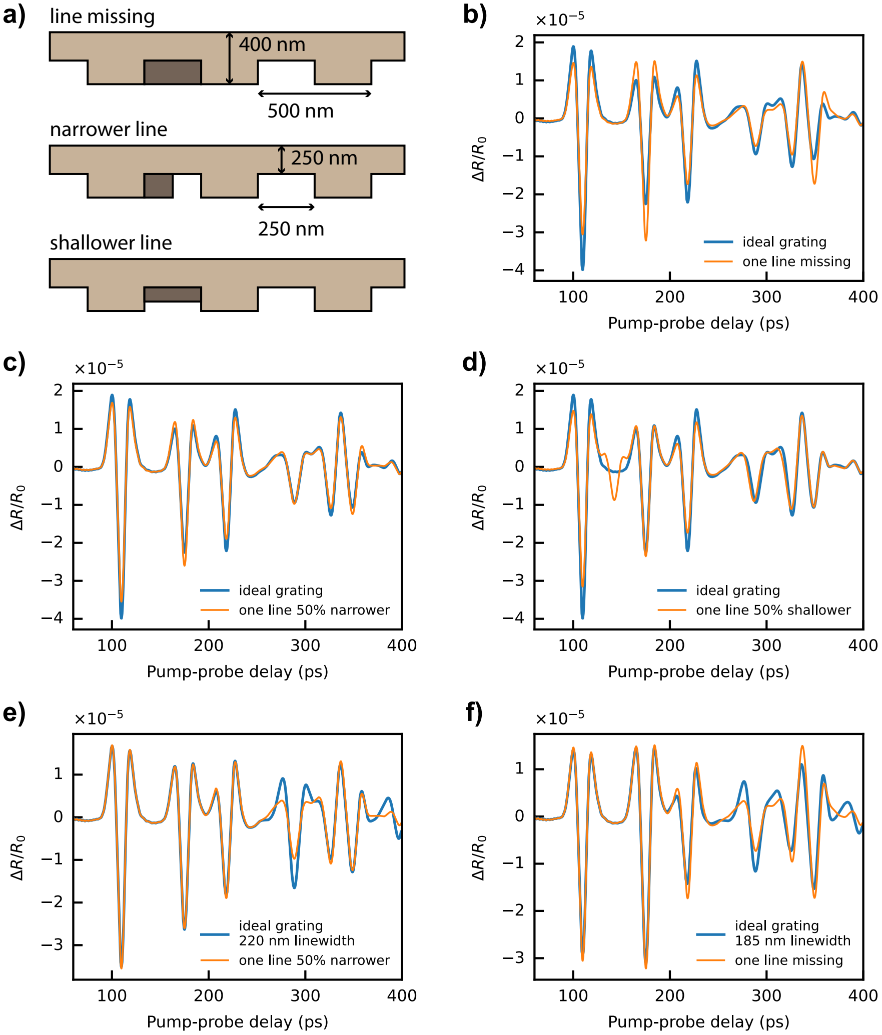

Figure 4.10: Sensitivity to grating defects. a) Schematics of the simulated gratings with defects. b)-d) Comparison of reflectivity curves obtained from the ideal grating and the grating containing a defect. e)-f) Comparison of signals from gratings with defects and ideal gratings with adjusted linewidth.

4.3.3 Detecting defects

In the present work, the measured $\Delta R/R_0$ signals were averaged over the spatial scale of the probe spot, which in principle limits the reconstruction ability to either periodic or isolated nanostructures. However, picosecond ultrasonics can be expected to be sensitive to defects in a perfect periodic structure as well, as such defects affect the acoustic diffraction as well. To explore this possibility, we performed simulations in which we introduce defects into a periodic pattern. Three different types of defects are investigated, as shown in Figure 4.10a, where a single grating line is either missing completely, 50 % narrower, or 50 % shallower than intended. In all cases, we assume a FWHM probe spot diameter of 2 µm. Figures 4.10b-d show the resulting reflectivity signals compared to the defect-free case. Each of these defects leads to a distinct difference in signal, with a magnitude that can readily be detected with the measurement sensitivity of our system. Importantly, the defect-induced signal shape cannot be mimicked by a change in the various fit parameters. Examples of such parameter adjustments are shown in Figures 4.10e,f, where a fit was attempted to a defect-free grating with an adjusted duty cycle to correct for the defect-induced signal shape change. While such a parameter adjustment can correct for the height of some of the echoes (in this case the first two), the fit quality is significantly reduced. We therefore conclude that picosecond ultrasonics can be used to identify the presence of defects in nanoscale structures as well. A smaller probe spot would sample a reduced number of grating lines, which would further increase the sensitivity to nanoscale defects and isolated structures. Using more advanced parametrization, it should be feasible to characterize the shape of the defects. By developing more advanced measurement concepts based on e.g. detailed sampling of the acoustic diffraction as a function of spatial position, we expect that the approach extends to more complex 3D nanostructures as well.

4.4 Conclusion

From the analysis of present experiments and a comparison with simulations for a range of different grating parameters, we conclude that we can retrieve pitch, linewidth and lineshape features with a sensitivity in the range of tens of nanometers. We also have shown the possibility of defect detection in such structures. It is worth noting that this has been achieved using infrared light with a wavelength of 780 nm, which exceeded the pitch of the detected gratings, and optical spot diameters of 2-4 µm. The sensitivity to nanoscale structural features results from the extremely short acoustic wavelengths propagating in the material. In the case of Zr, the central wavelength of the optically generated acoustic wavepacket was around 150 nm. The frequency content of the thermoelastically generated phonon wavepacket is mainly determined by the optical absorption depth and electron transport properties of the material. In many materials, particularly optically opaque ones, such high-frequency phonon wavepackets can then be generated with appropriate pump beam properties. Therefore, picosecond ultrasonics has significant potential as a metrology tool for optically opaque nanostructures.

5

PROBING PERIODIC SUB-MICRON METAL STRUCTURES ON TRANSPARENT SUBSTRATES WITH PICOSECOND ULTRASONICS

5.1 INTRODUCTION

As demonstrated in Chapter 4, picosecond ultrasonics shows strong potential for imaging nanostructures hidden beneath optically opaque materials. The core principle of the method is that the presence of a nanostructure beneath the opaque layer produces a unique transient reflectivity time trace. Light-induced acoustic waves undergo multiple reflections from the buried structures, which results in unique acoustic diffraction components. Those diffraction components are specific to the geometry of nanostructures. As a result, their amplitude and time of arrival at the top surface differs per sample, causing variations in the $\Delta R/R_0$ signals. Through comprehensive numerical modeling, one can fit the shape and dimensional parameters of the underlying nanostructures to achieve agreement between simulated and experimentally obtained $\Delta R/R_0$ traces. However, this approach has an obvious drawback. It requires significant computational resources to perform the fitting procedure. This naturally raises the question of whether structural information can be extracted directly from the measured transient reflectivity, without resorting to full-scale fitting.

Another related question is whether the method can also be applied to directly observable structures. Such structures may be deposited on the surface of a sample or covered by thick transparent layers. Direct excitation by the pump beam induces vibrations in these structures, which can subsequently be detected by the probe

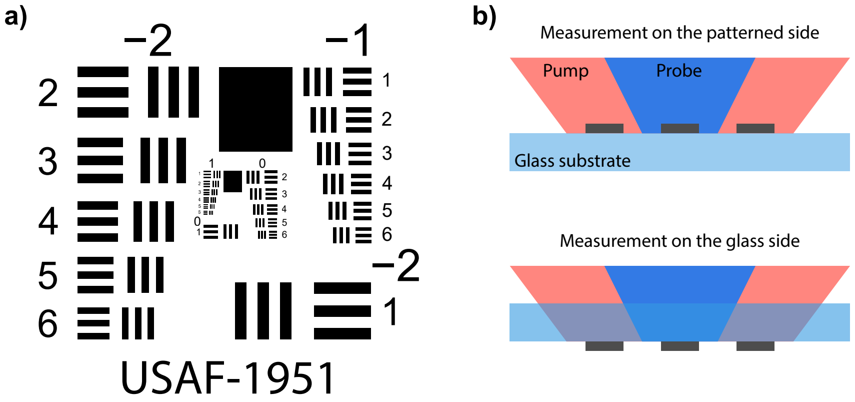

Figure 5.1: a) Schematic of the 1951 USAF resolution test chart used in experimental studies. b) Two experimental schemes of measurements on patterned and unpatterned sides of the resolution target. The pump beam homogeneously illuminates the entire group of lines, while the probe beam is focused on the central line of the group.

beam. The vibration frequencies depend on the material, dimensions, shape, and surrounding environment of the structures [40–42, 128, 129]. With prior knowledge of the material properties, structural information should be extractable in a manner analogous to the approach outlined in Chapter 4.

In this chapter, we investigate the correlation between the measured transient reflectivity and the period of metal gratings deposited on a glass substrate.

5.2 EXPERIMENTAL DETAILS AND SAMPLE DESCRIPTION

We use a positive resolution test target Edmund USAF 1951 (Fig. 5.1a) as an experimental sample. This test target is a 1.5 mm thick glass substrate with deposited chromium line triplets (groups) of various widths. We studied the groups with the highest density of line pairs, namely 406, 456, 512, 575 and 645 line pairs per mm, that corresponds to 1232, 1096, 978, 870 and 775 nm width of the individual lines, respectively. The spacing between lines is equal to the linewidth. Line thickness is around 50 nm and the line length is 5 times larger than its width.

The details on the experimental pump-probe setup are described in Chapter 2. The measurement schemes are shown in Fig. 5.1b. Generation and detection were performed on the patterned and unpatterned (through the glass) sides of the sample. In both cases, the pump beam is weakly focused to illuminate the entire line triplet. This implies homogeneous excitation of each line, resulting in in-phase vibrations of the triplet. The probe beam is focused onto the central line of the triplet and has approximately 1 μm $1/e^2$ radius.

5.3 RESULTS AND DISCUSSION

As shown in Fig. 5.1, the line triplets have a square shape. The pump focus spot is adjusted to fully cover the entire triplet, ensuring homogeneous illumination of the line surfaces. The pump pulse energy is absorbed by the electrons in the chromium lines and subsequently transferred to the lattice as heat. This increase in lattice temperature induces thermal stress, which is then released in the form of acoustic vibrations. Due to the low thickness of the lines and the high electronic thermal conductivity, the temperature distribution within each line can be considered uniform. As a result, the lines undergo periodic contractions and expansions along their length, width, and height. These oscillations are coupled through Poisson's ratio, giving rise to complex vibrational modes. Some of these modes can be detected by transient reflectivity measurements [41, 128].

Figure 5.2 presents reflectivity change signals measured from the unpatterned side of the sample at five different line triplets. The signals consist of a slowly decaying thermal background, with superimposed ΔR oscillations on timescales of $\sim 45\,\text{ps}$ and several hundred picoseconds. The high-frequency oscillations arise from the Brillouin effect. Vibrations of the photoexcited chromium lines generate strain pulses that propagate into the glass substrate. Interference between probe light

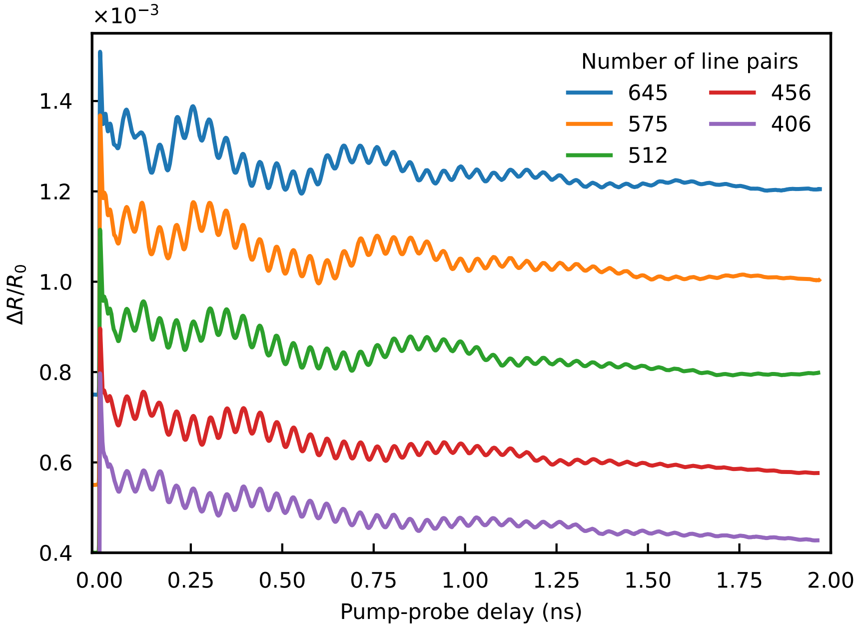

Figure 5.2: Measurements of reflectivity change on the unpatterned side of the sample. Strong Brillouin oscillations are visible superimposed on a low frequency signal. A vertical offset between the different traces is applied for clarity.

reflected from the chromium lines and probe light reflected from the propagating in glass strain pulse produces oscillatory reflectivity variations. For normal incidence, the frequency of these oscillations is given by $f = 2nc/\lambda = 2 \cdot 1.47 \cdot 5800/780 = 21.9\,\mathrm{GHz}$, where n is the refractive index, c is the speed of sound, and λ is the wavelength of the probe light. This value agrees well with the experimentally obtained spectra shown in Fig. 5.3. As seen in Fig. 5.2, the Brillouin oscillations gradually decay and nearly vanish around 1.75 ns, which is caused by the limited coherence length of the probe light. For a 100 fs probe pulse, the coherence length in glass is $\sim 20\,\mu\mathrm{m}$, corresponding to approximately twice the distance a sound wave travels in 1.75 ns.

The low-frequency components (1–10 GHz, Fig. 5.3) originate from vibrations of the lines themselves. Due to strong attenuation from coupling into the glass substrate, these modes exhibit significant spectral broadening, preventing the clear observation of individual frequency components, except for a distinct peak around 2 GHz. The position of this peak shows a linear dependence on the line density (Fig. 5.4). From the slope of this dependence, an effective propagation speed of 3290 m/s is extracted. This value is substantially lower than the longitudinal sound

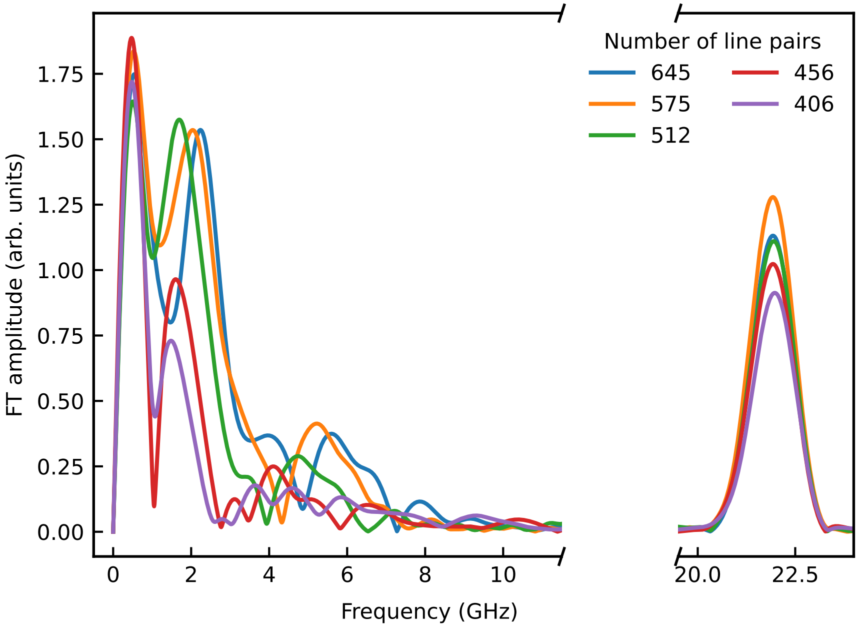

Figure 5.3: FFT spectra of signals shown in Fig. 5.2. To eliminate the strong DC component caused by a thermal background, the mean was subtracted from the signals before applying the FFT. Zero padding and Blackman windowing were also applied. The frequencies of vibrational modes are located in 1–10 GHz range. Brillouin components are detected around 22 GHz for all line groups.

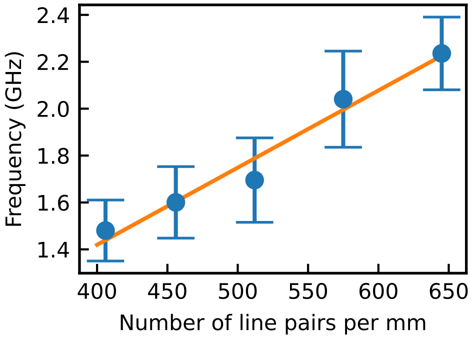

Figure 5.4: Frequency of the spectrum peak near 2 GHz (from Fig. 5.3) vs density of line pairs. In Fig. 5.3, positions of spectral peaks can be obtained with an accuracy not lower than the width of the spectral peak at 95 % level. These confidence intervals are represented by error bars. The orange line is the linear fit. Fitted parameters: slope – 3290 m/s and offset – 0.1 GHz.

velocity in chromium (6600 m/s), indicating that these modes cannot be attributed to simple width-wise contractions and expansions. Instead, they correspond to more complex vibrational modes. Since the frequencies of such modes depend not only on linewidth but also on other parameters including line length, thickness, and the acoustic impedance contrast between substrate and lines, extracting precise information about linewidth is not feasible. Additional complications arise from the strong attenuation of line vibrations through acoustic coupling into the substrate, which further broadens spectral components and obscures fine spectral features.

An alternative approach to retrieving linewidth from measured transient reflectivity is to examine specific features in the time domain of the signals. In Fig. 5.2, the low-frequency modulation exhibits an oscillatory behavior, but lacks a well-defined harmonic structure. Of particular interest is the drop in the ΔR signal occurring at a delay time of 100–200 ps. Due to the superimposed Brillouin oscillations, it is challenging to precisely determine the timing of this reflectivity drop. To address this, we performed measurements on the patterned side of the sample, where the line triplets are directly exposed to the pump and probe beams. The resulting transient reflectivity traces are shown in Fig. 5.5. In these traces, Brillouin oscillations are largely suppressed because the chromium lines block most of the probe light from penetrating the glass substrate. While the low-frequency modulation is also less pronounced, the reflectivity drop around 150 ps is clearly observed. This timing can be interpreted as the moment when the line reaches its maximum width. Following pump excitation, expansion waves are launched from all edges of each line. Each line experiences three pairs of such waves along its three axes, traveling in opposite directions. The line continues to expand until the expansion waves reach the opposing edges, at which point they reflect from the free surfaces and convert into contraction waves. Therefore, we hypothesize that the reflectivity drop around 150 ps corresponds to the arrival of expansion waves at the edges along the width of the chromium line. The slope from the linear fit in Fig. 5.6 provides the speed of this expansion wave, yielding a value of 6410 m/s, which is close to the longitudinal sound velocity in chromium. The slight discrepancy can be attributed to the fact that the expansion wave in this case is not a pure longitudinal wave, due to the finite thickness of the chromium line and consecutive boundary effects. Another notable feature of the linear fit in Fig. 5.6 is the vertical offset of 137 nm, indicating that, for all linewidths, the reflectivity drop occurs approximately 21 ps earlier than expected. The origin of this time shift remains unclear.

Figure 5.7 presents overlapping measurements taken from the patterned and unpatterned sides of the sample. Apart from the Brillouin oscillations, the traces agree well during the first 200 ps. However, at longer time delays, significant deviations appear between measurements from opposite sides of the sample, with stronger deviations observed for higher line densities (narrower lines). These differences are most likely caused by the detection of acoustic waves propagating in the glass substrate. When probing from the unpatterned side, the light is focused through the glass substrate. The strain distribution in the acoustic wave propagating in the

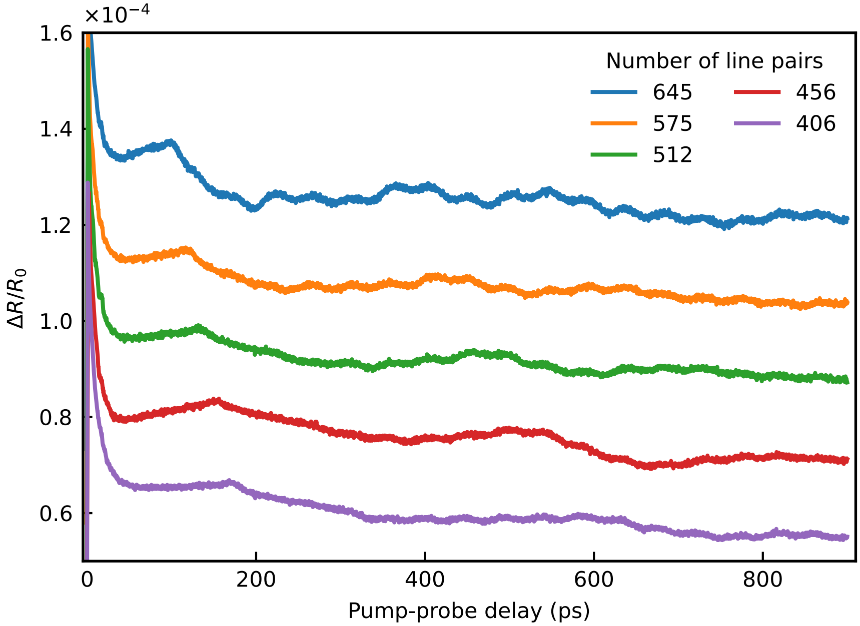

Figure 5.5: Measurements of reflectivity change on the patterned side of the sample. Brillouin oscillations are still visible, but their amplitude is much smaller. A vertical offset between the different traces is applied for clarity.

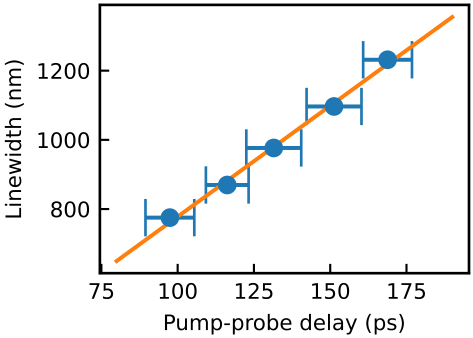

Figure 5.6: Time delay of the reflectivity drop (see Fig. 5.5) vs linewidth (blue dots). The time delay is obtained by applying 50 GHz lowpass zero-phase filtering and locating the maximum value in 100–200 ps window. In the vicinity of these maxima, the filtered curves exhibit a bell-shaped profile with a width of approximately 20 ps, as represented in this figure by the error bars. The orange line is the linear fit. Fitted parameters: slope – 6410 m/s and offset – 137 nm.

glass already exhibits a complex spatial structure due to the non-trivial geometry of the acoustic transducer (line triplets). Moreover, this wave packet propagates through the probe's focal region over a distance exceeding the Rayleigh length. The acousto-optic interaction of such a complex strain field with a non-planar light wave results in additional reflectivity modulation beyond the Brillouin oscillations.

Together with the transient reflectivity, Fig. 5.7 also presents a simulation of the influence of a relative change in width of the central line of the triplet. The two-dimensional numerical simulations were performed under the assumption of infinitely long lines of the triplets, using the numerical approach described in Chapter 1. The relative width change was calculated by integrating the longitudinal strain component ε_{yy} across the width of the lines and averaging along their height. As shown in Fig. 5.7, all three traces exhibit significant disagreement for the highest line density. However, in the other two cases, the simulated curves show reasonably good agreement with the signals measured from the patterned side of the glass. A notable feature is a 20 ps shift of the simulated drop at around 150 ps relative to the experimental signals. This shift coincides with the vertical offset of the linear fit showed in Fig. 5.6. The similarity between simulated and experimental curves raises the question of the physical origin of the measured reflectivity change. Specifically, whether the signal originates from optical modifications in the chromium lines induced by the photoelastic effect, or from a purely geometrical mechanism, i.e., modulation of the effective reflection area due to linewidth vibrations. In our simulations, a two-dimensional approximation results in the neglect of elastic waves generated at the short edges of the lines and propagating along their length. However, such waves should be considered, as for the narrowest lines, they are expected to reach the center of the line around 300 ps, which falls within the experimental

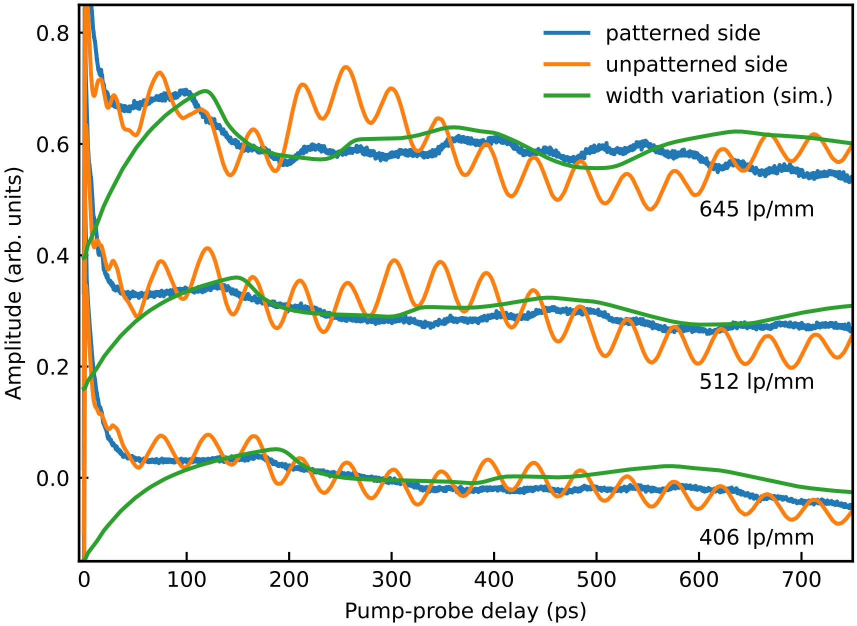

Figure 5.7: Overlapped traces of transient reflectivity measurements on patterned and unpatterned sides, together with simulated variation of the width of the central line of the triplet. The amplitude of the traces was adjusted for easier comparison.

measurement window. This could account for the discrepancy observed between simulation and experiment for the 645 lp/mm triplet in Fig. 5.7. To test whether our measurements are sensitive to elastic waves propagating along the lines, we repeated the experiment on the 645 lp/mm triplet with the probe beam displaced by 1 µm from the line center along its length. The resulting signals were indistinguishable from those obtained at the center of the line. This observation suggests that our measurements are not sensitive to elastic waves propagating along the line length. It further supports the conclusion that the origin of the reflectivity change is most likely a geometrical modification of the line shape. Since the probe beam was circularly polarized, coupling to the orthogonal strain components ε_{xx} and ε_{yy} should occur with equal efficiency. If the strain component ε_{xx} associated with waves propagating along the line length is undetectable, then ε_{yy} should likewise remain undetectable under these conditions. We therefore hypothesize that the detected signals primarily arise from variations in linewidth. Because the probe focus spot is larger than the linewidth, the measurement is sensitive to transverse expansions and contractions, while displacements along the line length remain undetected. Even when the probe beam was shifted by 1 µm toward the short edge of the line, the focus spot still remained within the linewidth, thereby preventing detection of longitudinal expansion.

5.4 CONCLUSION

The present study investigated whether the current PU technique can characterize isolated, sub-optical-wavelength structures without relying on complete numerical modeling and subsequent fitting to experimental data, as was done in Chapter 4. Experiments on an optical resolution test target revealed apparent differences in the measured photoacoustic response between groups with different line pair densities. Specific signal features, such as frequency components and time domain signatures, exhibited a linear dependence on line pair density. This linear trend suggests promise for retrieving grating parameters from measured signals. However, practical challenges remain in the calibration procedure. This study focused only on the retrieval of grating linewidth. Other geometric parameters of the grating were not investigated and could substantially influence the photoacoustic response. Consequently, to reliably extract complete grating parameters, full numerical simulation (preferably 3D) followed by fitting to experimental data appears necessary.

Moreover, the effect of acoustic coupling between neighboring lines is of interest for further study. Exploring this phenomenon could clarify the technique's ability to distinguish isolated elements from closely spaced groups.

BIBLIOGRAPHY

[1] S. D. Brorson, A. Kazeroonian, J. S. Moodera, D. W. Face, T. K. Cheng, E. P. Ippen, M. S. Dresselhaus, and G. Dresselhaus, *Femtosecond room-temperature measurement of the electron-phonon coupling constant γ in metallic superconductors,* Physical Review Letters **64**, 2172 (1990).

[2] R. H. M. Groeneveld, R. Sprik, and A. Lagendijk, *Femtosecond spectroscopy of electron-electron and electron-phonon energy relaxation in Ag and Au,* Physical Review. B, Condensed Matter **51**, 11433 (1995).

[3] A. Block, M. Liebel, R. Yu, M. Spector, Y. Sivan, F. J. G. de Abajo, and N. F. van Hulst, *Tracking ultrafast hot-electron diffusion in space and time by ultrafast thermomodulation microscopy,* Science Advances **5**, eaav8965 (2019).

[4] M. Maiuri, M. Garavelli, and G. Cerullo, *Ultrafast Spectroscopy: State of the Art and Open Challenges,* Journal of the American Chemical Society **142**, 3 (2020).

[5] S.-W. Lee, S.-J. Kim, and O.-H. Kwon, *Global Lifetime Analysis on Excited Three-State Reactions,* The Journal of Physical Chemistry A **129**, 5200 (2025).

[6] A. Ghosh, A. Liu, S. C. Boehme, P. Brosseau, D. N. Dirin, M. V. Kovalenko, and P. Kambhampati, *Correlated Lattice Fluctuations in CsPbBr3 Quantum Dots Give Rise to Long-Lived Electronic Coherence,* ACS Nano **19**, 19927 (2025).

[7] C. Thomsen, J. Strait, Z. Vardeny, H. J. Maris, J. Tauc, and J. J. Hauser, *Coherent Phonon Generation and Detection by Picosecond Light Pulses,* Physical Review Letters **53**, 989 (1984).

[8] C. Thomsen, H. T. Grahn, H. J. Maris, and J. Tauc, *Surface generation and detection of phonons by picosecond light pulses,* Physical Review B **34**, 4129 (1986).

[9] G. L. Eesley, B. M. Clemens, and C. A. Paddock, *Generation and detection of picosecond acoustic pulses in thin metal films,* Applied Physics Letters **50**, 717 (1987).

[10] O. B. Wright and T. Hyoguchi, *Ultrafast vibration and laser acoustics in thin transparent films,* Optics Letters **16**, 1529 (1991).

[11] O. Wright, *Thickness and sound velocity measurement in thin transparent films with laser picosecond acoustics,* Journal of Applied Physics **71**, 1617 (1992).

[12] O. B. Wright, *Laser picosecond acoustics in double-layer transparent films,* Optics Letters **20**, 632 (1995).

[13] A. Devos and A. Le Louarn, *Strong effect of interband transitions in the picosecond ultrasonics response of metallic thin films,* Physical Review B **68**, 045405 (2003).

[14] R. M. Slayton, K. A. Nelson, and A. A. Maznev, *Transient grating measurements of film thickness in multilayer metal films,* Journal of Applied Physics **90**, 4392 (2001).

[15] A. M. Lomonosov, A. Ayouch, P. Ruello, G. Vaudel, M. R. Baklanov, P. Verdonck, L. Zhao, and V. E. Gusev, *Nanoscale Noncontact Subsurface Investigations of Mechanical and Optical Properties of Nanoporous Low-k Material Thin Film,* ACS Nano **6**, 1410 (2012).

[16] H. Zhang, A. Antoncecchi, S. Edward, P. Planken, and S. Witte, *Ultrafast laser-induced guided elastic waves in a freestanding aluminum membrane,* Physical Review B **103**, 064303 (2021).

[17] G. Tas, J. J. Loomis, H. J. Maris, A. A. Bailes, III, and L. E. Seiberling, *Picosecond ultrasonics study of the modification of interfacial bonding by ion implantation,* Applied Physics Letters **72**, 2235 (1998).

[18] M. Hettich, A. Bruchhausen, S. Riedel, T. Geldhauser, S. Verleger, D. Issenmann, O. Ristow, R. Chauhan, J. Dual, A. Erbe, E. Scheer, P. Leiderer, and T. Dekorsy, *Modification of vibrational damping times in thin gold films by self-assembled molecular layers,* Applied Physics Letters **98**, 261908 (2011).

[19] A. Devos and P. Emery, *Thin-film adhesion characterization by Colored Picosecond Acoustics,* Surface and Coatings Technology **352**, 406 (2018).

[20] S. Edward, A. Antoncecchi, H. Zhang, H. Sielcken, S. Witte, and P. C. M. Planken, *Detection of periodic structures through opaque metal layers by optical measurements of ultrafast electron dynamics,* Optics Express **26**, 23380 (2018).

[21] S. Edward, H. Zhang, I. Setija, V. Verrina, A. Antoncecchi, S. Witte, and P. Planken, *Detection of Hidden Gratings through Multilayer Nanostructures Using Light and Sound,* Physical Review Applied **14**, 014015 (2020).

[22] V. Verrina, S. Edward, H. Zhang, S. Witte, and P. C. M. Planken, *Photoacoustic detection of low duty cycle gratings through optically opaque layers,* Applied Physics Letters **117**, 051104 (2020).

[23] A. Antoncecchi, H. Zhang, S. Edward, V. Verrina, P. C. M. Planken, and S. Witte, *High-resolution microscopy through optically opaque media using ultrafast photoacoustics,* Optics Express **28**, 33937 (2020).

[24] M. H. van Es, A. Mohtashami, R. M. T. Thijssen, D. Piras, P. L. M. J. van Neer, and H. Sadeghian, *Mapping buried nanostructures using subsurface ultrasonic resonance force microscopy,* Ultramicroscopy **184**, 209 (2018).

[25] S. Che, P. R. Guduru, A. V. Nurmikko, and H. J. Maris, *A scanning acoustic microscope based on picosecond ultrasonics,* Ultrasonics **56**, 153 (2015).

[26] B. C. Daly, N. C. R. Holme, T. Buma, C. Branciard, T. B. Norris, D. M. Tennant, J. A. Taylor, J. E. Bower, and S. Pau, *Imaging nanostructures with coherent phonon pulses,* Applied Physics Letters **84**, 5180 (2004).

[27] B. Audoin, M. Ducousso, T. Dehoux, C. Chollet, O. Zouani, C. Chanseau, and M.-C. Durrieu, *Picosecond acoustics at 30 GHz in the nucleus of an osteoblast cell,* in *Photons Plus Ultrasound: Imaging and Sensing 2011*, Vol. 7899 (SPIE, 2011) pp. 181–185.

[28] F. Pérez-Cota, R. J. Smith, E. Moradi, L. Marques, K. F. Webb, and M. Clark, *High resolution 3D imaging of living cells with sub-optical wavelength phonons,* Scientific Reports **6**, 39326 (2016).

[29] T. Dehoux, M. A. Ghanem, O. F. Zouani, J.-M. Rampnoux, Y. Guillet, S. Dilhaire, M.-C. Durrieu, and B. Audoin, *All-optical broadband ultrasonography of single cells,* Scientific Reports **5**, 8650 (2015).

[30] L. Liu, M. Simon, G. Muggiolu, F. Vilotte, M. Antoine, J. Caron, G. Kantor, P. Barberet, H. Seznec, and B. Audoin, *Changes in intra-nuclear mechanics in response to DNA damaging agents revealed by time-domain Brillouin micro-spectroscopy,* Photoacoustics **27**, 100385 (2022).

[31] B. Audoin, *Principles and advances in ultrafast photoacoustics; applications to imaging cell mechanics and to probing cell nanostructure,* Photoacoustics **31**, 100496 (2023).

[32] G. Tas and H. J. Maris, *Electron diffusion in metals studied by picosecond ultrasonics,* Physical Review B **49**, 15046 (1994).

[33] B. C. Daly, K. Kang, Y. Wang, and D. G. Cahill, *Picosecond ultrasonic measurements of attenuation of longitudinal acoustic phonons in silicon,* Physical Review B **80**, 174112 (2009).

[34] D. Li and D. G. Cahill, *Attenuation of 7 GHz surface acoustic waves on silicon,* Physical Review B **94**, 104306 (2016).

[35] H. Zhang, A. Antoncecchi, S. Edward, I. Setija, P. Planken, and S. Witte, *Unraveling Phononic, Optoacoustic, and Mechanical Properties of Metals with Light-Driven Hypersound,* Physical Review Applied **13**, 014010 (2020).

[36] O. Matsuda, M. C. Larciprete, R. Li Voti, and O. B. Wright, *Fundamentals of picosecond laser ultrasonics,* Ultrasonics **56**, 3 (2015).

[37] A. Devos, J.-F. Robillard, R. Côte, and P. Emery, *High-laser-wavelength sensitivity of the picosecond ultrasonic response in transparent thin films,* Physical Review B **74**, 064114 (2006).

[38] P. A. Mante, J. F. Robillard, and A. Devos, *Complete thin film mechanical characterization using picosecond ultrasonics and nanostructured transducers: Experimental demonstration on SiO2,* Applied Physics Letters **93**, 071909 (2008).

[39] F. Bruno, L. Saint-Martin, D. Thuau, and B. Audoin, *Multilayer transducer for highly efficient initiation of time-resolved Brillouin scattering,* Applied Physics Letters **120**, 212201 (2022).

[40] T. Bienville, J. F. Robillard, L. Belliard, I. Roch-Jeune, A. Devos, and B. Perrin, *Individual and collective vibrational modes of nanostructures studied by picosecond ultrasonics,* Ultrasonics Proceedings of Ultrasonics International (UI'05) and World Congress on Ultrasonics (WCU), **44**, e1289 (2006).

[41] A. Amziane, L. Belliard, F. Decremps, and B. Perrin, *Ultrafast acoustic resonance spectroscopy of gold nanostructures: Towards a generation of tunable transverse waves,* Physical Review B **83**, 014102 (2011).

[42] C. Jean, L. Belliard, T. W. Cornelius, O. Thomas, Y. Pennec, M. Cassinelli, M. E. Toimil-Molares, and B. Perrin, *Spatiotemporal Imaging of the Acoustic Field Emitted by a Single Copper Nanowire,* Nano Letters **16**, 6592 (2016).

[43] F. Xu, Y. Guillet, S. Ravaine, and B. Audoin, *All-optical in-depth detection of the acoustic wave emitted by a single gold nanorod,* Physical Review B **97**, 165412 (2018).

[44] R. Delalande, D. Garcia-Sanchez, and L. Belliard, *Towards acoustic microscopy at the nanoscale by coupling atomic force microscopy with picosecond ultrasonics,* Physical Review B **107**, 085409 (2023).

[45] G. de Haan, V. Verrina, A. J. L. Adam, H. Zhang, and P. C. M. Planken, *Plasmonic enhancement of photoacoustic-induced reflection changes,* Applied Optics **60**, 7304 (2021).

[46] G. de Haan, E. Abram, T. J. van den Hooven, and P. C. M. Planken, *Plasmonic enhancement of photoacoustic strain-waves on gold gratings,* AIP Advances **12**, 025227 (2022).

[47] T. J. van den Hooven and P. C. M. Planken, *Surface-plasmon-enhanced strain-wave-induced optical diffraction changes from a segmented grating,* Photoacoustics **31**, 100497 (2023).

[48] Y. Li, Q. Miao, A. V. Nurmikko, and H. J. Maris, *Picosecond ultrasonic measurements using an optical cavity,* Journal of Applied Physics **105**, 083516 (2009).

[49] P. Babilotte, P. Ruello, D. Mounier, T. Pezeril, G. Vaudel, M. Edely, J.-M. Breteau, V. Gusev, and K. Blary, *Femtosecond laser generation and detection of high-frequency acoustic phonons in GaAs semiconductors,* Physical Review B **81**, 245207 (2010).

[50] L. Liu, Y. Guillet, and B. Audoin, *Common-path conoscopic interferometry for enhanced picosecond ultrasound detection,* Journal of Applied Physics **123**, 173103 (2018).

[51] M. Robin, R. Guis, M. U. Arabul, Z. Zhou, N. Pandey, and G. J. Verbiest, *Experimental and numerical study of Conoscopic Interferometry sensitivity for optimal acoustic pulse detection in ultrafast acoustics,* Photoacoustics **30**, 100470 (2023).

[52] C. Quate, A. Atalar, and H. Wickramasinghe, *Acoustic microscopy with mechanical scanning—A review,* Proceedings of the IEEE **67**, 1092 (1979).

[53] H. Yu, *Scanning acoustic microscopy for material evaluation,* Applied Microscopy **50**, 25 (2020).

[54] S. Brand, A. Lapadatu, T. Djuric, P. Czurratis, J. Schischka, and M. Petzold, *Scanning acoustic gigahertz microscopy for metrology applications in three-dimensional integration technologies,* Journal of Micro/Nanolithography, MEMS, and MOEMS **13**, 011207 (2014).

[55] E. T. A. Mohamed and N. F. Declercq, *Giga-Hertz ultrasonic microscopy: Getting over the obscurity- A short review on the biomedical applications,* Physics in Medicine **9**, 100025 (2020).

[56] S. Salahuddin, K. Ni, and S. Datta, *The era of hyper-scaling in electronics,* Nature Electronics **1**, 442 (2018).

[57] P. van den Hurk, *Aligning lithography to the nanometer,* https://www.asml.com/en/news/stories/2021/fellow-simon-mathijssen-aligning-lithography-nanometer (2021).

[58] A. J. den Boef, *Optical wafer metrology sensors for process-robust CD and overlay control in semiconductor device manufacturing,* Surface Topography: Metrology and Properties **4**, 023001 (2016).

[59] L. Heineck, *First to market, second to none: The world's first 232-layer NAND,* https://www.micron.com/about/blog/memory/nand/first-to-market-second-to-none-the-worlds-first-232-layer-nand (2022).

[60] S. Rachidi and M. Rosmeulen, *Unlocking z-pitch scaling for next-generation 3d nand flash,* https://www.imec-int.com/en/articles/unlocking-z-pitch-scaling-next-generation-3d-nand-flash (2025).

[61] Y. Nishi, *Advances in Non-volatile Memory and Storage Technology* (Elsevier, 2014).

[62] P. Ruello and V. E. Gusev, *Physical mechanisms of coherent acoustic phonons generation by ultrafast laser action,* Ultrasonics **56**, 21 (2015).

[63] V. E. Gusev, *On the duration of acoustic pulses excited by subpicosecond laser action on metals,* Optics Communications **94**, 76 (1992).

[64] N. W. Ashcroft and N. D. Mermin, *Solid State Physics* (Holt, Rinehart and Winston, 1976).

[65] M. I. Kaganov, I. M. Lifshitz, and L. V. Tantarov, *Relaxation between electrons and the crystalline lattice,* Soviet Physics – JETP **4**, 173 (1957).

[66] C. Kittel, *Introduction to Solid State Physics* (John Wiley \& Sons, 2018).

[67] S. I. Anisimov, B. L. Kapeliovich, and T. L. Perel'Man, *Electron emission from metal surfaces exposed to ultrashort laser pulses,* Soviet Journal of Experimental and Theoretical Physics **39**, 375 (1974).

[68] T. Q. Qiu and C. L. Tien, *Heat Transfer Mechanisms During Short-Pulse Laser Heating of Metals,* Journal of Heat Transfer **115**, 835 (1993).

[69] T. Q. Qiu and C. L. Tien, *Femtosecond laser heating of multi-layer metals—I. Analysis,* International Journal of Heat and Mass Transfer **37**, 2789 (1994).

[70] Z. Lin, L. V. Zhigilei, and V. Celli, *Electron-phonon coupling and electron heat capacity of metals under conditions of strong electron-phonon nonequilibrium,* Physical Review B **77**, 075133 (2008).

[71] T. Q. Qiu and C. L. Tien, *Short-pulse laser heating on metals,* International Journal of Heat and Mass Transfer **35**, 719 (1992).

[72] P. B. Allen, *Theory of thermal relaxation of electrons in metals,* Physical Review Letters **59**, 1460 (1987).

[73] B. Rethfeld, A. Kaiser, M. Vicanek, and G. Simon, *Ultrafast dynamics of nonequilibrium electrons in metals under femtosecond laser irradiation,* Physical Review B **65**, 214303 (2002).

[74] L. D. Landau, E. M. Lifshitz, A. M. Kosevich, and L. P. Pitaevskii, *Theory of Elasticity: Volume 7* (Elsevier, 1986).

[75] A. Devos, M. Foret, S. Ayrinhac, P. Emery, and B. Rufflé, *Hypersound damping in vitreous silica measured by picosecond acoustics,* Physical Review B **77**, 100201 (2008).

[76] L. Anand and S. Govindjee, *Continuum Mechanics of Solids* (Oxford University Press, 2020).

[77] J. W. Tucker and V. W. Rampton, *Microwave Ultrasonics in Solid State Physics* (North Holland, 1972).

[78] W. P. Mason, *Physical Acoustics: Principles and Methods / Vol.3, Part B, Lattice Dynamics.* (Academic Press, New York ;, 1965).

[79] D. H. Hurley and O. B. Wright, *Detection of ultrafast phenomena by use of a modified Sagnac interferometer,* Optics Letters **24**, 1305 (1999).

[80] T. Tachizaki, T. Muroya, O. Matsuda, Y. Sugawara, D. H. Hurley, and O. B. Wright, *Scanning ultrafast Sagnac interferometry for imaging two-dimensional surface wave propagation,* Review of Scientific Instruments **77**, 043713 (2006).

[81] T. F. Crimmins, A. A. Maznev, and K. A. Nelson, *Transient grating measurements of picosecond acoustic pulses in metal films,* Applied Physics Letters **74**, 1344 (1999).

[82] R. M. Slayton and K. A. Nelson, *Picosecond acoustic transmission measurements. I. Transient grating generation and detection of acoustic responses in thin metal films,* The Journal of Chemical Physics **120**, 3908 (2004).

[83] S. J. Byrnes, *Multilayer optical calculations,* (2020), arXiv:1603.02720 [physics] .

[84] T. Saito, O. Matsuda, and O. B. Wright, *Picosecond acoustic phonon pulse generation in nickel and chromium,* Physical Review B **67**, 205421 (2003).

[85] K. H. Bennemann and K. H. Bennemann, *Non-Linear Optics in Metals*, International Series of Monographs on Physics (Oxford University Press, Oxford, New York, 1998).

[86] K. Yee, *Numerical solution of initial boundary value problems involving maxwell's equations in isotropic media,* IEEE Transactions on Antennas and Propagation **14**, 302 (1966).

[87] D. M. Sullivan, *Electromagnetic Simulation Using the FDTD Method* (Wiley-IEEE Press, 2000).

[88] P. Moczo, J. Kristek, V. Vavryčuk, R. J. Archuleta, and L. Halada, *3D Heterogeneous Staggered-Grid Finite-Difference Modeling of Seismic Motion with Volume Harmonic and Arithmetic Averaging of Elastic Moduli and Densities,* Bulletin of the Seismological Society of America **92**, 3042 (2002).

[89] C. Zeng, J. Xia, R. D. Miller, and G. P. Tsoflias, *An improved vacuum formulation for 2D finite-difference modeling of Rayleigh waves including surface topography and internal discontinuities,* GEOPHYSICS **77**, T1 (2012).

[90] L. N. Trefethen, *Group Velocity in Finite Difference Schemes,* SIAM Review **24**, 113 (1982).

[91] E. Isaacson and H. Keller, *Analysis of Numerical Methods* (Dover Publications Inc., 1994).

[92] J. K. Chen, J. E. Beraun, and C. L. Tham, *Comparison of one-dimensional and two-dimensional axisymmetric approaches to the thermomechanical response caused by ultrashort laser heating,* Journal of Optics A: Pure and Applied Optics **4**, 650 (2002).

[93] M. C. Velsink, M. Illienko, P. Sudera, and S. Witte, *Optimizing pump–probe reflectivity measurements of ultrafast photoacoustics with modulated asynchronous optical sampling,* Review of Scientific Instruments **94**, 103002 (2023).

[94] A. Abbas, Y. Guillet, J.-M. Rampnoux, P. Rigail, E. Mottay, B. Audoin, and S. Dilhaire, *Picosecond time resolved opto-acoustic imaging with 48 MHz frequency resolution,* Optics Express **22**, 7831 (2014).

[95] M. Lejman, V. Shalagatskyi, O. Kovalenko, T. Pezeril, V. V. Temnov, and P. Ruello, *Ultrafast optical detection of coherent acoustic phonons emission driven by superdiffusive hot electrons,* JOSA B **31**, 282 (2014).

[96] P. A. Elzinga, F. E. Lytle, Y. Jian, G. B. King, and N. M. Laurendeau, *Pump/Probe Spectroscopy by Asynchronous Optical Sampling,* Applied Spectroscopy **41**, 2 (1987).

[97] A. Bartels, A. Thoma, C. Janke, T. Dekorsy, A. Dreyhaupt, S. Winnerl, and M. Helm, *High-resolution THz spectrometer with kHz scan rates,* Optics Express **14**, 430 (2006).

[98] A. Bartels, R. Cerna, C. Kistner, A. Thoma, F. Hudert, C. Janke, and T. Dekorsy, *Ultrafast time-domain spectroscopy based on high-speed asynchronous optical sampling,* Review of Scientific Instruments **78**, 035107 (2007).

[99] R. Gebs, G. Klatt, C. Janke, T. Dekorsy, and A. Bartels, *High-speed asynchronous optical sampling with sub-50fs time resolution,* Optics Express **18**, 5974 (2010).

[100] G. Klatt, R. Gebs, C. Janke, T. Dekorsy, and A. Bartels, *Rapid-scanning terahertz precision spectrometer with more than 6 THz spectral coverage,* Optics Express **17**, 22847 (2009).

[101] G. Klatt, R. Gebs, H. Schäfer, M. Nagel, C. Janke, A. Bartels, and T. Dekorsy, *High-Resolution Terahertz Spectrometer,* IEEE Journal of Selected Topics in Quantum Electronics **17**, 159 (2011).

[102] O. Kliebisch, D. C. Heinecke, and T. Dekorsy, *Ultrafast time-domain spectroscopy system using 10 GHz asynchronous optical sampling with 100 kHz scan rate,* Optics Express **24**, 29930 (2016).

[103] C. Li, N. Krauß, G. Schäfer, L. Ebner, O. Kliebisch, J. Schmidt, S. Winnerl, M. Hettich, and T. Dekorsy, *High-speed asynchronous optical sampling based on GHz Yb:KYW oscillators,* Optics Express **25**, 9204 (2017).

[104] Y. Kim and D.-S. Yee, *High-speed terahertz time-domain spectroscopy based on electronically controlled optical sampling,* Optics Letters **35**, 3715 (2010).

[105] R. J. B. Dietz, N. Vieweg, T. Puppe, A. Zach, B. Globisch, T. Göbel, P. Leisching, and M. Schell, *All fiber-coupled THz-TDS system with kHz measurement rate based on electronically controlled optical sampling,* Optics Letters **39**, 6482 (2014).

[106] M. Yahyapour, A. Jahn, K. Dutzi, T. Puppe, P. Leisching, B. Schmauss, N. Vieweg, and A. Deninger, *Fastest Thickness Measurements with a Terahertz Time-Domain System Based on Electronically Controlled Optical Sampling,* Applied Sciences **9**, 1283 (2019).

[107] M. Illienko, M. C. Velsink, and S. Witte, *Understanding photoacoustic signal formation in the presence of transparent thin films,* Photoacoustics **38**, 100617 (2024).

[108] H. Zhang, A. Antoncecchi, S. Edward, P. Planken, and S. Witte, *Enhancing the detection of laser-excited strain waves via transparent nanolayers,* Physical Review B **104**, 205416 (2021).

[109] V. Gusev, *Laser hypersonics in fundamental and applied research,* Acustica Acta Acustica **82**, S37 (1996).

[110] Ch. Koch, *Coated fiber-optic hydrophone for ultrasonic measurement,* Ultrasonics **34**, 687 (1996).

[111] V. Wilkens and C. Koch, *Optical multilayer detection array for fast ultrasonic field mapping,* Optics Letters **24**, 1026 (1999).

[112] E. Zhang, J. Laufer, and P. Beard, *Backward-mode multiwavelength photoacoustic scanner using a planar Fabry-Perot polymer film ultrasound sensor for high-resolution three-dimensional imaging of biological tissues,* Applied Optics **47**, 561 (2008).

[113] D. E. Gray, *American Institute of Physics Handbook: 3d Ed* (McGraw-Hill, 1972).

[114] A. D. Rakić, *Algorithm for the determination of intrinsic optical constants of metal films: Application to aluminum,* Applied Optics **34**, 4755 (1995).

[115] P. B. Johnson and R. W. Christy, *Optical Constants of the Noble Metals,* Physical Review B **6**, 4370 (1972).

[116] J. F. Shackelford and W. Alexander, eds., *CRC Materials Science and Engineering Handbook*, 3rd ed. (CRC Press, Boca Raton, 2000).

[117] R. Boidin, T. Halenkovič, V. Nazabal, L. Beneš, and P. Němec, *Pulsed laser deposited alumina thin films,* Ceramics International **42**, 1177 (2016).

[118] P. Frank, *Fundamentals of Heat and Mass Transfer*, 6th ed. (John Wiley, Hoboken, NJ, 2007).

[119] M. Illienko, K. Chaudhary, M. C. Velsink, and S. Witte, *Characterization of Sub-Optical-Wavelength Structures through Optically Opaque Films Using Picosecond Ultrasonics,* Nano Letters **25**, 8909 (2025).

[120] N. G. Orji, M. Badaroglu, B. M. Barnes, C. Beitia, B. D. Bunday, U. Celano, R. J. Kline, M. Neisser, Y. Obeng, and A. E. Vladar, *Metrology for the next generation of semiconductor devices,* Nature Electronics **1**, 532 (2018).

[121] B. C. Daly, T. B. Norris, J. Chen, and J. B. Khurgin, *Picosecond acoustic phonon pulse propagation in silicon,* Physical Review B **70**, 214307 (2004).

[122] A. A. Maznev, F. Hofmann, A. Jandl, K. Esfarjani, M. T. Bulsara, E. A. Fitzgerald, G. Chen, and K. A. Nelson, *Lifetime of sub-THz coherent acoustic phonons in a GaAs-AlAs superlattice,* Applied Physics Letters **102**, 041901 (2013).

[123] J. A. Rogers, A. A. Maznev, M. J. Banet, and K. A. Nelson, *Optical Generation and Characterization of Acoustic Waves in Thin Films: Fundamentals and Applications,* Annual Review of Materials Research **30**, 117 (2000).

[124] O. Matsuda and O. B. Wright, *Reflection and transmission of light in multilayers perturbed by picosecond strain pulse propagation,* JOSA B **19**, 3028 (2002).

[125] D. R. Lide, *CRC Handbook of Chemistry and Physics*, Vol. 85 (CRC press, 2004).

[126] M. R. Querry, *Optical Constants of Minerals and Other Materials from the Millimeter to the Ultraviolet* (CRDEC-CR-88009, Aberdeen Proving Ground, Maryland, 1987).

[127] M. Born and E. Wolf, *Principles of Optics: Electromagnetic Theory of Propagation, Interference and Diffraction of Light*, 6th ed. (Pergamon, 1980).

[128] L. Belliard, T. W. Cornelius, B. Perrin, N. Kacemi, L. Becerra, O. Thomas, M. Eugenia Toimil-Molares, and M. Cassinelli, *Vibrational response of free standing single copper nanowire through transient reflectivity microscopy,* Journal of Applied Physics **114**, 193509 (2013).

[129] P.-A. Mante, L. Belliard, and B. Perrin, *Acoustic phonons in nanowires probed by ultrafast pump-probe spectroscopy,* Nanophotonics **7**, 1759 (2018).

SUMMARY

PICOSECOND ULTRASONICS FOR NANOSCALE SUBSURFACE STRUCTURAL CHARACTERIZATION

Picosecond ultrasonics (PU), also known as ultrafast photoacoustics, is a pump-probe experimental technique that utilizes laser-generated acoustic waves in the gigahertz to terahertz frequency range. In this method, an ultrashort laser pulse (pump) irradiates an opaque material, causing localized heating and rapid thermal expansion, which generates an acoustic wave. This wave propagates through the sample, reflects from internal interfaces, and returns to the surface, where it is detected by a time-delayed probe pulse. By systematically varying the temporal delay between the pump and probe pulses, one can investigate the generation, propagation, and reflection dynamics of the acoustic waves with sub-picosecond temporal resolution.

The picosecond timescale of acoustic generation enables several significant opportunities. Firstly, it generates ultrahigh-frequency acoustic modes, corresponding to acoustic wavelengths on the order of 100 nm. This short wavelength promises successful application of PU in high-resolution metrology. In particular, it has already been implemented as a tool for characterizing thin films and evaluating interfacial adhesion. Meanwhile, the detection and imaging of buried structures are in the active research and development phase. Secondly, PU provides an opportunity for exploring fundamental processes in solids governed by electron dynamics, such as electron transport and electron-phonon coupling, which is of high interest in fundamental physics studies.

In this thesis, we focus on exploiting PU for the detection and imaging of buried nanostructures. Despite the demonstrated potential for high-resolution imaging, several challenges remain. These include improving the signal-to-noise ratio in photoacoustic measurements, enabling the detection of complex (non-binary) and three-dimensional nanostructures, and overcoming the spatial resolution limits imposed by optical diffraction. Although light-induced acoustic waves can possess much shorter wavelengths than light itself, current implementations of PU remain constrained by optical probing methods. In this work, we address these challenges and propose approaches to advance the capabilities of PU for nanoscale detection and imaging.

In Chapter 1, we give an overview of the theory of light-induced elastic waves and their detection. We also present a numerical simulation model that we use in our studies to gain insights into physical processes occurring in photoacoustic experiments.

To perform experimental studies, we developed an asynchronous optical sampling (ASOPS) based pump-probe setup, as presented in Chapter 2. In our setup, we modified the ASOPS scheme by introducing a modulation of the frequency offset between the repetition rates of the pump and probe lasers. This modification results in higher measurement efficiency compared to traditional ASOPS and mechanical delay scan methods.

In Chapter 3, we address the problem of weak measured signals in photoacoustic experiments. Previous studies have demonstrated that thin transparent layers placed on top of the sample can enhance the detection efficiency of light-induced acoustic waves. This enhancement occurs because these layers eliminate the free-boundary constraint at the surface of opaque materials. However, the presence of these transparent layers significantly affects both the generation and detection of elastic waves, leading to a complex temporal photoacoustic response. In this chapter, our goal is to develop a detailed understanding of how signals are formed in such samples. We demonstrate that, in addition to the purely mechanical enhancement resulting from the elimination of the free-boundary constraint, the transparent layer introduces extra optical effects. These additional effects originate from the coating effect of the transparent layer and elastic wave coupling into this layer. For materials with weak strain-optic coupling, these additional optical contributions can play a dominant role in shaping the overall photoacoustic response.

In Chapter 4, we study the possibility of overcoming optical resolution limits on imaging of buried structures. The optical detection of acoustic waves partially levels out the advantage of the extremely short wavelength of acoustic waves generated by sub-picosecond laser pulses. Although the longitudinal resolution of the PU-based measurement technique can reach the nanometer level, the lateral resolution is still limited by the size of the focus spot of the probe pulse. However, we demonstrate that nanoscale spatial information is also encoded in the temporal variations of measured reflectivity through the diffraction and scattering of acoustic waves on internal structures. In this chapter, we use PU to characterize the main features of subsurface grating with linewidth down to 100 nm. We manage to retrieve not only grating parameters such as pitch and duty cycle, but also estimate the shape of the grating lines.

Lastly, in Chapter 5, we examine the photoacoustic response of directly exposed periodic structures. Upon pump excitation, these structures exhibit vibrational modes whose frequency spectra are governed by their geometrical parameters. A distinct correlation is observed between the frequency components and the grating period. However, further investigation is required to enable the precise quantitative retrieval of grating properties.

ULTRASNEL ULTRAGELUID VOOR HET KARAKTERISEREN VAN ONDOORZICHTIGE STRUCTUREN OP NANOSCHAAL

Picoseconde-ultrasoontechnologie (PU), ook bekend als ultrasnelle fotoakoestiek, is een pump-probe-experimentele techniek die gebruikmaakt van lasergegenereerde akoestische golven in het frequentiebereik van gigahertz tot terahertz. Bij deze methode bestraalt een ultrakorte laserpuls (pump) een ondoorzichtig materiaal, waardoor lokale verhitting en snelle thermische uitzetting optreden, wat een akoestische golf genereert. Deze golf verspreidt zich door het materiaal, wordt gereflecteerd door interne grensvlakken en keert terug naar het oppervlak, waar hij wordt gedetecteerd door een in de tijd vertraagde probe-puls. Door de tijdsvertraging tussen de pump- en probe-pulsen systematisch te variëren, kan men de dynamica van de generatie, de verspreiding en de reflectie van de akoestische golven onderzoeken met een tijdsresolutie van minder dan een picoseconde.

De picoseconde-tijdschaal van deze vorm van akoestische generatie biedt verschillende belangrijke mogelijkheden. Ten eerste genereert het ultrahoge frequentie akoestische modi, die overeenkomen met akoestische golflengten in de orde van 100 nm. Deze korte golflengte belooft een succesvolle toepassing van PU in metrologie met hoge resolutie. Het is met name al geïmplementeerd als een hulpmiddel voor het karakteriseren van dunne films en het evalueren van interfaciale hechting. Ondertussen bevinden de detectie en beeldvorming van verborgen structuren zich in de actieve onderzoeks- en ontwikkelingsfase. Ten tweede biedt PU de mogelijkheid om fundamentele processen in vaste stoffen te onderzoeken die worden beheerst door elektronendynamica, zoals elektronentransport en elektron-fononkoppeling, wat van groot belang is voor fundamentele natuurkundige studies. In dit proefschrift richten we ons op het gebruik van PU voor de detectie en beeldvorming van verborgen nanostructuren. Ondanks het aangetoonde potentieel voor beeldvorming met hoge resolutie, blijven er nog verschillende uitdagingen bestaan. Deze omvatten het verbeteren van de signaal-ruisverhouding in foto-akoestische metingen, het mogelijk maken van de detectie van complexe (niet-binaire) en driedimensionale nanostructuren, en het overwinnen van de ruimtelijke resolutielimieten die worden opgelegd door optische diffractie. Hoewel door licht geïnduceerde akoestische golven veel kortere golflengten kunnen hebben dan licht zelf, blijven de huidige implementaties van PU beperkt door optische meetmethoden. In dit werk gaan we deze uitdagingen aan en stellen we benaderingen voor om de mogelijkheden van PU voor detectie en beeldvorming op nanoschaal te verbeteren.

In Hoofdstuk 1 geven we een overzicht van de theorie van door licht geïnduceerde elastische golven en de detectie daarvan. We presenteren ook een numeriek simulatiemodel dat we in onze studies gebruiken om inzicht te krijgen in fysische processen die zich voordoen in foto-akoestische experimenten.

Om experimentele studies uit te voeren, hebben we een op asynchrone optische

sampling (ASOPS) gebaseerde pump-probe-opstelling ontwikkeld, zoals gepresenteerd in Hoofdstuk 2. In onze opstelling hebben we het ASOPS-schema aangepast door een modulatie van de frequentie-offset tussen de herhalingsfrequenties van de pump- en probe-lasers in te voeren. Deze aanpassing resulteert in een hogere meetefficiëntie in vergelijking met traditionele ASOPS- en mechanische vertragingsscanmethoden.

In Hoofdstuk 3 behandelen we het probleem van zwakke gemeten signalen in foto-akoestische experimenten. Eerdere studies hebben aangetoond dat dunne transparante lagen bovenop het materiaal de detectie-efficiëntie van door licht geïnduceerde akoestische golven kunnen verbeteren. Deze verbetering vindt plaats omdat deze lagen de vrije uitzetting van aan het oppervlak van ondoorzichtige materialen beperken. De aanwezigheid van deze transparante lagen heeft echter een aanzienlijke invloed op zowel het genereren als het detecteren van elastische golven, wat leidt tot een complexe temporele foto-akoestische respons. In dit hoofdstuk willen we een gedetailleerd inzicht krijgen in hoe signalen in dergelijke lagen worden gevormd. We tonen aan dat, naast de puur mechanische verbetering als gevolg van het wegvallen van de vrije uitzetting, de transparante laag extra optische effecten introduceert. Deze extra effecten zijn het gevolg van het coatingeffect van de transparante laag en de koppeling van elastische golven aan deze laag. Voor materialen waarvoor het effect van de elastische uitwijking op het probe-licht zwak is kunnen deze extra optische bijdragen een dominante rol spelen bij het vormgeven van de totale foto-akoestische respons.

In Hoofdstuk 4 bestuderen we de mogelijkheid om de optische resolutielimieten bij het in beeld brengen van structuren onder het oppervlak te overwinnen. De optische detectie van akoestische golven doet het voordeel van de extreem korte golflengte van akoestische golven die worden gegenereerd door sub-picoseconde laserpulsen gedeeltelijk teniet. Hoewel de longitudinale resolutie van de op PU gebaseerde meettechniek het nanometerniveau kan bereiken, wordt de laterale resolutie nog steeds beperkt door de grootte van het brandpunt van het probe-licht. We tonen echter aan dat nanoscopische ruimtelijke informatie ook gecodeerd is in de temporele variaties van de gemeten reflectiviteit door de diffractie en verstrooiing van akoestische golven op interne structuren. In dit hoofdstuk gebruiken we PU om de belangrijkste kenmerken van ondergrondse tralies met een lijnbreedte tot 100 nm te karakteriseren. We slagen erin om niet alleen tralie-eigenschappen zoals pitch en duty cycle te achterhalen, maar ook de vorm van de lijnen van het tralie te schatten.

Ten slotte onderzoeken we in Hoofdstuk 5 de foto-akoestische respons van direct blootgestelde periodieke structuren. Bij pump-excitatie vertonen deze structuren trillingsmodi waarvan de frequentiespectra worden bepaald door hun geometrische parameters. Er wordt een duidelijke correlatie waargenomen tussen de frequentiecomponenten en de periode van het tralie. Er is echter verder onderzoek nodig om de tralie-eigenschappen nauwkeurig kwantitatief te kunnen achterhalen.

Пікосекундна ультразвукова спектроскопія для визначення характеристик нанорозмірних підповерхневих структур

Пікосекундна ультразвукова спектроскопія (PU) - це експериментальна методика на основі «накачка-зонд» спектроскопії з розділенням у часі (time-resolved pump-probe spectroscopy). У цій методиці надкороткий субпікосекундний лазерний імпульс (накачка) опромінює непрозорий матеріал, спричиняючи локальне нагрівання. В результаті теплового розширення, що відбувається протягом декількох пікосекунд, генерується акустична хвиля з частотою в ГГц-ТГц діапазоні. Ця хвиля поширюється крізь експериментальний зразок, відбивається від внутрішніх струкур і повертається до поверхні зразка, де реєструється затриманим у часі зондуючим субпікосекундним лазерним імпульсом. Змінюючи часову затримку між імпульсами накачки та зонду, можна досліджувати процеси генерації, поширення та відбиття акустичних хвиль. При цьому надкоротка тривалість зондуючих лазерних імпульсів дозволяє досягати субпікосекундну роздільну здатність.

Пікосекундний часовий масштаб генерації акустичних хвиль відкриває низку важливих можливостей. По-перше, він забезпечує збудження високочастотних акустичних мод, що відповідають довжинам хвиль порядку 100 нм. Така коротка довжина хвилі робить можливим застосування PU у метрології високої роздільної здатності. Зокрема, метод вже використовується для визначення характеристик тонких плівок і оцінювання їх адгезії. Одночасно ведуться активні дослідження в напрямку детектування та візуалізації структур, покритих непрозорими матеріалами. По-друге, PU надає можливість досліджувати фундаментальні процеси в твердих тілах, спричинені електронною динамікою, наприклад, теплопровідність або електрон-фононну взаємодію.

У дисертації основна увага зосереджена на використанні PU для детектування та візуалізації наноструктур, покритих непрозорим матеріалом. Незважаючи на продемонстровану потенційну здатність PU до метрології високої роздільної здатності, певні труднощі залишаються актуальними. Серед них: підвищення відношення сигнал/шум у PU вимірюваннях; детектування складних (небінарних) і тривимірних наноструктур; а також подолання обмежень роздільної здатності, обумовлених дифракцією світла. Хоча світлоіндуковані акустичні хвилі можуть мати значно коротші довжини хвиль ніж саме світло, роздільна здатність сучасних реалізацій PU досі обмежена оптичними методами зондування. У роботі розглянуті зазначені проблеми та запропоновані підходи для розширення можливостей PU у детектуванні та візуалізації на наномасштабному рівні.

У розділі 1 подано огляд теорії світлоіндукованих акустичних хвиль і методів їх детектування. Також представлено модель для числових симуляцій, яку використано для аналізу фізичних процесів, що відбуваються у PU експериментах. Для проведення експериментальних досліджень розроблена «накачка-зонд» установка на основі методу асинхронної оптичної вибірки (asynchronous optical sampling ASOPS). У нашій системі схему ASOPS було модифіковано шляхом введення модуляції розстройки між частотами повторення імпульсів накачки та зонду. Ця модифікація підвищує ефективність вимірювань порівняно з традиційними методами ASOPS або використанням оптичних ліній затримки. Експериментальна установка описана в розділі 2.

У розділі 3 розглядається проблема слабкої амплітуди детектованих сигналів у PU експериментах. Попередні дослідження показали, що тонкі прозорі шари діелектрика, нанесені на поверхню зразка, можуть підвищувати ефективність детектування світлоіндукованих акустичних хвиль. Це зумовлено зміною граничних умов для акустичної хвилі на поверхні непрозорого матеріалу. Проте наявність прозорих шарів суттєво впливає як на генерацію, так і на детектування пружних хвиль, що призводить до значних змін форми експериментальних сигналів. Метою цього розділу є дослідження формування фотоакустичних сигналів у таких зразках. Показано, що, окрім підсилення сигналів, спричиненого зміною граничних умов, прозорий шар вносить додаткові оптичні ефекти. Ці ефекти зумовлені інтерференцією світла у прозорому шарі, а також фотопружними властивостями самого шару. Для матеріалів зі слабким пружньо-оптичним зв’язком ці оптичні внески можуть домінувати у формуванні фотоакустичних сигналів.

У розділі 4 розглянуто можливість подолання оптичних обмежень просторової роздільної здатності PU. Оптичний процес детектування частково нівелює переваги надзвичайно коротких довжин акустичних хвиль, що генеруються субпікосекундними лазерними імпульсами. Хоча поздовжня роздільна здатність методики PU може досягати нанометрів, поперечна роздільна здатність все ще обмежується розміром фокусної плями зондуючого лазерного променя. Ми показуємо, що інформація про наномасштабну геометрію внутрішніх структур також кодується у часових змінах виміряної відбивної здатності завдяки дифракції та розсіюванню акустичних хвиль. У цьому розділі PU використовується для визначення характеристик підповерхневих ґраток із характерними розмірами від 100 нм. Нам вдалося не лише визначити параметри ґраток, такі як період і скважність, але й оцінити поперечний профіль ліній ґраток.

У розділі 5 досліджено використання PU на відкритих ґратках. Після опромінення імпульсом накачки в таких ґратках збуджуються власні пружні коливання, частотні спектри яких визначаються геометричними параметрами ґраток. Виявлено чітку кореляцію між частотними компонентами та періодом ґраток. Проте, для точного кількісного визначення параметрів ґраток необхідні подальші дослідження.

LIST OF PUBLICATIONS

CHAPTER 2

M. C. Velsink, **M. Illienko**, P. Sudera, and S. Witte, *Optimizing pump-probe reflectivity measurements of ultrafast photoacoustics with modulated asynchronous optical sampling*, Review of Scientific Instruments **94**, 103002 (2023).

Author contributions: Conceptualization, Investigation, Methodology, Writing – review & editing.

CHAPTER 3

M. Illienko, M. C. Velsink, and S. Witte, *Understanding photoacoustic signal formation in the presence of transparent thin films*, Photoacoustics **38**, 100617 (2024).

Author contributions:, Conceptualization, Investigation, Methodology, Validation, Software, Data analysis, Data acquisition, Writing – original draft.

CHAPTER 4

M. Illienko, K. Chaudhary, M. C. Velsink, and S. Witte, *Characterization of sub-optical-wavelength structures through optically opaque films using picosecond ultrasonics*, Nano Letters **25**, 8909-8914 (2025).

Author contributions:, Conceptualization, Investigation, Methodology, Validation, Software, Data analysis, Data acquisition, Writing – original draft.

The author has also contributed to the following publications:

M. C. Velsink, M. Illienko, I. Setija, and S. Witte, *Nanometer-level metrology through opaque layers using laser-induced picosecond ultrasonics*, Light: Advanced Manufacturing, accepted.

M. C. Velsink, M. Illienko, K. Chaudhary, and S. Witte, *Improving signal-to-noise ratios in pump-probe spectroscopy on light-sensitive samples by adapting pulse repetition rates*, Optics Express **33**, 23632-23644 (2025).

K. Chaudhary, M. Illienko, T. van den Hooven, S. Witte, and P. Planken, *Optically enhancing and controlling photoacoustic signals using ultra-thin semiconductor coatings on metal surfaces*, Optics Express **33**, 199-214 (2025).

M. Illienko, Yu. Pilgun, and Ye. Smirnov, *Simultaneous acousto-optic diffractions by two lobes of a shaped phased-array transducer*, Ukrainian Journal of Physical Optics **22**, 138-150 (2021).

ACKNOWLEDGEMENTS

"It's over." Such a simple phrase, yet so evocative. It might bring relief and peace, but also sadness and melancholy, or even all these feelings at once. Now, as I close a significant chapter of my life, I find myself touched by all the shades of happiness for the work has been done, for the people I have met, and the challenges I have overcome. And at the same time, there is a bittersweet longing for an experience that cannot be repeated. Although among this swirl of feelings, one rises above the rest and will always stay with me. This is gratitude to everyone who supported me during my PhD journey and made my graduation possible.

I want to start with the EUV Generation & Imaging Group, where I completed my PhD. Like any research group, it was always changing. People were coming and leaving. But the welcoming and supportive atmosphere was something that never changed. I feel really lucky to have been part of this family.

Stefan, thank you for supervising me over these years. You gave me a lot of freedom to explore, while still staying closely involved and helping me to choose directions whenever I felt lost. You were always genuinely happy to see any scientific progress, even when it didn't turn out as nicely as we'd hoped. I really appreciated how open you were to both deep discussions and quick bits of advice. You also care a lot about the well-being of your PhD students, and that definitely doesn't go unnoticed. Thank you for putting so much effort into making my PhD experience as low-stress as it could be.

Kjeld, thank you for setting up the group with Stefan, for your valuable advice during group meetings, and for your consistently uplifting attitude. I appreciate the amazing ultrafast lasers course I took from you at the beginning of my PhD. It turned out to be incredibly useful for everything that followed.

Matthijs, buddy, we started our PhDs almost at the same time, and pretty quickly, it was just the two of us doing photoacoustics in the group. Neither of us really knew much about it back then, so we were figuring everything out as we went. It was kind of insane, man. So many days spent deep in discussions about theory and simulations, building setups from scratch, chasing wild ideas. And the best part is, some of them actually worked! You're an amazing scientist. You are curious, fearless, and always ready to bring even the craziest, most convoluted ideas to life. That's what makes research so fun and exciting. I'm really proud to have worked side by side with you all these years. And beyond the lab, we became close friends. I've always felt your support, both at work and in daily life. After all those conferences, you helping me to move several times, dinners, pub nights, and everything in between, I’m honestly just grateful the universe brought us both to ARCNL at the same time.

Ale, you’re basically my godfather in photoacoustics. We only overlapped for a couple of months, but you did so much to get me started in the lab. With COVID and all the access restrictions, it wasn’t that easy, but whenever we were there, you made the most of it. You were babysitting me while still working on your own thesis, which is pretty impressive. Thanks a lot for your patience, and for answering all my questions (even the not-so-smart ones). You gave me a solid foundation to start my own research journey, and I really appreciate that.

Hao, we only met in person once, just as you were leaving to China. Although we had numerous online meetings, during which I learned a lot of the theory of photoacoustics from you. Together with Ale, you laid the foundation that allowed me to get started.

Nik, you are the best technician ever! So enthusiastic and always eager to build something for us. I have to admit, there were times I felt a bit bad when you approached me with that spark in your eyes, asking, “What can I build for you?” and I had nothing to suggest. You were always genuinely invested in making our lab the best it could be, and that should never go unappreciated.

Zeudi, awesome Italian, I don’t know what to say more, haha. The first day I came to the office, I saw you, and the first thing you said was ”You look like my sister’s ex. Can I take a picture of you?”. In that moment, I realized I was in the right place:) You were an energy plant of our group. It was impossible to lose motivation while you were around. At the same time, you were extremely empathetic and understanding. I enjoyed so much our trainings for the Berlin skate marathon during our lunch breaks. It’s a shame we didn’t manage to do it together in the end.

Randy, I was always impressed by how engaged you were in every group meeting. You consistently had something to contribute, and it was always to the point. It paired perfectly with your Dutch straightforwardness. You never hesitated to call things out, even when it might have sounded harsh, whether in science or everyday situations. I really loved that. The blunt truth you shared always motivated me to do better.

Maisie, thank you for getting me into swing dancing. It truly helped me stay sane, haha. Well, I’m grateful for much more than that, though. You were an amazing colleague. Beyond our many enjoyable chats, both in and out of the office, and your sharing of your own PhD experiences, you consistently helped me stay on course toward my graduation and not get lost in circles.

Prerna, you were the first postdoc to join Matthijs and me on the project after we had been on our own for quite some time. We both really appreciated your easygoing nature and your willingness to contribute so much. You brought new

energy and joy to our small subgroup. The time you spent with us feels like a distinct and memorable chapter of my PhD journey.

Matthias, you're the most person people I've ever met. Every time I walked into the office, you'd light up with a smile and go straight for a hug. I love how you're always up for any crazy thing, whether it's a spontaneous 7 am trip to Belgium or floating through Amsterdam canals on an inflatable mattress. Buddy, I'm really happy to have you in my life. From swing dancing socials to camping in Greece and everything in between, it was amazing! I hope there's much more ahead.

Augustas, you definitely brought a fun kind of chaos into the group. If Matthias was doing something wild, there was about an 80 % chance it started with you :D Your group meeting presentations, which mix solid science with provocative (and sometimes dark) humor, are another work of art. I really admire how you try to keep things simple and don't overcomplicate just for the sake of fancy appearances. And beyond that, you're a great friend: empathetic, always ready to listen, and be there when it matters. Thanks for randomly coming across Stefan's thesis and deciding to reach out to him.

Aaron, you joined when I was almost done with my PhD, but maybe because you are so great, I slowed down my progress to overlap with you more, haha. I loved how quickly and easily you got absorbed into the group, as you have always been there. m happy to continue working with you, and as your new flatmate, I hope we'll have a lot of fun in the coming couple of years.

Komal, we started collaborating when you were in Paul's group, and then you joined ours in the final year of my PhD. We worked on the same project, which came with plenty of tricky puzzles. Thank you for all the endless brainstorming sessions, even when it looked like there was no way out.

Fengling, Antonios, Jan, Anne, Jacob, Kevin, and Edcel, thank you for all the priceless discussions during our group meetings, the joyful lunch breaks, the shared conference experiences, and all the fun we had outside of work. It really meant a lot to go through all of that together.

I would like to thank the members of the Light-Matter Interaction group, with whom we shared close scientific interests that led to fruitful collaborations. Paul, Klaasjan, Thomas, Ester, and Lorenzo, thank you for the valuable discussions, both during our joint group meetings and in those casual coffee break chats at the office.

Paul, thank you for being my second supervisor. It was really reassuring to have another group leader at ARCNL who's an expert in photoacoustics. You were always happy to share your thoughts and help to work through the challenges that came up. Furthermore, in my first year, I had the opportunity to use your lab, where I learned the fundamentals of experimental photoacoustics. Thank you a lot for making that possible.

ARCNL was an outstanding place to work, thanks to the dedicated people behind it. I'm greatful to those who made that happen. To the management team: Joost, as the first director, you laid the foundation and helped to shape the institute into the thriving scientific environment it is today; Wim, as the new director, you got up to speed quickly and stayed closely involved with every PhD student's progress, offering a gentle but firm push to help everyone successfully complete their PhD journey; and Marjan, as institute manager, you kept ARCNL running smoothly day to day. Thank you for your consistent efforts in keeping everything on track and for always being there to help with any administrative or bureaucratic challenge. To the members of the secretariat: Celine, Ellen, Jet, Jusra, and Marja. Thank you for making our institute a cozy and welcoming place.

Of course, to my ARCNL colleagues! Beyond the many scientific discussions during poster sessions and coffee breaks, I also enjoyed all the simple moments we shared: picnics, movie nights, bingo games, foosball, volleyball and soccer tournaments, and so much more. All of that made me feel like part of a big, wonderful family. Thank you, Lucas, Nataliia, John, Kevin, Ester PP, Yahia, Manos, Tanya, Dion, Barsha, Aleksandra, Jane, Zhonghui, Ksenia, Francesco, Roy, Kian, Paul, Leo, Reynolds, Karl, Luka, Christoph.

Irwan and Stephen, as our contacts at ASML, you kept a close eye on the progress of our research, offering valuable feedback along the way. You also brought in new ideas for future directions, several of which grew into successful projects.

Now I want to thank people who were with me and for me during these years. Daphne, you were my first friend in Amsterdam, and became the closest. Our friendship grew much like our trips together did. What started with simple biking through Dutch tulip fields turned into a full-on Iceland expedition packed with every possible adventure. At this point, I honestly can't imagine how my PhD journey would have looked without you. I'm so grateful for every moment we've shared. Maksym, you were the first Ukrainian I met in Amsterdam, and what a coincidence that we share the same name! Thank you for all the great times we've had together and for your genuine support throughout these years.

To my university friends! Viktor, Taras, Roman, and Anton, thank you for staying close despite the distance. Our regular reunion trips were always refreshing and left me recharged, and that time together is something I always look forward to. Kateryna, you and Taras always welcomed me in Leuven, no matter the occasion, making me feel right at home. Thank you for that!

To my childhood friends who have stuck with me all this time: Stanislav, Petro, Serhii, and Denys. We don't get to meet often, but even through the occasional call or text, I feel you there. Thank you, guys!

My scientific journey began during my bachelor's and master's studies at Taras Shevchenko National University of Kyiv. I would like to express my gratitude to the Acousto-Optics Lab team, especially my first supervisors, Yevhen Smirnov, Yuriy

Pilgun, and Serhii Kolienov, for giving me that push into the academic world.

Цілком можливо, я б не був там, де я зараз, без моїх неймовірних шкільних вчителів. Сергію Вікторовичу та Наталіє Володимирівно, я безмежно вдячний вам за ті захоплюючі уроки фізики та математики, які множили моє бажання поринути глибше в науку. Окремо вдячний Вам, Людмило Григорівно, за те, що дали мені найнеобхідніший інструмент, завдяки якому я відкрив світ.

Наостанок хочу подякувати своїм рідним. Насамперед своїм батькам. Мамо й Тату, дякую вам за все! Ви зростили мене з бажанням дати мені найкраще і я не можу це не відчувати. Ви навчили мене самостійно будувати своє щасливе життя незалежно від обствин. І, можливо, це й є найкраще, що може бути у людини. Тату, ти був моїм першим вчителем фізики. Ти брав мене, зовсім малого, до себе в школу, де ти колись працював, і показував мені різноманітні фізичні демонстрації. Абсолютно нічого не розуміючи, але неймовірно вражений, я дивився на штучні блискавки і в моїй голові з'являлося все більше питань “чому?” і “як?”. Хтозна, можливо в ті моменти в мені й почала зароджуватись цікавість про навколишній світ та про те як він влаштований. Мамо, ти завжди вірила в мій успіх і продовжуєш це робити. Крім того, своїм прикладом енергійності і завзятості своєю роботою ти не залишаєш мені вибору, окрім як робити так само. Дякую тобі за те, що ти така крута!:) Сева, брате, дякую, що не даєш батькам нудьгувати. Сподіваюсь, скоро зможемо бачитись частіше. Дякую, всім своїм рідним за підтримку та постійний міцний зв'язок незважаючи на велику відстань між нами.